

EUR 3323 e

EUROPEAN ATOMIC ENERGY COMMUNITY - EURATOM

PHYSICAL PROPERTIES OF UO_2
SINGLE CRYSTALS

by

R. GEVERS *et al.*
(CEN)

1967



EURATOM/US Agreement for Cooperation

EURAEC Report No. 1776 prepared by CEN
Centre d'Etude de l'Energie Nucléaire, Mol-Belgium

Euratom Contract No. 056-64-3 TEEB

LEGAL NOTICE

This document was prepared under the sponsorship of the Commission of the European Communities in pursuance of the joint programme laid down by the Agreement for Cooperation signed on 8 November 1958 between the Government of the United States of America and the European Communities.

It is specified that neither the Commission of the European Communities nor the Government of the United States, their contractors or any person acting on their behalf :

Make any warranty or representation, express or implied, with respect to the accuracy, completeness, or usefulness of the information contained in this document, or that the use of any information, apparatus, method, or process disclosed in this document may not infringe privately owned rights; or

Assume any liability with respect to the use of, or for damages resulting from the use of any information, apparatus, method or process disclosed in this document.

This report is on sale at the addresses listed on cover page 4

at the price of FF 15.—	FB 150.—	DM 12.—	Lit. 1 870	Fl. 11.—
-------------------------	----------	---------	------------	----------

When ordering, please quote the EUR number and the title, which are indicated on the cover of each report.

Printed by CEN, Mol
Brussels, October 1967

EUR 3323 e

PHYSICAL PROPERTIES OF UO_2 SINGLE CRYSTALS
by R. GEVERS *et al.* (CEN)

European Atomic Energy Community - EURATOM
Euratom/US Agreement for Cooperation
EURAEK Report No. 1773 prepared by CEN -
Centre d'Etude de l'Energie Nucléaire, Mol (Belgium)
Euratom Contract No. 056-64-3 TEEB
Brussels, October 1967 - 104 Pages - 58 Figures - FB 150

Further progress in the investigation of different fundamental physical properties of uranium dioxide is presented. The following studies were undertaken :

- the preparation of big single crystals using large sintered cylinders made by slip casting;
- the observation in the optical microscope of the structure of U_4O_9 precipitates in UO_{2+x} with various oxygen contents;

EUR 3323 e

PHYSICAL PROPERTIES OF UO_2 SINGLE CRYSTALS
by R. GEVERS *et al.* (CEN)

European Atomic Energy Community - EURATOM
Euratom/US Agreement for Cooperation
EURAEK Report No. 1776 prepared by CEN -
Centre d'Etude de l'Energie Nucléaire, Mol (Belgium)
Euratom Contract No. 056-64-3 TEEB
Brussels, October 1967 - 104 Pages - 58 Figures - FB 150

Further progress in the investigation of different fundamental physical properties of uranium dioxide is presented. The following studies were undertaken :

- the preparation of big single crystals using large sintered cylinders made by slip casting;
- the observation in the optical microscope of the structure of U_4O_9 precipitates in UO_{2+x} with various oxygen contents;

- the observation of anti-phase boundaries in thin foils of U_4O_9 by transmission electron microscopy;
- the measurement of the thermal conductivity of stoichiometric and slightly oxidized UO_2 in the temperature range between 4.2 and 300 °K;
- the study of the electrical conductivity, Hall effect and thermoelectric power as a function of composition and temperature : these results favour an electronic conduction mechanism in UO_{2+x} by small polarons;
- the study of some aspects of motion phenomena of uranium and oxygen ions in UO_2 ; this includes the determination of the diffusion coefficients for the uranium-235 ion in stoichiometric UO_2 , the activation energies for migration of uranium point defects and oxygen interstitials and the activation energy for reorientation of oxygen interstitials;
- the measurement of the magnetic susceptibility of UO_{2+x} crystals with $0 < x < 0.25$ at temperatures ranging from 90 to 300 °K and magnetic fields between 7 and 11 kOe.

-
- the observation of anti-phase boundaries in thin foils of U_4O_9 by transmission electron microscopy;
 - the measurement of the thermal conductivity of stoichiometric and slightly oxidized UO_2 in the temperature range between 4.2 and 300 °K;
 - the study of the electrical conductivity, Hall effect and thermoelectric power as a function of composition and temperature : these results favour an electronic conduction mechanism in UO_{2+x} by small polarons;
 - the study of some aspects of motion phenomena of uranium and oxygen ions in UO_2 ; this includes the determination of the diffusion coefficients for the uranium-235 ion in stoichiometric UO_2 , the activation energies for migration of uranium point defects and oxygen interstitials and the activation energy for reorientation of oxygen interstitials;
 - the measurement of the magnetic susceptibility of UO_{2+x} crystals with $0 < x < 0.25$ at temperatures ranging from 90 to 300 °K and magnetic fields between 7 and 11 kOe.

EUR 3323 e

EUROPEAN ATOMIC ENERGY COMMUNITY - EURATOM

PHYSICAL PROPERTIES OF UO_2
SINGLE CRYSTALS

by

R. GEVERS *et al.*
(CEN)

1967



EURATOM/US Agreement for Cooperation

EURAE C Report No. 1776 prepared by CEN
Centre d'Etude de l'Energie Nucléaire, Mol-Belgium

Euratom Contract No. 056-64-3 TEEB

SUMMARY

Further progress in the investigation of different fundamental physical properties of uranium dioxide is presented. The following studies were undertaken :

- the preparation of big single crystals using large sintered cylinders made by slip casting;
- the observation in the optical microscope of the structure of U_4O_9 precipitates in UO_{2+x} with various oxygen contents;
- the observation of anti-phase boundaries in thin foils of U_4O_9 by transmission electron microscopy;
- the measurement of the thermal conductivity of stoichiometric and slightly oxidized UO_2 in the temperature range between 4.2 and 300 °K;
- the study of the electrical conductivity, Hall effect and thermoelectric power as a function of composition and temperature : these results favour an electronic conduction mechanism in UO_{2+x} by small polarons;
- the study of some aspects of motion phenomena of uranium and oxygen ions in UO_2 ; this includes the determination of the diffusion coefficients for the uranium-235 ion in stoichiometric UO_2 , the activation energies for migration of uranium point defects and oxygen interstitials and the activation energy for reorientation of oxygen interstitials;
- the measurement of the magnetic susceptibility of UO_{2+x} crystals with $0 < x < 0.25$ at temperatures ranging from 90 to 300 °K and magnetic fields between 7 and 11 kOe.

Supervisor : R. Gevers (S.C.K.)

Research Associates : R. De Batist (S.C.K.)
R. De Coninck (S.C.K.)
M. Denayer (S.C.K.)
J. Devreese (S.C.K.)
P. Nagels (S.C.K.)
R. Penninckx (S.C.K.)
A. Van den Bosch (S.C.K.)
W. Van Lierde (S.C.K.)

Technical Assistance : M. Delcon (S.C.K.)
A. Gijs (S.C.K.)
L. Van Gool (S.C.K.)
M. Van Roy (S.C.K.)
A. Vranken (S.C.K.)
G. Wilms (S.C.K.)

TABLE OF CONTENTS

	Pages
LIST OF FIGURES	5
1. PREPARATION	9
2. STRUCTURAL INVESTIGATION BY OPTICAL MICROSCOPY	10
3. STRUCTURAL INVESTIGATION BY ELECTRON MICROSCOPY	12
4. SURFACE ENERGY OF STOICHIOMETRIC UO ₂	13
5. LOW TEMPERATURE THERMAL CONDUCTIVITY	14
5.1. Introduction	14
5.2. Method of measurement and applied techniques	14
5.3. Description of the apparatus	15
5.4. Other technological properties of the apparatus	16
5.5. Experimental results	17
6. ELECTRICAL PROPERTIES	18
6.1. Introduction	18
6.2. Resistivity and Hall effect measurements	20
6.2.1. Experimental procedures	20
6.2.2. Results and discussion	20
6.3. Thermoelectric power measurements	23
6.3.1. Introduction	23
6.3.2. The apparatus	24
6.3.3. Crystal treatments	25
6.3.4. Results and discussion	26
6.4. Some theoretical considerations about the conduction mechanism in UO ₂	30
7. ATOMIC MOTION PHENOMENA	34
7.1. Uranium self-diffusion in UO ₂	34
7.1.1. Introduction	34
7.1.2. Experimental procedures and results	34
7.1.3. Discussion	36
7.2. Migration energies for uranium and oxygen point defects	36
7.2.1. Introduction	36
7.2.2. Migration energy of oxygen interstitials	36
7.2.3. Migration energy of uranium	38
7.3. Reorientation of oxygen interstitials	41
8. KUCZYNSKI TYPE EXPERIMENTS	45
9. MAGNETIC SUSCEPTIBILITY	46
REFERENCES	50

LIST OF FIGURES

- Fig. 1 : Cooling rate of UO_2 single crystals after oxidation at $1400^\circ C$
- Fig. 2 : Polished and stain-etched surfaces of UO_2 single crystals as observed by reflection in the optical microscope
- a) U_4O_9 bright regions, $O/U = 2.013$ ($\times 150$)
 - b) U_4O_9 dark regions, $O/U = 2.041$ ($\times 150$)
 - c) U_4O_9 dark regions, $O/U = 2.08$ ($\times 150$)
 - d) U_4O_9 bright regions, $O/U = 2.11$ ($\times 150$)
 - e) U_4O_9 dark regions, $O/U = 2.12$ ($\times 150$)
 - f) U_4O_9 bright regions, $O/U = 2.17$ ($\times 150$)
 - g) U_4O_9 dark regions, $O/U = 2.19$ ($\times 150$)
 - h) U_4O_9 bright regions, $O/U = 2.23$ ($\times 150$)
 - i) U_4O_9 bright regions, $O/U = 2.05$ ($\times 400$)
 - j) U_4O_9 bright regions, precipitations in the $\{100\}$ plane, $O/U = 2.056$ ($\times 400$)
 - k) U_4O_9 bright regions, precipitations in the $\{110\}$ plane, $O/U = 2.056$ ($\times 400$)
 - l) U_4O_9 bright regions, precipitations in the $\{111\}$ plane, $O/U = 2.056$ ($\times 400$)
 - m) U_4O_9 bright regions, surface precipitations in the $\{100\}$ plane, $O/U = 2.056$ ($\times 400$)
 - n) U_4O_9 bright regions, surface precipitations in the $\{110\}$ plane, $O/U = 2.056$ ($\times 400$)
 - o) U_4O_9 bright regions, surface precipitations in the $\{111\}$ plane, $O/U = 2.056$ ($\times 400$)
- Fig. 3 : Polished and stain-etched surface of a $UO_{2.056}$ single crystal as observed in the optical microscope ($\times 400$)
- Fig. 4 : Surface of the same $UO_{2.056}$ single crystal after irradiation up to a dose $nvt = 1.7 \times 10^{19}$ thermal neutrons, cm^{-2} ($\times 400$)
- Fig. 5 : Polished and stain-etched surface of a $UO_{2.056}$ single crystal as observed in the optical microscope ($\times 400$)- After irradiation to a dose of 10^{20} thermal neutrons, cm^{-2} no precipitates of U_4O_9 could be detected by optical microscopy
- Fig. 6 : Anti-phase boundaries in U_4O_9 crystals
- Fig. 7 : Magnified part of Fig. 6 to show the detail of the fringes at two triple points
- Fig. 8 : Schematic representation of Fig. 7
- Fig. 9 : Theoretical pore having the form of a regular polyhedron and consisting of eight $\{111\}$ planes and six $\{100\}$ planes

- Fig. 10** : Shape of pores as observed after annealing at 1600–1700°C
 a) Pore cut by a {100} plane ($\times 1500$)
 b) Pore cut by a {111} plane ($\times 1500$)
- Fig. 11** : Arrangement used for the measurement of the thermal conductivity at low temperatures
- Fig. 12** : Schematic drawing of the cryostat used for the thermal conductivity measurements
- Fig. 13** : Thermal conductivity of UO_2 single crystals as a function of temperature (curves 1, 2 and 3) – The dashed line (curve 4) corresponds to measurements made by Bethoux et al. on a sintered UO_2 polycrystal
- Fig. 14** : Phonon mean free path in UO_2 as a function of temperature (curve 1 : nearly stoichiometric UO_2 ; curve 2 : slightly oxidized UO_2)
- Fig. 15** : Electrical conductivity of UO_2 single crystals with O/U ratios smaller than 2.001
- Fig. 16** : Complete set of conductivity data of UO_2 single crystals with compositions $0 < x < 0.18$
- Fig. 17** : Conductivity and Hall coefficient of a UO_2 single crystal with $O/U \simeq 2.001$ – Notice the reversal of sign of the Hall coefficient
- Fig. 18** : Hall mobility of a reduced UO_2 single crystal ($O/U < 2.001$) as a function of the reciprocal temperature
- Fig. 19** : Conductivity and Hall coefficient as a function of the reciprocal temperature of a UO_2 single crystal with $O/U \simeq 2.05$
- Fig. 20** : Conductivity and Hall coefficient as a function of the reciprocal temperature of a UO_2 single crystal with $O/U \simeq 2.10$
- Fig. 21** : Conductivity and Hall coefficient as a function of the reciprocal temperature of a UO_2 single crystal with $O/U \simeq 2.14$
- Fig. 22** : Conductivity and Hall coefficient as a function of the reciprocal temperature of a UO_2 single crystal with $O/U \simeq 2.15$
- Fig. 23** : Hall mobilities as a function of the reciprocal temperature of UO_2 crystals with O/U ratios varying between 2.05 and 2.15
- Fig. 24** : Schematic drawing of the cryostat used for measurements of thermoelectric power and electrical conductivity
- Fig. 25** : Sample holder for measurement of thermoelectric power and electrical conductivity
- Fig. 26** : Switch system used for measurement of thermoelectric power and electrical conductivity
- Fig. 27** : General view of the apparatus for measurements of thermoelectric power and electrical conductivity

- Fig. 28 : Thermoelectric power as a function of the reciprocal temperature for oxidized UO_2 single crystals ($2.046 < O/U < 2.25$)
- Fig. 29 : Thermoelectric power as a function of reciprocal temperature for slightly oxidized UO_2 single crystals ($0.001 < x < 0.013$)
- Fig. 30 : Electrical conductivity of two as-grown crystals ($O/U \simeq 2.005$) versus reciprocal temperature
- Fig. 31 : Thermoelectric power as a function of reciprocal temperature for UO_2 crystals before and after reduction
- Fig. 32 : Thermoelectric power of nearly stoichiometric UO_2 single crystals ($0.001 < x$) versus reciprocal temperature
- Fig. 33 : Thermoelectric power measurements on UO_2 as reported by different authors : Bates (curve A), Wolfe (curves F and G), Aronson et al. (curve D), Karkhanavala et al. (curve E), present work (curves H, B, K and I)
- Fig. 34 : Electrical conductivity measurements on UO_2 as reported by different authors : Bates (curves A and B), Wolfe (curves C and D), Karkhanavala et al. (curve E), present work (curves O, S, F, U, α and G)
- Fig. 35 : Electrical conductivity of different specimens in a diagram $\log \sigma T^{3/2}$ versus reciprocal temperature - Curves SR-2 and CC-14 correspond to measurements made by Wolfe
- Fig. 36 : Electrical conductivity of different specimens (other than Fig. 35) in a diagram $\log \sigma T^{3/2}$ versus reciprocal temperature - Curves SR-2 and CC-14 correspond to measurements made by Wolfe
- Fig. 37 : Thermoelectric power and conductivity of a nearly stoichiometric UO_2 crystal (sample N) before and after quenching
- Fig. 38 : Thermoelectric power and conductivity of a nearly stoichiometric UO_2 crystal (sample T) before and after quenching
- Fig. 39 : Thermoelectric power and conductivity of a nearly stoichiometric UO_2 crystal (sample U) before and after quenching
- Fig. 40 : Thermoelectric power as a function of reciprocal temperature for a nearly stoichiometric UO_2 crystal before and after irradiation
- Fig. 41 : Idem as Fig. 40
- Fig. 42 : Idem as Fig. 40
- Fig. 43 : Idem as Fig. 40
- Fig. 44 : Idem as Fig. 40
- Fig. 45 : Uranium self-diffusion data for UO_2 according to different authors - Curve 1 : Auskern et al. and present work ; curve 2 : Lindner et al.; curve 3 : McNamara

- Fig. 46 : Isochronal annealing of a quenched UO_{2+x} single crystal ($O/U \simeq 2.005$)
- Fig. 47 : Conductivity measurements during linear heating and cooling of a quenched UO_{2+x} single crystal
- Fig. 48 : Two successive isothermal annealing curves measured on a quenched UO_{2+x} crystal ($O/U \simeq 2.005$) at the temperatures $133.3^\circ C$ and $161.1^\circ C$
- Fig. 49 : Recovery of the electrical conductivity due to annealing of UO_2 previously irradiated with thermal neutrons ; the conductivity values before irradiation are 1.4×10^{-3} (curve 1) and $1.2 \times 10^{-3} \text{ ohm}^{-1}\text{cm}^{-1}$ respectively
- Fig. 50 : Analysis following the method of Balarin and Zetzsche of the pulse annealing data of UO_2 previously irradiated with thermal neutrons - The dotted and full lines correspond to first and second order kinetics respectively
- Fig. 51 : Model for an oxygen interstitial in UO_{2+x} (according to Willis)
- Fig. 52 : Neck growth as a function of the square root of time during sintering
- Fig. 53 : Neck between two spheres sintered at $1700^\circ C$ for 3 h ($\times 1500$)
- Fig. 54 : Neck between two spheres sintered at $1700^\circ C$ for 7 h ($\times 1500$)
- Fig. 55 : Reciprocal of the magnetic susceptibility as a function of the absolute temperature
- Fig. 56 : Reciprocal of the magnetic susceptibility of a UO_2 crystal (F) as a function of the absolute temperature
- Fig. 57 : Weiss constant θ of different UO_2 crystals as a function of the O/U ratio
- Fig. 58 : Curie constant C of different UO_2 crystals as a function of the O/U ratio

1. PREPARATION

All the single crystals used in the different studies have been prepared by the sublimation method using UO_2 with natural uranium isotope content. The growth process has been described in detail in the final reports of the first and second year of study. Therefore, only a few modifications which were introduced, especially to grow larger crystals, will be reported.

The single crystals are prepared by vaporization of UO_2 from the interior of a cylinder of sintered UO_2 , followed by condensation of the UO_2 vapour on a cooled tungsten sheet. The UO_2 itself is used as a container and as a heating element. During the first two years of study pressed cylinders of UO_2 (5 cm long and 2 cm thick) were used. As the size of the crystals depends mainly on the size of the cylinder, larger cylinders (42 mm diameter, 17 mm bore and 53 mm length, weighing 440 g) have been made by a modified slip-casting technique. To prepare the UO_2 slip, agate jars cannot be used because of unavoidable introduction of impurities during milling (up to 300 ppm SiO_2). The slip was then prepared by vibration, the stirrer being made of uranium metal. In this way one avoids the introduction of impurities. Very large high quality single crystals have been grown in this way. About 100 g of crystals of suitable size are obtained in one operation.

The O/U ratio of the as-grown crystals varies in most cases between 2.002 and 2.007, if starting from UO_2 cylinders obtained by sintering in pure hydrogen.

The composition of these crystals can afterwards be varied either by reduction in pure hydrogen at around 1400°C (in this case nearly stoichiometric crystals are obtained) or by further oxidation. As reported in the second final report a simple and reliable method has been developed allowing the preparation of single crystals with compositions up to O/U = 2.25. This was achieved by a controlled oxidation of UO_2 crystals in an oxygen atmosphere generated by the thermal dissociation of U_3O_8 .

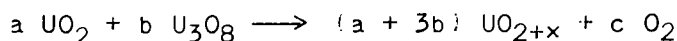
Two procedures have been used :

- the constant temperature method
- the constant pressure method.

a) *The constant temperature method*

If UO_2 and U_3O_8 are heated simultaneously in vacuum up to a fixed temperature, U_3O_8 will decompose. The oxygen liberated by the decomposition of U_3O_8 is distributed between the solid UO_{2+x} phase and its equilibrium gas phase.

One has :



The oxygen equilibrium pressures for UO_{2+x} as a function of temperature and composition are available from literature.

The UO_2 single crystals and a calculated amount of U_3O_8 are introduced into the same vacuum furnace. The latter is first evacuated whilst heating up to $800^\circ C$, and then shut off from the pumps. The temperature is next raised to $1400^\circ C$, the heating rate being about $2^\circ C \text{ min}^{-1}$.

b) The constant pressure method

Two zones of different independent temperature are created in a closed tube. Zone 1 contains the UO_2 single crystals and zone 2 the U_3O_8 powder. In this case, the oxygen pressure is determined by the temperature of zone 2 only. Instead of working at low total pressure, an inert gas (argon or helium) is introduced in the furnace up to a pressure of a few hundred torr. This makes the use of knife-edge seals and other special vacuum material superfluous. The partial oxygen pressure can not be measured during the experiment, but the equilibrium oxygen pressures over UO_{2+x} as reported by CHAPMAN and MEADOWS [1] again showed to be quite reliable.

The two methods proved to be suitable for the preparation of crystals of composition up to $UO_{2.25}$. A precision of 0.02 can be obtained for x in routine preparations.

Furthermore, another method has been worked out by which it is possible to oxidize UO_2 in oxygen at $1700^\circ C$ using Ta-Si based alloys as a crucible material. It has been found that after an oxidation to the composition $UO_{2.25}$ at $1700^\circ C$, followed by quenching in liquid nitrogen a single phase material UO_{2+x} is obtained.

2. STRUCTURAL INVESTIGATION BY OPTICAL MICROSCOPY

The morphology of the U_4O_9 precipitates in UO_{2+x} has been studied by observation of polished and stain-etched surfaces of oxidized UO_2 crystals in the optical microscope. The experimental conditions under which this investigation is carried out can be summarized as follows. Single crystals of UO_2 were oxidized to various oxygen excesses using the single or two oven method. The circumstances under which precipitation occurs have a certain importance. Therefore, the cooling rate after oxidation at $1400^\circ C$ is given in Fig. 1. The samples were polished on the precision grinder for diffusion work and then stain-etched according to the method of AMBLER and SLATTERY [2]. The procedure is as follows. The polished sample is immersed in hydrogen peroxide 30 % until the colour of the etched surface becomes blue-red (after about 2 min.). The sample is immediately rinsed with hot water and dried. In general, the precipitates appear light on a dark background, but reversion of the etching colours frequently occurs if the sample is etched a little too far.

The set of micrographs (Fig. 2 a-h) shows the morphology of the U_4O_9 precipitated in UO_{2+x} for various values of x . From these micrographs, the following observations can be made.

1* At low oxygen excess, i.e. $x < 0.015$, U_4O_9 precipitates clearly at lattice defects. Micrograph 2 a ($x = 0.013$) shows nearly continuous precipitation at the subgrain boundaries.

2* With increasing oxygen excess, i.e. $x > 0.015$, the second phase precipitates highly ordered, and marking of grain boundaries by precipitation of U_4O_9 was no longer observed; micrograph 2 i shows a grain boundary in $UO_{2.05}$, which can only be seen by the difference in orientation of the precipitates, and the difference in etching colour of the two regions.

The precipitation of U_4O_9 in the range from $x = 0.015$ to $x = 0.07$ was specially studied. In this range the U_4O_9 precipitates as platelets: see micrograph 2 b ($x = 0.04$). Micrographs 2 j, k and l show these platelets as seen in $\{100\}$, $\{110\}$ and $\{111\}$ planes. Combining these three micrographs, it can easily be stated that these platelets are exclusively oriented in the $\{111\}$ direction.

3* When the oxygen excess increases from $x = 0.07$ to $x = 0.25$, the morphology of the precipitates changes gradually to a more complex network: see micrographs 2 c and d ($x = UO_{2.08}$ and $UO_{2.11}$). The coherence with the original UO_2 lattice becomes more and more unclear, and at $x = 0.12$ (micrograph 2 e) bands of U_4O_9 start forming. These bands grow broader and broader with increasing oxygen excess: see micrographs 2 f and g. At $x = 0.23$ only isolated islands of UO_2 remain (micrograph 2 h) while at $x = 0.25$ (U_4O_9) the second phase has completely disappeared.

4* Some crystals were polished, oxidized and directly etched. This revealed a remarkable surface effect. Precipitation in the outermost layers to a depth of about 10 microns seemed to be quite different from precipitation in the bulk material. Micrographs 2 m, n and o show these surface precipitations in the $\{100\}$, $\{110\}$ and $\{111\}$ planes. The crystals are the same as for micrographs 2 j, k and l ($x = 0.056$).

The effect of reactor irradiation on the behaviour of U_4O_9 precipitates after various doses has also been studied by observation in the optical microscope. Two irradiation experiments were undertaken on UO_{2+x}/U_4O_9 crystals of different composition.

a) A crystal of composition $UO_{2.056}$ has been irradiated in the BRI reactor at a temperature of $80^\circ C$ to an integrated flux of about 1.7×10^{19} thermal neutrons. Fig. 3 shows the crystal before irradiation, Fig. 4 after irradiation. The structure of the U_4O_9 network is definitely more coarse: the thin edges of the platelets did dissolve and precipitated on the thicker parts.

b) Two crystals of composition $UO_{2.026}$ have been irradiated in the BR2 reactor to an integrated flux of about 10^{20} thermal neutrons. One sample was maintained between 133 and 159°C, the other one between 321 and 419°C.

Fig. 5 shows a micrograph of the structure before irradiation. After irradiation both crystals showed to be single-phased; hence, no precipitates of U_4O_9 could be detected by optical microscopy. Annealing experiments and irradiations on crystals of other compositions are in progress to learn more about the broadening of the solid solubility range of oxygen in UO_{2+x} during irradiation.

3. STRUCTURAL INVESTIGATION BY ELECTRON MICROSCOPY

The purpose of this study is to present electron microscopic evidence for the presence of anti-phase boundaries in U_4O_9 single crystal foils.

The single crystal foils were prepared by the chemical thinning of U_4O_9 single crystals made by carefully controlled oxidation of UO_2 single crystals. The chemical thinning was performed by means of hot orthophosphoric acid using a device developed by KIRKPATRICK et al [3].

It has already been suggested earlier that needle-shaped precipitates of U_4O_9 in oxidized UO_2 might contain periodic anti-phase boundaries [4]. The present evidence suggests the existence of non-periodic domain boundaries in U_4O_9 .

The exact crystal structure of U_4O_9 is still somewhat in doubt although it is now generally accepted that it is closely related to that of UO_2 and can be derived from this last structure by the systematic insertion of oxygen ions in the interstices of the calcium fluoride type structure of UO_2 . Since not all crystallographic equivalent interstices are filled in this process, the insertion can be achieved in several alternative ways. As a result one can imagine the formation of domains due to the fact that in different parts of the UO_2 host structure the insertion of oxygen ions may start according to a different scheme. More specifically, the uranium dioxide structure can be considered as a cubic close-packed arrangement of uranium ions with O-atoms in the tetrahedral interstices. Since N spheres give rise to 3N interstices (2N tetrahedral and N octahedral ones) the insertion of $\frac{1}{4}$ N oxygen ions (in the N remaining interstices) can be achieved in at least four different ways, whatever arrangement is used. We shall present evidence for the occurrence of at least four types of domains.

The evidence is contained in pictures such as Fig. 6 where domain walls are clearly visible as broad fringe patterns. It should be emphasized that the diffraction pattern corresponding to Fig. 6 only reveals the presence of a single crystal of U_4O_9 . The fringe patterns therefore do not mark grain boundaries. Their curved nature suggests very strongly that they are due to anti-phase boundaries rather than to stacking faults. This is further supported by the remark that the

boundaries only show up clearly when reflections characteristic of the U_4O_9 superlattice are strong.

The presence of triple points suggests that there should be at least three different ways of constructing the U_4O_9 structure in the UO_2 host structure. The details of the fringe patterns at triple points also support the hypothesis of the domain walls and further suggest that there are presumably four different filling schemes. We shall show this now by discussing the fringe pattern of Fig. 6 and Fig. 7.

It is clear that the fringes are rather broad ; also there are only one or at most two fringes. This is a consequence of the fact that the extinction distances associated with the superlattice reflections are very large. As a result the fringe patterns are reduced to the central fringe which, depending on the sign of $\sin \alpha$ ($\alpha = 2\pi g \cdot R$; g is the diffraction vector ; R is the displacement vector) is either bright or dark [5]. It is of interest to note that the fringes at the two triple points are as shown schematically in Fig. 8. Let us assume that the traces (a) are at the top and therefore (b) at the bottom. With this assumption we can determine for the four domains involved in Fig. 7 the sense of the slope of the walls and hence the sense of the displacement vectors for the five walls. It is clear that at a triple point the three domains must be displaced one relative to the other. One can conclude therefore that $I \neq II \neq III$. The slope of the walls (1) and (4) being in the same sense (i.e. III being in both cases the bottom part) but the fringe pattern being nevertheless different, it is concluded that $IV \neq I$, and since moreover $II \neq III \neq IV$ we conclude that at least four different arrangements are involved. It is easy to see that this reasoning leads to the same conclusion if it is assumed that (a) is the bottom trace. The same conclusion is reached when considering the equally sloping walls (1) and (4) ; if I and IV were packed according to the same scheme the signs of $\sin \alpha$ would be opposite for (2) and (5) and hence the nature of the central fringe would be different which is not the case. The last argument is valid only if (α_1) and (α_4) are different from π .

The observations described here suggest a possible explanation for some of the difficulties which have been encountered in determining the crystal structure of U_4O_9 . Any single crystal diffraction method will only yield a statistical structure, i.e. the average position of the O-atoms in octahedral positions in the different domains.

4. SURFACE ENERGY OF STOICHIOMETRIC UO_2

Artificial pores have been created inside single crystals of UO_2 by precipitation and dissociation of UN. These crystals have been annealed for 200 h at 1600-1700°C. The equilibrium shape of the pores remains unchanged after 5 h of annealing. Measurements of the shape of these "negative crystals" have been carried

out, and calculations have been made using the equations given by NELSON [6].

If a pore takes the form of a regular polyhedron consisting of eight {111} and six {100} faces, such as shown in Fig. 9, it is possible, by minimizing the total free energy expression :

$$\int \gamma dA = \sum_{hkl} A^{hkl} \gamma_{hkl}$$

to obtain the equilibrium relation

$$\frac{b}{a} = \frac{1}{\sqrt{2}} (\sqrt{3} \gamma^{111} / \gamma^{100} - 1)$$

in which a is the distance between opposite {100} faces, and b the side of the square {100} face.

Careful measurements of some hundred pores, between 10 and 35 μ in diameter, cut by a {100} plane (Fig. 10 a) and by a {111} plane (Fig. 10 b), allowed

the calculation of the ratio $\frac{\gamma^{100}}{\gamma^{111}}$.

A value of 1.19 ± 0.02 found by these measurements is in fair agreement with the theoretical value of 1.152 calculated for the f.c.c. structure by MACKENZIE [7].

The same crystal has been annealed at 1400°C for 100 h in an oxygen pressure corresponding to the composition $UO_{2.20}$ (single phase UO_{2+x}). After this treatment the pores regained a pure spherical shape, indicating a perfect isotropic surface energy for single phase $UO_{2.20}$, which loses the characteristic anisotropy of the f.c.c. structure.

5. LOW TEMPERATURE THERMAL CONDUCTIVITY

5.1. Introduction

The thermal conductivity of UO_2 single crystals has been measured from 4.2 to 300°K. The results obtained for stoichiometric UO_2 are compared with those of UO_2 containing a slight oxygen excess and with those obtained by BETHOUX et al. [8] with a sintered polycrystal.

5.2. Method of measurement and applied techniques

The classic stationary method has been used. The free end of the sample is heated with a constant and known calorific power. This heat is absorbed by the sample holder which is fixed to the other end of the crystal. The heat flux passing

lengthwise through the sample builds up a temperature gradient which is measured. Knowing the dimensions of the sample, one can thus calculate its thermal conductivity. The samples are of the parallelepiped shape with square basis of 2 mm side and 10 mm length.

In order to be able to perform measurements without having to stabilize the temperature, the technique of HOLLAND et al [9] has been applied. This consists in recording simultaneously all the magnitudes to measure, converted into electric tensions, on a recording potentiometer with several channels. The potential difference produced at the terminals of a differential thermocouple is measured to know the temperature gradient. This small potential difference (sometimes inferior to 1 μ V) is amplified and recorded through a Keithley microvoltmeter. The sample is supplied with a constant calorific power through an electric resistance fixed to the free end of the crystal. The voltage at the terminals of the heating resistance and the voltage drop caused at the terminals of a known resistance is recorded to know the current intensity, thus allowing to calculate the calorific power. Furthermore, the absolute temperature is also determined by recording, after amplification, the difference between a known tension, supplied by a potentiometer, and that of a thermocouple from which one welding is fixed to the sample holder and of which the other is kept at a reference temperature. Before being recorded all these voltages are adjusted by means of voltage dividers, so that they can be recorded in a same measurement scale (from 0 to 10 mV). It may be noticed that when the absolute temperature is being stabilized, it can also be measured with the aid of a gas thermometer (this has been done for temperatures below 50°K).

The measurements can thus be done in a continued way while the temperature increases or decreases. This allows to perform a large number of measurements within a relatively short time (10 measurements in one hour, or even more). Due to variation of the absolute temperature, a temperature gradient is produced in the sample even when it does not receive any calorific power. Therefore, the potential difference of the differential thermocouple with and without heating must be recorded alternatively. The difference between the two curves thus obtained, is proportional to the partial gradient produced by the calorific power.

5.3. Description of the apparatus

The cryostat is schematically presented in Fig. 11. Two single crystals (a) are simultaneously used. They are fixed upon a copper sample holder which is in good thermal contact with the gas thermometer (b). The temperature gradient of the samples is measured with a chrome/gold-cobalt (2.11 %) differential thermocouple. The measuring chamber (c) covered in a non-inductive way with a heating resistance (i) is being fixed inside of a second chamber (d) isolating it from the refrigerant (k). The space between the two rooms (c) and (d) may be put under

vacuum or filled with gaseous helium at the pressure wanted. When a pushed vacuum is realized between the chambers (c) and (d), the only contact between the measuring chamber (c) and the refrigerant (k) is composed of a stainless steel tube (m) which offers a high thermal resistance. So, it is easy to increase the temperature of the measuring room above that of the refrigerant by supplying a low electric power to the resistance (i). When supplying a constant power, the temperature of the measuring chamber may be stabilized at any value wanted. The chamber (d) and the junction box (e) where the chromel wires of the differential thermocouples are welded to the copper wires leading to the amplifiers, are immersed into the refrigerant (k) contained in a dewar (f). When the refrigerant is liquid helium or nitrogen, the outer dewar (g) is filled with liquid nitrogen.

Fig. 12 gives a detailed view of the mounting of the samples inside of the measuring room. Besides the two single crystals (a) and (c), serving directly for measuring the thermal conductivity, two additional samples (f) and (g) of identical composition and dimensions as the two first ones, are suspended to the sample holder by thin gold-cobalt wires. These wires are coupled to a chromel wire (i) to compose a differential thermocouple between (f) and (g). The sample (f) is also carrying a heating resistance. This device has been realized to permit measurement of the calorific power dissipated by the sample for a set temperature difference between the sample and the measuring chamber. This allows us to correct the obtained values for the thermal conductivity. This correction is small below 100°K and can, therefore, be completely neglected.

The connection box (e) which is immersed into the refrigerant permits to decrease the parasitic thermoelectric potentials produced at the junction of the chromel wires of the differential thermocouples with the copper wires connected to the amplifier. At temperatures below liquid nitrogen, the connection box is dipped into the liquid helium, so as to eliminate all the parasitic potentials.

5.4. Other technological properties of the apparatus

The gold-cobalt / chromel thermocouple has been chosen instead of the couple gold-cobalt / copper because of the much lower thermal conductivity of chromel against that of copper. In this way, the deviation between the temperature of the welding of a differential thermocouple and that of a point where this welding is fixed, is reduced to a maximum (the wires used are very thin : 75 microns). Moreover, the chromel also has a higher absolute thermoelectric power than that of copper.

Two samples (a) and (c) (Fig. 12), mounted on the sample holder (e), are used to reduce as much as possible the thermoelectric power produced by the parasitic gradient resulting from the absolute temperature variation. Each of them is carrying a differential thermocouple. These thermocouples are placed in series in

such a way that the gradients originating from the absolute temperature variation produce opposite thermoelectric powers. As their absolute value is almost equal, the total potential resulting from the parasitic gradient is rather small. Only one sample is measured. Therefore, the heating current is only supplied to the resistance (b) of (a), whereas the resistance (d) of (c) does not receive any current. During the heating of (a) the compensation of the potential due to the parasitic gradient also occurs. A similar procedure is realized with the samples (f) and (g).

Two types of heating resistances have been used. First, a graphite layer has been used, which was obtained by rubbing the small surface of the free end of the sample against a piece of graphite, and by removing the excess with a filter paper. The resistance then obtained varies between 1 and 10 $k\Omega$ (on a surface of 4 mm^2). While heating powers of the order of 100 μW are used, this permits to use very low current intensities. On the other hand, this heating resistance is in perfect thermal contact with the sample; moreover, it does not increase the surface of the sample, so that thermal losses are reduced to a minimum. Finally, its thermal and mechanical inertness are practically nil, so that the thermal equilibrium is very soon reached and the mechanical vibrations have little effect. However, this method has two disadvantages. First, the wires are difficult to fix to the free end of the sample and have a tendency to disconnect easily. On the other hand, when the electric resistance of the sample is not sufficiently high, this causes a parasitic potential in the differential thermocouple. In order to avoid these difficulties, the graphite layer has been replaced by a small slab of a KCl single crystal (sizes 7 x 2 x 0.5 mm^3) welded to the free end of the sample. Upon this slab a thin layer of nichrome has been previously deposited by evaporation. Contact wires are soldered into two small holes at each end of the plate. Although this solution is less perfect than the first one in view of the inertness and the thermal losses, it nevertheless gives good results and does not show the errors of the former.

5.5. Experimental results

The thermal conductivity of a UO_2 single crystal has been measured before and after complete reduction. On another single crystal it has been measured after complete reduction.

Some characteristics of the crystals used in this investigation are given in Table I. The compositions of the samples are evaluated from their electrical conductivity values at room temperature.

TABLE I

Crystal	Treatment	Electrical conductivity ohm ⁻¹ cm ⁻¹	Evaluation of O/U ratio	Curve number in Fig. 13
1	before reduction	1.7×10^{-3}	≥ 2.001	1
1	after reduction	1.7×10^{-5}	< 2.001	2
2	after reduction	2.5×10^{-6}	< 2.001	3

The thermal conductivity measurements have been performed from 4° to 300°K. The experimental results are shown in Fig. 13 (curves 1, 2 and 3). Curve 4 of this diagram corresponds to measurements made by BETHOUX et al [8] on a specimen of sintered UO₂ of apparent density 9.97 and for which the authors admitted a nearly stoichiometric composition.

The curves obtained with both reduced crystals coincide very well in the whole temperature region. A maximum in the thermal conductivity is found at 6.2°K. After a slight oxidation the thermal conductivity decreases markedly at very low temperatures. The maximum in thermal conductivity of the reduced crystal is about ten times higher than this of the slightly oxidized one. Moreover, this maximum is shifted towards higher temperatures for the slightly oxidized specimen (from 6.2°K to 12°K).

The equation which relates the thermal conductivity with the phonon mean free path is well known :

$$k = \frac{1}{3} c v l$$

Here, k is the thermal conductivity, c the specific heat, v the sound velocity ($\approx 4.2 \times 10^5$ cm s⁻¹ for UO₂) and l the phonon mean free path.

Using the experimental data of the thermal conductivity obtained on the oxidized and reduced crystals and the heat capacity data [10], the phonon mean free path has been calculated. In Fig. 14 the calculated l values are plotted versus the absolute temperature.

6. ELECTRICAL PROPERTIES

6.1. Introduction

When stoichiometric UO₂ is slightly oxidized the excess oxygen enters interstitial positions in the lattice. The additional oxygen atoms may be distri-

buted either at random, forming the UO_{2+x} phase, or in an ordered way forming the U_4O_9 superstructure.

In UO_{2+x} the excess interstitials are doubly negatively charged ions. The introduction of these O^{--} ions results in a conversion of nearby U^{4+} ions into one U^{6+} or two U^{5+} ions. At absolute zero these holes are bound to the interstitial excess oxygen ion. At normal or higher temperatures an appreciable number of these holes become free and will contribute to the electrical p-type conductivity in the presence of an applied external electric field. The number of free holes is as usual found from Fermi-Dirac statistics and it is one of the purposes of the undertaken research to find estimates for the ionization energies. This involves, in particular, the necessity for a very strict and careful control of the composition, during the measurements, which is especially difficult to realize at higher temperatures due to the very low oxygen equilibrium vapour pressure.

In U_4O_9 on the other hand, electrical conductivity is n-type but arises also if the composition deviates from stoichiometry. Excess electrons can now be produced by the removal of oxygen ions from the U_4O_9 lattice, converting adjacent U^{5+} ions to U^{4+} ions. The U^{4+} ions associated with the oxygen vacancies can be considered as donors.

It is well known that band theory does not describe correctly the electronic properties of a number of compounds, especially oxides and ionic crystals. This is due to the fact that the interaction between the conduction electrons and the phonons is very important in these compounds and plays an essential rôle.

Two important cases can be distinguished in this respect, depending on the magnitude of the three-dimensional periodic potential $V(r)$, experienced by the electron if the latter would not induce a polarization.

- a) The potential $V(r)$ is weak but the electron-phonon interaction is not a small perturbation. In that case an effective mass approach can be used but the polarization induced by the electron contributes to the inertia of the system (resulting in an effective mass different from that in the case without polarization) and lowers its energy. This case has been treated with a continuum polaron.
- b) It is also possible that the potential $V(r)$ is "strong" (strongly bound electrons). The starting point then is a localized state of the electron (L.C.A.O. approximation). The introduction of the electron-phonon interaction then causes a further localization of the electron. The small overlap between the wave functions of the electron at neighbouring sites induces transitions of the electron between different sites which involve multi-phonon processes at high temperature ("hopping" mechanism). The localized electrons together with their induced lattice polarization are called "small polarons".

Formally the cases a) and b) are only different in that in their Hamiltonian the energy of the electron in the unpolarized lattice is written differently. In case a) the potential $V(r)$ is accounted for by introducing an effective mass in the kinetic energy term. In case b) the potential $V(r)$ has to be treated separately. In spite of the formal similarity of both cases many properties of the compounds a) and b) are totally different. In particular the mobility behaves as $\mu_L \propto e^{-h\omega/kT}$ for large polarons ($h\omega$ is the energy of an optical phonon) and as $\mu_S \propto e^{-\eta h\omega/kT}$ for small polarons, where η is related to the coupling strength between electrons and phonons.

Typical compounds of the type a) are the alkali halogenides and the silver halogenides. Type b) materials are mostly oxides which recently have been studied in terms of the small polaron concept. Many oxides (e.g. transition metal oxides) have a trend for a small overlap between the wave functions of conduction electrons on neighbouring sites. So in studying UO_2 single crystals we took into account the possibility of having a strong potential $V(r)$. As these oxides and especially UO_2 are largely of the ionic type, a strong electron-phonon interaction can result and therefore we expected UO_2 to belong to the class of compounds described sub b).

In order to obtain a better understanding of the electronic conduction mechanism in UO_2 , experiments on the electrical conductivity, the thermoelectric power and the Hall effect in UO_2 were undertaken on UO_2 single crystals of well-defined composition.

6.2. Resistivity and Hall effect measurements

6.2.1. Experimental procedures

The four probe method of VAN DER PAUW [11] has been used to determine the electrical conductivity and the Hall coefficient. The samples have the shape of small platelets of 4×4 mm with a thickness of about 300 μ m. The Hall voltage which has to be detected is extremely small. The Hall signal is measured by a dc technique in a static magnetic field of 8,000 Gauss, using a Dieselhorst potentiometer, a galvanometer amplifier and a Kipp Micrograph recorder. With this set-up, we are able to detect Hall voltages as low as a few microvolts and even a few tenths of a microvolt, if the resistance of the sample does not exceed 10 $k\Omega$.

6.2.2. Results and discussion

Conductivity data obtained on crystals with O/U ratios smaller than 2.001 are shown in Fig. 15 (O/U = 2.001 is the maximum sensitivity of the chemical analysis; the exact composition of these samples can therefore not be given). In the temperature region between 120° and 300°K, $\log \sigma$ depends linearly on the

inverse temperature. The values of the activation energy, calculated from the slope of the curves vary between 0.22 and 0.26 eV. At temperatures higher than 300°K the log σ curves deviate gradually from the linear behaviour.

Conductivity measurements have also been performed on more oxidized crystals. Fig. 16 gives the complete set of conductivity data of crystals with O/U ratios ranging from < 2.001 up to 2.18. As shown by observations in the electron microscope, all the crystals with O/U > 2.001 are in the two phase region. Crystal 8 clearly shows a more rapid rise in conductivity above 200°C. From the phase diagram of UO₂, it can be deduced that the phase boundary between UO_{2+x} and UO_{2+x} + U₄O_{9-y} is situated around 200°C for a composition O/U = 2.007; the break in the conductivity curve therefore corresponds to a phase transition. For crystals with O/U ratios between 2.05 and 2.18 the UO_{2+x} single phase region is at much higher temperatures (around 950°K for x = 0.05). The Hall coefficient of a crystal with O/U \approx 2.001 has been measured at temperatures ranging from room temperature up to 400°C (Fig. 17). It can be noticed that the Hall coefficient shows an anomalous behaviour in this temperature range: below 50°C the Hall coefficient is negative, whereas heating above 100°C results into a change to p-type conduction. It is believed that this behaviour is due to a surface effect. Even at low temperature a highly oxidized surface layer is rapidly formed on UO₂ by diffusion of oxygen from the surrounding atmosphere into the lattice. The surface region, probably having the U₄O_{9-y} structure (n-type), may form an inversion layer on the bulk material. This view is supported by the fact that the same UO_{2.001} crystal became p-type at room temperature after a short reduction with hydrogen at 800°C. Another argument is that the reversal of sign occurs around 100°C, a temperature where we know from the annealing experiments on quenched UO_{2+x} crystals (see this report) that the interstitial oxygen becomes mobile in the lattice. So it can be assumed that heating up to about 100°C causes an homogenization of the excess oxygen in the lattice, thereby eliminating the surface effect.

In order to avoid this anomalous effect, Hall coefficient measurements have been carried out on a slightly reduced crystal (x < 0.001) in the temperature range between 200° and 550°C. The Hall mobility of holes (calculated using the usual formula $\mu_H = R_H \times \sigma$) is shown in Fig. 18. Notice that the Hall mobility increases exponentially with temperature. At 200°C μ_H is equal to about $4 \times 10^{-2} \text{cm}^2 \text{V}^{-1} \text{s}^{-1}$, whereas at 550°C μ_H equals $1.2 \times 10^{-1} \text{cm}^2 \text{V}^{-1} \text{s}^{-1}$. The mobility activation energy deduced from the slope of the curve corresponds to about 0.12 eV. The activation energy associated with the conductivity is found to be equal to 0.22 eV.

The Hall coefficient of crystals with composition UO_{2.05} and UO_{2.10} shows also a reversal of sign around 100°C (Fig. 19 and 20). The samples used here are in the two phase region: the p-type UO_{2+x} phase and the n-type U₄O_{9-y} phase are both present. From the appearance of n-type conduction below 100°C it has to

be concluded that either negatively charged current carriers, released from the oxygen vacancies of the U_4O_9 precipitates predominate at low temperature, or that the mobility of the electrons is much higher than of the holes ; both effects can of course contribute. On heating two phenomena may happen : 1) the oxygen vacancies in the U_4O_9 lattice are presumably filled by migrating oxygens (annealing effect) and 2) by further increasing temperatures the U_4O_9 precipitates dissolve gradually due to the increasing oxygen solubility in the UO_2 lattice.

Crystals with $O/U = 2.14$ and 2.15 are p-type in the whole temperature range (Fig. 21 and 22). The Hall coefficient decreases exponentially with increasing temperature, the associated activation energy being equal to 0.10 and 0.09 eV respectively. The Hall mobility is of the order of $10^{-2} \text{cm}^2 \text{V}^{-1} \text{s}^{-1}$ at room temperature.

In Fig. 23 the Hall mobility of crystals with O/U ratios varying between 2.05 and 2.15 is represented versus the reciprocal temperature. Only these values have been plotted where the sign of the Hall coefficient indicates that the samples are in the p-type region. The Hall mobility increases exponentially with temperature, the activation energy being within the range $0.11 - 0.14$ eV (Table II).

TABLE II

O/U ratio	Activation energy for conduction (eV)	Ionization energy of acceptor centres (eV)	Mobility activation energy (eV)
< 2.001	0.22	0.10	0.12
2.05	0.22	0.11	0.11
2.10	0.21	0.08	0.14
2.14	0.21	0.10	0.11
2.15	0.21	0.09	0.12

The Hall mobilities of the reduced crystal ($O/U < 2.001$) and of the more oxidized ones are in good approximation the same, and this in the whole temperature range. One is forced to assume that the U_4O_9 precipitates act more or less as insulating particles in the two phase $UO_{2.14}$ and $UO_{2.15}$ samples and also in the $UO_{2.05}$ and $UO_{2.10}$ ones but after the annealing treatment resulting into p-type. The introduction of insulating regions in semiconductors does not influence to a large extent the conductivity and the Hall coefficient. In the special case of uniformly distributed insulated particles JURETSCHKE et al [12] found that the measured value of Hall mobility μ_M is related to the bulk value by

$$\mu_M = \mu_H (1 - f/4)/(1 + f/2)$$

where f is the fraction of the crystal volume occupied by the spherical regions.

For a $UO_{2.15}$ specimen, where 60 % of the total volume is occupied by U_4O_9 , this would represent a difference of 35 % between the measured and the real Hall mobility.

What can one conclude now about the electronic conduction in UO_{2+x} . Firstly, it should be pointed out that the theory of the Hall effect in hopping conduction is rather controversy. Although starting from the same Hamiltonian, the theories developed by different authors give completely different results for the temperature behaviour of the Hall mobility. According to the earliest theory by FRIEDMAN and HOLSTEIN [13], the Hall mobility of the small polaron in the hopping region increases exponentially at rising temperature. Later theories by FIRSOV [14] and KLINGER [15] resulted in an exponential decrease of the Hall mobility. On the other hand SCHNAKENBERGH [16] who reinvestigated the theory of the Hall effect in a small polaron semiconductor starting from the Kubo formula, found only a slight variation of the Hall mobility with temperature. Recently FRIEDMAN [17] presented physical arguments to support the idea that the Hall mobility has a thermally activated nature.

Due to this contradiction in the existing small polaron theories one is not in the position of definitely establishing the type of conduction in UO_{2+x} if one considers only the analysis of the Hall mobility. Particularly interesting, however, is the behaviour of the drift mobility deduced from conductivity and thermoelectric power measurements [18] [19]. The temperature dependence found here can be expressed as $\mu_H \propto \exp[-E/kT]$ which is typical for small polarons. Therefore, if the small polaron model really holds for UO_{2+x} , the temperature dependence of the Hall mobility found by experiment is in agreement with the theory of Holstein and Friedman. From the examination of their thermoelectric power data Wolfe and De Coninck concluded to an ionization energy of about 0.08 eV. By subtracting this value from the total activation energy for conduction (for the samples used in the Hall effect measurements) this energy is equal to about 0.26 eV if one plots $\ln \sigma^{3/2}$ vs $\frac{1}{T}$ according to the theory of Holstein and Firsov one finds an activation energy for the drift mobility of about 0.18 eV. So the Hall mobility ($E \simeq 0.12$ eV) depends to a lesser degree upon temperature than the drift mobility. However, μ_H does not show an activation energy equal to 1/3 of the activation energy for the drift mobility as predicted by Holstein's theory.

6.3. Thermoelectric power measurements

6.3.1. Introduction

An apparatus for thermoelectric power and resistance measurements has been constructed. Measurements have been made on several crystals of various O/U ratios ($0 < x < 0.25$) as a function of temperature. UO_{2+x} shows p-type conductivity up to compositions of the order $O/U = 2.12$. At higher oxygen excess n-type conductivity is observed.

The result of neutron irradiation and quenching has also been studied.

The measurements of thermoelectric power have shown to give valuable information about the nature of the conduction mechanism in UO_2 .

6.3.2. The apparatus

a) Method of measurement

The measurement of the thermoelectric power (T.E.P.) consists in the determination of a ratio $\frac{\Delta E}{\Delta T}$. Here ΔE is the thermal emf measured between two points of the sample, which are brought at a temperature difference ΔT . This ratio is defined as the thermoelectric power at the average temperature $T_a = \frac{T+(T+\Delta T)}{2}$. A positive sign of the T.E.P. signifies a positive voltage at the cold junction. The material is then p-type.

The technique adopted here for measuring the thermoelectric power consists in slowly varying the average absolute temperature of the sample and maintaining the temperature difference as constant as possible. The potential difference produced at the terminals of a differential thermocouple is measured to calculate the temperature gradient ΔT .

b) Description of the apparatus

All measurements are carried out in a cryostat of all metal construction cooled by liquid nitrogen (Fig. 24). The sample holder is placed in the central tube of the cryostat. This holder consists of two cylinders which can be heated or cooled separately. Two chromel-P alumel thermocouples are pressed with the help of springs on the surface of the sample, the ends of which are in contact with two copper plates (Fig. 25). These are electrically insulated but in good thermal contact with the two cylinders. The contact between the thermocouples and the sample surface was found to be ohmic.

A switch system (Fig. 26) permits the following measurements: the two thermocouples separately and their difference by a Tinsley type potentiometer; the thermoelectric voltage by a Wayne Kerr electrometer type M 141 and the resistance by a Lemousy electrometer-ohmmeter.

Fig. 27 gives a general view of the apparatus.

c) Measurement range and reproducibility

In the actual set-up, measurements can be carried out in the range 77° to 450°K. The lowest temperature reached during the measurements is governed by the resistance of the sample (maximum 5×10^9 ohm). The smallest detectable

thermoelectric voltage is about $2\mu\text{V}$, whereas the temperature difference can be measured with a precision of about 0.01 deg.

All measurements are done under vacuum (10^{-5} to 10^{-6} mm Hg). Since the highest temperature of measurement is about 450°K, oxidation of the UO_2 samples is avoided.

The reproducibility reaches 2 to 3 %. It depends, in particular, on the insulation and the electrical shielding of the thermocouple wires on their thermal contact with the crystal, on their thermal conductivity and also on the constancy of the reference temperature (melting ice).

Resistivity values of the samples are calculated from the resistances measured between two points. Systematic errors in these absolute values may arise from the dimensions of the samples which are difficult to estimate correctly.

The thermocouples were calibrated against tables of standard chromel-alumel thermocouples [20]. To calculate the absolute thermoelectric power, corrections for the measuring wires (chromel and alumel) were made.

To check reliability following measurements were performed : 1) the thermoelectric power during two temperature runs, each with a temperature gradient in the opposite direction ; 2) the thermoelectric voltage as a function of ΔT at a given T_a ; 3) the thermoelectric power once against the chromel wires and once against the alumel ones.

6.3.3. *Crystal treatments*

All crystals were sandblasted to clean the surface and were carefully inspected for irregularities.

On four crystals (B, D, H and one with known composition $\text{O/U} = 2.0023$) Au-5 % Ta contacts were alloyed by heating to about 1200°C for 1 or 10 min. In this case the measurements were done with the pressure contacts either applied directly to the crystal surface or to the alloyed contacts.

To obtain nearly stoichiometric crystals, reductions under hydrogen with a pressure of 10 to 20 cm Hg were carried out in an UO_2 crucible placed in a high frequency furnace. Temperatures of 1400°C and times varying between 10 and 20 min were used. Further reductions are executed in a U-shaped quartz tube, carefully evacuated and rinsed with hydrogen. After filling with 10 to 20 cm Hg of hydrogen gas one arm of the tube containing the UO_2 sample is heated to about 1000°C for 1 to 1.5 hour. The other arm of the tube is immersed in liquid nitrogen and serves as a trap for the water formed from the residual oxygen. After heating, some crystals of nearly stoichiometric composition were quenched by dropping into liquid nitrogen. Some other crystals were irradiated in the BR facility [21]. These

irradiations were done in evacuated quartz capsules. Integrated thermal flux measurements were made by Co detectors adjacent to the crystal.

6.3.4. Results and discussion

a) Non-stoichiometric crystals

Fig. 28 represents the thermoelectric power of oxidized crystals as a function of the reciprocal temperature.

The crystals with compositions between 2.05 and 2.17 are p-type at low temperatures. They change to n-type conductivity at higher temperatures (at about 160°K for a $UO_{2.17}$ sample and around 350°K for a $UO_{2.11}$ one). All crystals with higher oxygen excess are n-type in the whole temperature range investigated.

b) Nearly stoichiometric crystals ($0 < x < 0.005$)

Special attention has been drawn to nearly stoichiometric crystals. The main reason for this is that in these samples the content of the U_4O_9 superstructure phase is small and hence will have only a minor influence on the properties of the UO_{2+x} phase.

The T.E.P. of the as-grown crystals ($O/U \simeq 2.006$) is always p-type. Its value is higher than of the oxidized specimens. A straight line is generally obtained if the T.E.P. is plotted as a function of the reciprocal temperature (Fig. 29). The electrical conductivity was measured only for two as-grown specimens at temperatures ranging from 110°K to 300°K (Fig. 30).

Measurements were also performed after reducing the as-grown crystals. Fig. 31 shows T.E.P. curves of four as-grown crystals (designated by the letters E, F, H and I) before and after reduction. In Fig. 32 all the results of T.E.P. measurements on several reduced crystals are plotted. After reduction straight lines are obtained in most cases. Nevertheless, some of the samples yield slightly bended lines, even after several subsequent reductions.

c) Discussion of the T.E.P. results

Most of the previous T.E.P. measurements by other authors [18] [22] [23] [24] on nearly stoichiometric UO_2 are represented in Fig. 33. These curves were calculated from the data originally plotted versus T. The best measurements are those of Wolfe and those by Aronson et al. ; they refer to compositions 2.003 and 2.001, respectively. Some of our curves are also shown in the same graph (the highest and lowest curve obtained for reduced crystals, as well as the results for as-grown samples and for a $UO_{2.17}$ one). From the figure it can be noticed that the behaviour of the different curves is quite similar. In the temperature range from 1850° to 170°K one can distinguish two distinct parts. Starting from

high temperatures, a first straight part extends to between 1200° and 1000°K. In most cases the second part can also be represented by a straight line and extends to temperatures between 250° and 170°K. Measurements to lower temperatures were not possible due to the high resistance of the samples.

The region between 1000° and 170°K, where the plot of the T.E.P. (S) versus the reciprocal temperature gives a straight line, corresponds to the general formula for an extrinsic non-degenerate semiconductor

$$S = \frac{k}{e} \left(A + \frac{U}{kT} \right) \quad (1)$$

Here e is the electronic charge ;

k is the Boltzmann constant ;

U is the separation between the Fermi level and the edge of the relevant energy band ;

and A is a constant which depends on the mechanism of carrier scattering.

Using the relation

$$p = P \exp [- U/kT] \quad (2)$$

eq. (1) can be transformed in

$$S = \frac{k}{e} \left(A - \ln \frac{p}{P} \right) \quad (3)$$

P represents the number of available energy levels per unit volume and p the number of charge carriers per unit volume.

The activation energy U (in eV) and the parameter A calculated with the help of formula (1) for those specimens which give straight lines in the temperature interval are tabulated in Table III.

TABLE III

Crystal	As-grown		Reduced	
	U (eV)	A	U (eV)	A
A	0.066	6.14		
E	0.079	5.07	0.112	6.22
F			0.086	7.77
H	0.083	4.45	0.066	8.85
L			0.045	8.09
N			0.052	8.28
T			0.074	6.57
U			0.064	6.57
Mean values	0.076	5.22	0.074	7.36

In Table IV the activation energies for conduction calculated from the expression

$$\sigma = A \exp [- E/kT] \quad (4)$$

are collected. Some of our conductivity measurements of nearly stoichiometric crystals, together with those of Bates, Wolfe and Karkhanavala are shown in Fig.34. It can be noticed that the σ -curves deviate from linear behaviour above about 300°K. If the small polaron theory is applicable to UO_2 one expects the conductivity σ to be proportional with $\frac{e^{-E/kT}}{T^{3/2}}$. Therefore, values of $\log \sigma T^{3/2}$ have been plotted versus the reciprocal temperatures.

TABLE IV

Crystal	As-grown E(eV)	Reduced	
		E(eV)(1)	E(eV)(2)
α	0.189		
XVIII	0.195		
N		0.216	0.236
O		0.226	0.250
P		0.248	0.274
S		0.275	0.312
T		0.218	0.236
U		0.209	0.228

(1) calculated using $\sigma \propto \exp [- E/kT]$

(2) calculated using $\sigma T^{3/2} \propto \exp [- E/kT]$

This is shown in Fig. 35 and 36. Using this $\sigma T^{3/2}$ versus $\frac{1}{T}$ dependence values of the activation energies for conduction have been calculated. They are also given in Table IV.

d) Quenching of reduced crystals

Several reduced crystals were quenched in liquid nitrogen after heating to around 900°C. This thermal treatment does not change markedly the value of the thermoelectric power. The results obtained on three different samples (N, T and U) are represented in Fig. 37, 38 and 39. In all these cases the resistance decreases, mainly by a factor of two (see the same figures).

e) Neutron irradiation and annealing

Measurements on irradiated crystals have been started. Five crystals (F, I, L, N and O) were submitted to thermal neutron doses varying between 7×10^{14}

and 10^{16} nvt (Fig. 40, 41, 42, 43 and 44). Some of them were afterwards annealed either at a temperature of 140°C or at about 300°C .

It is difficult to associate directly the change of the electrical properties of the specimens with the integrated thermal neutron flux. Very irregular results are found.

At first sight a rather surprising behaviour of the thermoelectric power after irradiation is obtained.

Indeed, a decrease of the number of free holes captured in hole traps would imply an increase of the absolute value of the thermoelectric power; however, a decrease is measured and in some cases a maximum appears in the curve.

Before irradiation the electrical conductivity is a complete straight line over about five decades in the higher temperature region. At lower temperatures a bending to higher values is nearly always found. As suggested by ACKET [25] this bending at low temperatures can be explained on the assumption of n-type impurity conduction. This hypothesis could not be confirmed by our thermoelectric power measurements on unirradiated crystals due to the high resistance of the samples at low temperatures. However, the behaviour of the thermoelectric power after irradiation might be explained by considering the rôle played by impurity conduction.

The thermoelectric power of a single semiconductor which has two independent groups of charge carriers, e.g. p- and n-type, with conductivities σ_p and σ_n respectively, and such that each group, if acting alone, would have a thermoelectric power S_p and S_n respectively is

$$S_t = \frac{S_p \sigma_p + S_n \sigma_n}{\sigma_p + \sigma_n} \quad (5)$$

with

$$S_p = \frac{k}{e} \left(A - \ln \frac{p}{P} \right) \quad (6)$$

$$S_n = \frac{k}{e} \left(B - \ln \frac{n}{N} \right) \quad (7)$$

$$\sigma_p = p e \mu_p \quad (8)$$

$$\sigma_n = n e \mu_n \quad (9)$$

p and n are the numbers of holes and electrons, P and N the corresponding density of states and A and B are constants connected with the kinetic energy of the charge carriers.

At low temperatures part of the holes will be trapped after neutron irradiation and the "impurity" conduction becomes relatively more important. As the

impurity conduction is n-type, the thermoelectric power tends to lower values. The maximum in S_T which is characteristic for impurity conduction will shift to higher temperatures: indeed the temperature at which it occurs is related to the temperature at which $\sigma_n \simeq \sigma_p$. The effect of irradiation realized this equality at higher temperatures. This explains why a maximum is observed after irradiation.

Concluding, the bending of the conductivity curves at low temperatures suggests the possibility of n-type impurity conduction. This hypothesis is confirmed by an analysis of the thermoelectric power as a function of temperature after neutron irradiation. After irradiation a maximum in S_T appears. This maximum which was not seen in the results on unirradiated crystals shifts to higher temperatures because irradiation causes a decrease in the number of holes and hence enhances the effect of impurity conduction. By irradiation we have shifted the maximum from an inaccessible to an accessible temperature region.

6.4. Some theoretical considerations about the conduction mechanism in UO_2

The thermoelectric power of UO_2 is, in an important temperature range, well represented by

$$S = \frac{k}{e} \left(A + \frac{U}{kT} \right) \quad (10)$$

First, the meaning of the activation energy U will be considered here.

The hopping type motion of small polarons and their resultant mobility can be reasonably well approximated as being a diffusion process. Therefore, it is indicated to consider the same analogue to study the thermoelectric power of the low mobility semiconductors like UO_{2+x} .

In ionic crystals there are at least two kinds of oppositely charged defects and the effect of a temperature gradient is to separate these charges. One is tempted to write the following equation to describe the current density of one of the defects α (say an interstitial ion)

$$Y_\alpha = \sigma_\alpha F - q_\alpha D_\alpha \frac{\delta n_\alpha}{dx} - q_\alpha n_\alpha \frac{\delta D_\alpha}{dx} \quad (11)$$

This equation can also be written as

$$Y_\alpha = \frac{n q_\alpha D_\alpha}{kT} \left[q_\alpha F - (U_\alpha^n + U_\alpha^\mu) \frac{1}{T} \frac{\delta T}{\delta x} \right] \quad (12)$$

where q_α is the charge of the interstitial ion ;

D_α its diffusion coefficient ;

F is the electric field strength ;

U_α^n is the activation energy for the number of defects ;

U_α^μ is the activation energy for their mobility ;

$\frac{\delta T}{\delta x}$ represents the temperature gradient.

To obtain the last term in eq. (12) one considers the ion α in its potential well and expresses its jump probabilities as a function of the depth of this well (local functions).

The argument is similar to that leading to the second term.

If one of the two defects α and β (opposite charges), say β , is much less mobile, then the other one obtains an expression for the T.E.P. of the same form as (10) with

$$U = U_{\alpha}^n + U_{\alpha}^{\mu} \quad (13)$$

The analogy would then indicate that the activation energy for the thermoelectric power in UO_{2+x} is the same as that for the electrical conductivity, a result which is in contradiction with experiment.

A similar difficulty occurred in the study of the effect of a temperature gradient on the migration of solute in a solid (thermal diffusion, Soret effect) where it was thought on the basis of simple arguments that there existed a parallel between the temperature dependence of the mobility and the Soret effect.

However, if the problem is treated with the thermodynamics of irreversible processes one arrives at the same equation (3) for γ_{α} except that U_{α}^{μ} is replaced by Q_{α} , the so-called heat of transport. HOWARD and LIDIARD [26] define this heat of transport thermodynamically as follows: if we imagine two neighbouring parts of the system (I and II, say) maintained at temperatures T and $T + dT$, respectively, and if one defect i jumps from region I to region II, under conditions of constant pressure, then Q_i is defined as the heat absorbed by I and developed by II in such a way as to preserve their initial temperatures.

Although thermal diffusion in solids is not very well understood some insight into the significance of Q_{α} can be obtained by a kinetic model for the atomic jump process. This model was proposed by WIRTZ [27]. Wirtz argues that the probability for a jump of the interstitial ion from the position A to the position B (at a different temperature) will be affected not only by the situation A (as supposed in deriving (11) but also by both the situation in B and between A and B (so these probabilities are non-local functions). He assumes that the activation energy U_{α}^{μ} consists of three parts: U_H , the energy which must be given to the ion at A (Hemmungsenergie), U_R , the energy which must be given to bring the ions between A and B in positions which permit an easy transition from A to B (Rückschwingungsenergie). Finally, due to the dimensions of the interstitial ion or to specific interactions with the lattice it is possible that also the neighbourhood of B should be in a high energy configuration to enable that the ion is trapped at B. The energy necessary to establish this high energy configuration is U_L (Lochbildungsenergie).

Writing the conditions for zero net flux in terms of these different energies (leading to a non-local jump probability) Wirtz finds

$$Q^* = U_H - U_L \quad (14)$$

Although the argument of Wirtz is crude, it still is a refinement of eq. (11) and permits to understand qualitatively why $Q_\alpha^* \leq U_\alpha^\mu$. Therefore, the apparent difficulty resulting from (13) is, at least in principle, removed.

From these arguments it is logical to expect that the experimental value for U is an upper limit for the activation energy of the number of carriers in UO_{2+x} and that part of it is presumably related to the activation energy for the drift mobility.

The values for the activation energies for the electrical conductivity of uranium dioxide crystals with different excess oxygen content range from 0.19 eV to 0.34 eV. The T.E.P. measurements reveal typical U values between 0.05 and 0.08 eV. The foregoing discussion on the T.E.P. then leaves us with an uncertainty of 0.07 eV on the activation energy for the drift mobility. So for a crystal with $U_\sigma = 0.19$ eV, we expect $0.12 \text{ eV} < U_\mu \leq 0.19 \text{ eV}$. For all the crystals one then expects $0.12 \text{ eV} < U_\mu < 0.34 \text{ eV}$.

Now we want to calculate the activation energy for the drift mobility on the basis of small polaron theory in order to compare with the experiment.

Comparison between theory and experimental data was difficult until recently because of the lack of experimental data on the static dielectric constant (ϵ_0) and the frequency of the optical longitudinal phonons (ω_0). Recently these data became available

$$\epsilon_s \simeq 24 \quad [28]$$

$$\nu_0 \simeq 1.7 \times 10^{13} \text{ Hz} \quad [29]$$

while ϵ_∞ (the high frequency dielectric constant) is known to be about 5.5 [30]. The knowledge of these data enables now to compare theory and experiment.

Of the different small polaron theories we will consider here the treatment of LANG and FIRSOV [31] which, except for some details (like the appearance of an intermediate temperature region), is the three-dimensional extrapolation of Holstein's theory. The expression for the activation energy E_a obtained by Lang seems reliable.

For $kT_0 \gg \frac{\hbar\omega_0}{4}$ Firsov's method predicts an activated drift mobility, the activation energy being given by

$$E_a = \frac{1}{N\beta} \sum_k |\gamma_k|^2 (1 - \cos k g) \text{tgh} \frac{\hbar(\omega_k)}{4} \quad (15)$$

where $\beta = \frac{1}{kT}$

N is the number of elementary cells in the crystal ;

ω_k is the frequency of the optical phonons with wave vector k ;

g is a lattice vector ;

and

$$|\gamma_k|^2 = \frac{4\pi e^2}{k^2 \Omega \kappa(\omega_0)} \left(\frac{1}{\epsilon_\infty} - \frac{1}{\epsilon_0} \right) \quad (16)$$

where Ω is the volume of the elementary cell.

At high temperatures $\tanh \frac{\kappa \omega_k \beta}{4}$ can be replaced by its argument. Furthermore, one takes $\omega_k = \omega_0$. The expression for the electron-phonon coupling constant is

$$\gamma = \frac{1}{2N} \sum_k |\gamma_k|^2 \quad (17)$$

In order to compare theory and experiment one has to approximate the summations over k . For this purpose a procedure introduced for a similar case by YAMASHITA and KUROSAWA [32] and EAGLES [33] was used here. It consists in replacing the sum over the k vectors by an integration over the first Brillouin zone. As UO_2 is an "isotropic" material it is a reasonable approximation to replace the Brillouin zone by a sphere. The radius of this sphere is well approximated by $k_B \approx \frac{2\pi}{a}$ where a is the lattice parameter (there are four elementary cells in the volume a^3). The integration gives

$$\gamma = \frac{2e^2}{a} \frac{1}{\kappa(\omega_0)} \left(\frac{1}{\epsilon_\infty} - \frac{1}{\epsilon_0} \right) \quad (18)$$

The calculate E_a the same method was used. The z -axis was taken in the g -direction.

The result is

$$E_a = \frac{e^2}{a^2 k_B} \left(\frac{1}{\epsilon_\infty} - \frac{1}{\epsilon_0} \right) [ak_B - \text{Si}(ak_B)] \approx 0.31 \gamma \kappa \omega \quad (19)$$

An expression similar to (18) also occurs in Eagles' work. This shows that this theory is basically similar to Firsov's. Introducing the experimental data on UO_{2+x} in (18) and (19) we find for the coupling parameter

$$\gamma(UO_2) = 10.5$$

and for the activation energy of the drift mobility for $T \gg T_0$

$$E_a(UO_2) \approx 0.23 \text{ eV}$$

Holstein proposed $\gamma = 10$ as the typical electron-phonon coupling constant for small-polaron crystals.

The activation energy calculated here $E_a = 0.23 \text{ eV}$ is well in the range of the activation energy deduced from the experiments. However, the agreement between theory and experiment might be fortuitous for at least three reasons.

1. One of the basic expressions involved in small polaron theory γ_k is especially adapted in the long wavelength part of the Brillouin zone and is less accurate for small wavelengths.
2. The experimental values for ϵ_0 , ϵ_∞ and ω_0 correspond to crystals of which the stoichiometry presumably was different.
3. The small polaron theories treat the case of crystals with an optical longitudinal dispersion branch. In this respect they are not applicable to UO_2 with its CaF_2 structure. However, in general the optical longitudinal modes with the highest frequency contribute predominantly to the polarization.

In Holstein's treatment the activated mobility behaviour is expected for $kT \gg \frac{\hbar\omega}{2}$. At $kT \ll \frac{\hbar\omega}{2}$ a totally different mechanism (polaron band conduction) with a drift mobility which sharply decreases with increase of temperature is expected. In the three-dimensional treatment of Lang and Firsov the transition temperature is shifted towards lower temperatures. The most stringent criterion (for the existence of hopping type motion) is $kT > \frac{\hbar\omega}{4}$. However, the conductivity results show that the hopping type motion dominates still at much lower temperatures. At the lowest temperatures covered, the activation energy for the electrical conductivity changes but no polaron band conduction is observed.

7. ATOMIC MOTION PHENOMENA

7.1. Uranium self-diffusion in UO_2

7.1.1. Introduction

Experiments on the self-diffusion of uranium in sintered uranium dioxide have been performed by AUSKERN and BELLE [34], by LINDNER and SCHMITZ [35] and by ALCOCK and McNAMARA [36]. The results are summarized in Fig. 45. Although all the experiments deal with sintered materials using the surface activity decrease method, it is clear that the values of the diffusion coefficient D measured by these different authors differ widely. It seemed therefore worthwhile to carry out U self-diffusion experiments on single crystals as a function of composition. In the study reported here, self-diffusion of uranium has been measured at temperatures between 1300 and 1800°C using the sectioning technique.

7.1.2. Experimental procedures and results

Diffusion couples are designed to approximate a semi-infinite couple with an instantaneous source of diffusion material, initially concentrated on a plane. A couple is prepared by cutting a disc, 4 mm in diameter and 1 mm thick, from a single crystal of nearly stoichiometric natural UO_2 . One face of the couple is polished to a flatness better than 0.1 micron over the whole surface, and a layer of

$^{235}\text{UO}_2$ is then vapour deposited to a thickness of max. 0.2 micron. Evaporation of the tracer during the diffusion anneals is avoided as follows. Two crystals are mounted in a close fitting hole drilled in a sintered UO_2 pellet, the labelled surfaces separated by a thin single crystalline ring, 100 micron thick. Diffusion anneals at temperatures higher than 1600°C are very difficult due to strong deformation of the labelled surfaces. It is necessary to use very perfect crystals which show no traces of subgrains or imperfections after a long annealing.

The samples are diffusion annealed at a pressure of 10^{-5} mm Hg in a molybdenum wound alumina furnace, controlled to $\pm 5^\circ\text{C}$. After annealing, the couple is mounted on a precision grinder especially developed for this study [37]. This allows the adjustment of the original surface up to a precision of 0.02 micron, and removes parallel layers of 0.08 micron, the material of the layers being collected for analysis.

In each sample the ratio ^{235}U is determined. The ^{235}U concentration is measured by neutron irradiation and subsequent counting of the $^{140}\text{(Ba-La)}$ peak in a multi-channel spectrometer. The total amount of ($^{235}\text{U} + ^{238}\text{U}$) is measured by fluorimetric analysis. Several standards have been checked by mass spectrometry. From this it follows that the largest error of the method could be estimated to be about 10 %, mainly due to fluorimetry. The thickness of each layer is calculated from the total amount of U to a precision of ± 0.01 micron.

The expression relating the diffusion coefficient to the concentration C versus penetration profiles x is well known

$$\frac{C}{C_0} = \frac{1}{\sqrt{\pi Dt}} \exp\left(-\frac{x^2}{4Dt}\right)$$

The results of four vacuum anneals at 1300, 1450, 1465 and 1800°C are summarized in Table V.

TABLE V

Temperature ($^\circ\text{C}$)	Diffusion coefficient ($\text{cm}^2 \text{s}^{-1}$)
1300	3.3×10^{-16}
1450	2.2×10^{-15}
1465	3.6×10^{-15}
1800	3.2×10^{-13}

These results are also plotted as a log D versus $1/T$ together with the results reported by Auskern and Belle, Lindner et al. and Alcock et al. (Fig. 43).

7.1.3. Discussion

As mentioned before, the experimental results on uranium ion self-diffusion coefficients obtained by three different authors on sintered UO_2 differ. Auskern and Belle measured the diffusion of ^{235}U in high density UO_2 , held in an atmosphere of flowing hydrogen, and found $D = 4.3 \times 10^{-4} \exp(-88,000/RT)$ from 1450 to 1850°C. Higher values were reported by Lindner and by Alcock et al.; they found respectively $D = 0.23 \exp(-104,600/RT)$ and $D = 118 \exp(-108,000/RT)$. Our values of the diffusion coefficient measured on well reduced single crystalline UO_2 seem to agree well with the values obtained by Auskern and Belle. A least square analysis of our data leads to an activation energy of 88 ± 6 kcal mole⁻¹.

The reasons for the discrepancy between the values for the activation energy and especially for D_0 are not fully understood. The large difference in the D values may possibly be due to different experimental conditions employed by the various investigators. Lindner et al. did not use a combined diffusion couple in their experiments. As pointed out by Auskern and Belle, this may have lead to evaporation losses and as a consequence to apparent higher values of the diffusion coefficients. Alcock et al. measured also the diffusion coefficient in two single crystal specimens at one temperature (1600°C) and found much less U penetration, D being 1×10^{-15} cm² s⁻¹ (our corresponding value at this temperature would be about 25 times higher). The concordance of our first results on single crystals and those obtained by Auskern and Belle seems to indicate that the grain boundaries do not influence significantly the cation diffusion. This should then be in accordance with several investigations on cation diffusion in different oxides and halides mentioned in the literature [38] [39].

7.2. Migration energies for uranium and oxygen point defects

7.2.1. Introduction

For a complete understanding of the self-diffusion process, the activation energies for migration of the diffusion current carriers have to be known. Therefore, methods have been utilized to create excess concentration of point defects. The techniques employed in this investigation include quenching and irradiation with thermal neutrons. Electrical conductivity is used to determine the point defect concentrations. Variations of these concentrations as a result of annealing give information about the energies of migration.

7.2.2. Migration energy of oxygen interstitials in UO_{2+x}

a) Introduction

As reported earlier [40] the conductivity curves of quenched as-grown crystals ($O/U \approx 2.005$) show some kind of irreversible hysteresis during a first

temperature cycle in the region 20–200°C ; the heating and cooling curves do not coincide. The room temperature conductivity after cooling is decreased by about a factor of 2 as compared to the initial one. The excess oxygen content $(O/U \approx 2.005)$ of the UO_2 specimens used in these measurements exceeds the oxygen solubility limit at room temperature.

If a slightly oxidized UO_2 crystal is sufficiently rapidly quenched from a temperature above the phase boundary then the excess oxygens can be nearly completely retained in the UO_{2+x} phase. U_4O_9 precipitates can also be partly dissolved by irradiation with high energetic particles. If one heats now subsequently these quenched or irradiated samples one will attain a temperature at which the oxygen interstitials become mobile and will migrate through the lattice until they reach a U_4O_9 precipitate. The U_4O_9 precipitates will act as sinks for the oxygen interstitials whose disappearance out of the UO_{2+x} phase will influence the electrical conductivity. The present study is based on the recovery of the electrical resistivity during annealing experiments.

b) Experimental

The four probe method of VAN DER PAUW [11], which requires plane-parallel platelets of arbitrary shape with four point contacts at the periphery has been used to determine the electrical conductivity. The UO_2 single crystals (composition in the range $UO_{2.005}$ to $UO_{2.05}$) used in this investigation are first shaped to a four-leaf clover of approximately $5 \times 5 \times 0.5$ mm. On one side of the specimens four Au contacts with Pt strips are alloyed by heating in a high frequency furnace. Quenching was achieved by heating the crystals in an inert atmosphere (Ar 10^{-3} mmHg) to around 800°C and cooling in liquid nitrogen.

c) Results and discussion

In order to investigate the effect of thermal treatment, a quenched UO_2 crystal ($O/U \approx 2.005$) was submitted to isochronal pulse annealing in the temperature range 20–200°C. Pulses of 30 min at about 10°C interval are applied with intermediate determinations of the conductivity at room temperature (21.0°C). The

results presented as $\frac{\sigma^2 - \sigma_\infty^2}{\sigma_0^2 - \sigma_\infty^2}$ versus the pulse temperature are given in Fig.45.

Here σ_0 , σ and σ_∞ are the conductivity values after quenching, after each annealing step and after complete annealing, respectively. In this case, squared values of σ are used as a measure of the defect concentration since it is assumed that UO_2 is still in the extrinsic range at the reference temperature. In this range the number of free holes is proportional to the square root of the acceptor concentration. No significant change in the electrical conductivity values is observed below the pulse temperature of 100°C. Above this temperature the defect concentration starts varying as observed by the decrease in the electrical conductivity, and reaches a constant value at about 180°C.

In another experiment a quenched UO_{2+x} crystal was heated with a constant rate and subsequently cooled down to room temperature. Readings of the resistivity were made every five minutes. Fig. 47, which shows the results, is representative for the annealing process taking place between 20 and 230°C. The upper line represents the heating curve. One sees again that deviation from the linear behaviour starts around 100°C.

There are a number of experimental approaches to study the annealing processes and, in particular, to determine the activation energy involved in the process. In this study the technique of OVERHAUSER [41] has been used to determine the migration energy of the oxygen interstitial in UO_{2+x} . This method is based on the measurement of two successive isothermal anneals at two different temperatures. By comparing the rate of recovery at the end of the first isothermal and the rate of recovery at the beginning of the second isothermal, the activation energy can be determined.

In a first experiment two successive isothermals were measured on a quenched crystal ($O/U \approx 2.13$) at the temperatures 141.8°C and 161.1°C. The electrical resistivity was measured every minute at the annealing temperature. After 50 min the annealing temperature was abruptly changed to the higher temperature. The results are shown in Fig. 48. The activation energy of migration E_M of the oxygen interstitial calculated from these data, using the equation

$$\ln \frac{\left(\frac{dc}{dt}\right)_{T_1}}{\left(\frac{dc}{dt}\right)_{T_2}} = -\frac{E_M}{k} \left(\frac{1}{T_1} - \frac{1}{T_2}\right)$$

is found to be 0.88 ± 0.05 eV.

In a second experiment the same measurements were repeated on a quenched $UO_{2.003}$ crystal at different temperatures ($T_1 = 133.3^\circ\text{C}$ and $T_2 = 155.8^\circ\text{C}$) and on a slightly different way. Pulses of 30 min were applied and the electrical conductivity was measured after cooling to a reference temperature (23.8°C). Moreover, at the same time the changes in conductivity were determined every minute at the pulse temperature. The differences in conductivity measured at the pulse temperature and at the reference temperature were in good agreement. The analysis of this second experiment yields an activation energy $E_M = 0.82 \pm 0.05$ eV.

From the experiments it follows that the oxygen interstitial is mobile in the UO_{2+x} lattice at temperatures as low as 100°C. Its migration energy is equal to 0.85 ± 0.1 eV.

7.2.3. Migration energy of uranium

a) Introduction

The electrical conductivity of slightly oxidized UO_2 crystals drops markedly as a result of fission fragment damage [42]. This decrease in electrical

conductivity shows that during irradiation defect centres are produced which reduce the initial free hole concentration. Changes in electrical conductivity when annealing is applied subsequent to neutron irradiation may, therefore, give information about the activation energies for point defect migration in UO_2 .

b) Experimental procedures and results

As in the previous study, the electrical conductivity before and after irradiation has been determined by using Van der Pauw's method. The irradiations were carried out in the BRI reactor at reactor temperature (about 90°C). However, due to γ - and nuclear heating during exposure, the temperature of the specimens may exceed 90°C . After exposure, the crystals are sandblasted and etched in order to remove a thin oxide layer formed by oxidation on the surface during irradiation.

The electrical conductivity of as-grown UO_2 crystals ($O/U \approx 2.005$), measured after successive periods of reactor exposure, drops markedly as a result of fission fragment damage and reaches a constant value at about 4×10^{15} thermal neutrons cm^{-2} (or 4×10^{15} fissions cm^{-3}). At this dose the total crystal volume is affected by the fission tracks and a saturation of damage is achieved. The total decrease in electrical conductivity after exposure up to the saturation dose corresponds to about three decades (initial value $\sigma \approx 10^{-3} \text{ ohm}^{-1}\text{cm}^{-1}$ at 300°K).

Two UO_2 single crystals, irradiated to an integrated thermal neutron flux of about $5 \times 10^{15} \text{ n cm}^{-2}$, were submitted to isochronal pulse annealing experiments (pulses of 1 h) in the temperature range 100 – 850°C . Before measurement of the residual conductivity at the reference temperature (22°C), the crystal surfaces were carefully etched and sandblasted. The results of these annealing experiments are shown in Fig. 49. Two distinct annealing stages are observed. Between 350°C and 500°C a further decrease in the conductivity occurs, whereas recovery only starts at 650°C with an annealing peak around 725°C . Until now only the recovery stage occurring at high temperature is examined in further detail. For this purpose, a new series of annealing measurements was conducted in such a way that a constant heating rate (temperature difference/time difference = 1°C min^{-1}) is achieved. In the temperature range between 670° and 850°C about every 30°C a pulse of required time is applied with intermediate determinations of the conductivity at room temperature. As will be discussed, such pulse annealing curves can be analyzed using the method of BALARIN and ZETZSCHE [43] [44] and permit us to determine the activation energy of defect migration.

c) Discussion

The irradiations result in a marked decrease of the electrical conductivity, indicating that defect centres, which act as hole traps, are produced. So the problem which we are dealing with is to determine the nature of the hole traps and their activation energy for motion. The pulse annealing data show a recovery stage and thus a disappearance of the hole traps in the temperature range 670 – 850°C .

The annealing data performed under the special experimental conditions (heating with a constant rate) are analyzed according to Balarin and Zetzsch's method. Starting from the known kinetic equations for concentration decrease, these authors showed that the function $\ln(\ln \frac{C_0}{C})$ or the function $\ln(\frac{C_0}{C} - 1)$ depends linearly on the reverse absolute temperature if one has a process of first or second order, respectively ($\frac{C}{C_0}$ represents the relative concentration of the defects). For both processes, the activation energy can be calculated from the slope of the straight line thus obtained.

In Fig. 50 both functions $\log(\ln \frac{\sigma_\infty - \sigma_0}{\sigma_\infty - \sigma})$ and $\log(\frac{\sigma_\infty - \sigma_0}{\sigma_\infty - \sigma} - 1)$ are plotted versus $\frac{1}{T}$ (the ratio $\frac{\sigma_\infty - \sigma_0}{\sigma_\infty - \sigma}$ is considered to be proportional to $\frac{C_0}{C}$). As one can notice, a linear behaviour appears if the function $\log(\frac{\sigma_\infty - \sigma_0}{\sigma_\infty - \sigma} - 1)$ is used, pointing to second order kinetics for the annealing stage at the 725°C peak. The activation energy for defect migration calculated from the slope of this line curve is found to be equal to 2.3 ± 0.3 eV. Information about the nature of the point defect annealed during this stage can be obtained if one compares the energy for uranium and oxygen self-diffusion. The values for uranium self-diffusion energy are in the range 3.8 - 4.7 eV [34] [35] [45]; the activation energy for oxygen self-diffusion is smaller and equal to about 1.3 eV for a UO_{2+x} composition here employed [46]. One can conclude that the most evident explanation for the 2.3 eV process is uranium point defect migration. A further argument, which proves definitely this assumption, is that the oxygen interstitial is mobile at much lower temperatures (about 100°C) (see quenching experiments), so that all oxygen point defects produced by irradiation will have been annihilated at the temperature where the annealing of the hole trapping centres starts. The second order kinetics found here is consistent with the annealing picture of the migration of a more mobile U point defect to a nearly immobile one. Thus, one is inclined to accept the annihilation of the U vacancies and interstitials by recombination. Belle et al. assumed that the cation diffusion is accomplished by the movement of a uranium ion into a vacant lattice site. The diffusion in stoichiometric UO_2 is then controlled by the formation of Frenkel-type defects in the cation sublattice. If these assumptions are valid, the activation energy for uranium self-diffusion has to be decomposed into two parts: the energy required to create a Frenkel pair and the energy required for migration. The energy of motion (2.3 eV) of the uranium point defect represents about 60% of the value of the self-diffusion energy (3.8 eV) reported here. This is rather high since in general the energy of migration is smaller than the energy required to create the defect. Therefore, it would appear that the annealing process could be more complex than the simple model described by the migration of a single point defect.

Concluding, the recovery of the electrical conductivity due to the annihilation of U point defects leads to the supposition that the defect centres which act as hole traps are U vacancies.

In the annealing experiments after neutron irradiation, a reverse annealing stage is encountered between 350° and 500°C. This annealing stage will not be discussed here, since no detailed measurements, which might clarify the nature of this process, have been made until now.

7.3. Reorientation of oxygen interstitials

Internal friction experiments with small single crystal specimens vibrated in transverse resonance have revealed the existence of a relaxation process. For frequencies in the range 500-1000 Hz, the damping spectrum exhibits one or more maxima in the temperature region between room temperature and -50°C.

For a simple relaxation process, the maximum damping is determined by the condition

$$\omega\tau = 1$$

if $\omega = 2\pi f$ is the angular frequency of oscillation and τ the relaxation time. Very often τ depends on the temperature according to an Arrhenius type of relation

$$\tau = \tau_0 \exp \left[\frac{H}{kT} \right]$$

with $\tau_0^{-1} = Z\alpha \nu_0 \exp \left[\frac{\Delta S}{k} \right]$

and Z , coordination number, α a geometrical factor of order 1, ν_0 the jump frequency of the relaxing species, $\Delta F = H - T\Delta S$ the free energy of relaxation; k and T have their usual significance.

There exist several possibilities for obtaining the value of τ_0 and H for a relaxation process. The best way of course is to measure the peak temperature T_m at different frequencies and to plot $\ln \tau (= \ln \frac{1}{\omega})$ as a function of $1/T_m$. However, for the problem at hand this has proved to be impracticable due to the complex nature of the relaxation effect and to the limited frequency range which could be covered. One can obtain a reasonable estimate of the activation energy by using the fact that for an atomistic relaxation process the value of τ_0 does not vary very much and is of the order of $10^{-14} - 10^{-15}$ s. Thus, for one measurement of the peak temperature at one frequency, one can calculate the value of H . This procedure yields, for the relaxation effect discussed here, an activation energy of approximately 0.4 - 0.5 eV. This is higher than the value obtained for the thermal activation of the electrical conductivity, and lower than the energy of migration of interstitial oxygen atoms or of uranium atoms in the UO_2 lattice. Since the peak heights vary with heat treatment, the relaxation process must involve some kind of intrinsic defect. From the neutron diffraction data of WILLIS [47] the structure of the oxygen interstitial in lightly oxidized UO_2 (Fig. 5!) has been proposed. The average lattice strain per mole fraction of defects, caused by this defect can be described by a diagonal λ tensor with eigen vectors λ_1 , λ_2 and λ_3 lying along $\langle 113 \rangle$, $\langle 110 \rangle$ and $\langle 332 \rangle$. It can be seen from the model in Fig. 5!, that the orientation of the defect is characterized by the orientation of the $\langle 113 \rangle$ principal

strain. Since there are twelve $\langle 113 \rangle$ directions, the defect can occupy anyone of twelve equivalent positions in the unstressed lattice. Upon application of a stress, the number of equivalent sites will decrease and the defects will redistribute themselves according to the difference in potential energy between sites. This redistribution causes a non-elastic strain, resulting in a relaxation peak if the damping is measured as a function of temperature.

NOWICK and HELLER [48] have developed a general treatment for deriving the relaxation strengths caused by a stress-induced reorientation of elastic dipoles. This method has been applied for the case of a hypothetical defect having a λ tensor corresponding with the model for the oxygen interstitial in UO_2 . For any particular stress direction, we can now calculate the concentration of defects in anyone of the twelve possible directions. From these concentrations, we obtain at once the relaxation strength and, if we know the jump frequencies connecting the different orientations, we can calculate the relaxation times. We still outline the procedure for a stress in the $[100]$ direction, and then simply state the results for two other special cases, i.e. for stresses in the $[110]$ and $[111]$ directions.

$\langle 113 \rangle$ defect under a $[100]$ stress

We will number the twelve $\langle 113 \rangle$ directions. The principal axes corresponding with each site are collected in Table VI.

TABLE VI

Site number p	Principal axes		
1	$\bar{3}1\bar{1}$	$01\bar{1}$	$\bar{2}\bar{3}\bar{3}$
2	$3\bar{1}\bar{1}$	011	$\bar{2}3\bar{3}$
3	$\bar{3}11$	$01\bar{1}$	$23\bar{3}$
4	$31\bar{1}$	011	$2\bar{3}\bar{3}$
5	$\bar{1}31$	101	$3\bar{2}\bar{3}$
6	131	$10\bar{1}$	$\bar{3}2\bar{3}$
7	$1\bar{3}\bar{1}$	101	$\bar{3}23$
8	$\bar{1}\bar{3}1$	$10\bar{1}$	$32\bar{3}$
9	$\bar{1}\bar{1}\bar{3}$	110	$\bar{3}\bar{3}\bar{2}$
10	$11\bar{3}$	$1\bar{1}0$	$\bar{3}\bar{3}2$
11	$\bar{1}1\bar{3}$	$1\bar{1}0$	$\bar{3}3\bar{2}$
12	$11\bar{3}$	$1\bar{1}0$	$33\bar{2}$

The occupation C_p of the different sites is given by

$$C_p = \frac{C_o}{n} = \frac{V C_o \sigma}{nkT} \left(\lambda^p - \frac{1}{n} \sum_{q=1}^n \lambda^q \right)$$

where : C_0 is the molar concentration of defects ;
 n the number of possible orientations of the defect ;
 V_0 the volume per atom of the crystal ;
 σ the external stress ;
and kT have their usual significance.

Further $\lambda^p = \sum_{i=1}^3 (\alpha_i^p)^2 \lambda_i$ is the component of the λ tensor along the stress axis (α_i^p are direction cosines between the stress and the principal axes). For a stress σ along [100], the twelve equivalent directions separate into two groups, group I of four elements (sites 1 - 4) and group II of eight elements (sites 5 - 12). The corresponding direction cosines are

	α_1^p	α_2^p	α_3^p
group I	$3/\sqrt{11}$	0	$2/\sqrt{22}$
group II	$1/\sqrt{11}$	1/2	$3/\sqrt{22}$

and hence $\lambda_I^p = \frac{9}{11} \lambda_1 + \frac{2}{11} \lambda_3$

$$\lambda_{II}^p = \frac{1}{11} \lambda_1 + \frac{9}{2} \lambda_2 + \frac{9}{22} \lambda_3$$

This yields for the occupation numbers after complete relaxation

$$C_I = \frac{C_0}{12} + \frac{V_0 C_0 \sigma}{12 kT} \cdot \frac{1}{3} \cdot \left(\frac{16}{11} \lambda_1 - \lambda_2 - \frac{5}{11} \lambda_3 \right)$$

$$C_{II} = \frac{C_0}{12} + \frac{V_0 C_0 \sigma}{12 kT} \cdot \frac{1}{3} \cdot \left(-\frac{8}{11} \lambda_1 + \frac{1}{2} \lambda_2 + \frac{5}{22} \lambda_3 \right)$$

The relaxation strength δJ is given by

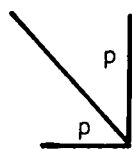
$$\delta J = \frac{1}{\sigma} \sum_{p=1}^n \lambda^p \left(C_p - \frac{C_0}{n} \right)$$

This gives for a [100] stress

$$\delta J_{100} = \frac{2}{363} \frac{V_0 C_0}{12 kT} (16 \lambda_1 - 11 \lambda_2 - 5 \lambda_3)^2$$

One may go on now and calculate the relaxation time. For this, we need the jump frequencies between the twelve orientations of the defect. These have been tabulated in Table VII. It is clear by reference to Fig. 51 that one can distinguish three different jump frequencies.

TABLE VII



	1	2	3	4	5	6	7	8	9	10	11	12
1	0	v_2	v_1	v_2	v_3	v_3	v_3	v_3	v_3	v_3	v_3	v_3
2		0	v_2	v_1	v_3	v_3	v_3	v_3	v_3	v_3	v_3	v_3
3			0	v_2	v_3	v_3	v_3	v_3	v_3	v_3	v_3	v_3
4				0	v_3	v_3	v_3	v_3	v_3	v_3	v_3	v_3
5					0	v_2	v_1	v_2	v_3	v_3	v_3	v_3
6						0	v_2	v_1	v_3	v_3	v_3	v_3
7							0	v_2	v_3	v_3	v_3	v_3
8								0	v_3	v_3	v_3	v_3
9									0	v_2	v_1	v_2
10										0	v_2	v_1
11											0	v_2
12												0

For a [100] stress, one obtains the following rate equations for the concentrations n_I and n_{II} (we will neglect the small change in jump frequency due to the stress)

$$\dot{n}_{II} = -4 v_3 n_{II} + 4 v_3 n_I$$

$$4 n_I + 8 n_{II} = C_0$$

The relaxation time is therefore in this case

$$\tau_{100}^{-1} = 12 v_3$$

The time dependence of the concentrations n_I and n_{II} can then be written as

$$n_I = A_I e^{-t/\tau_{100}} + B_I$$

$$n_{II} = A_{II} e^{-t/\tau_{100}} + B_{II}$$

The constants A and B are determined by the boundary conditions (e.g. : at $t=0$, $n_I = n_{II} = \frac{C_0}{12}$; at $t=\infty$, $n_I = C_I$; $n_{II} = C_{II}$). If more than one relaxation time is required to describe the time dependence of the occupation numbers of the different orientations, the values of the constants A can be used instead of C_p in the expression given the total relaxation strength caused by the stress induced rotation of the defects. In the way, the weight of the different relaxation processes can be determined separately.

These calculations have been carried out not only for a stress along a [100] direction, but also for a stress along a [111] direction and along a [110] direction. The results are listed in Table VIII.

TABLE VIII

Stress	Relaxation time	Relaxation strength
[100]	$12 \nu_3$	$\frac{2}{363} \cdot \frac{V_0 C_0}{12kT} \cdot (16 \lambda_1 - 11 \lambda_2 - 5 \lambda_3)^2$
[111]	$4 (\nu_2 + 2 \nu_3)$	$\frac{4}{363} \cdot \frac{V_0 C_0}{12kT} \cdot (2 \lambda_1 - 11 \lambda_2 + 9 \lambda_3)^2$
	$2 (\nu_1 + \nu_2 + 4 \nu_3)$	$\frac{288}{363} \cdot \frac{V_0 C_0}{12kT} \cdot (\lambda_1 - \lambda_3)^2$
[110]	$2 (\nu_1 + \nu_2 + 4 \nu_3)$	$\frac{216}{363} \cdot \frac{V_0 C_0}{12kT} \cdot (\lambda_1 - \lambda_3)^2$
	$4 (\nu_2 + 2 \nu_3)$	$\frac{3}{363} \cdot \frac{V_0 C_0}{12kT} \cdot (2 \lambda_1 - 11 \lambda_2 + 9 \lambda_3)^2$
	$12 \nu_3$	$\frac{1}{363} \cdot \frac{1}{2} \cdot \frac{V_0 C_0}{12kT} \cdot (16 \lambda_1 - 11 \lambda_2 + 9 \lambda_3)^2$

As can be seen in Table VIII, one expects one relaxation time for a stress in a [100] direction, two times for a stress along a [111] direction, and three times for a stress along [110]. The total relaxation strength for the three cases is difficult to compare a priori without a knowledge of λ_1 , λ_2 and λ_3 . In fact, measurements of the orientation dependence of the relaxation strength can be used to obtain the relative magnitudes of λ_1 , λ_2 and λ_3 .

In order to check this model, one should investigate therefore a specimen oscillating in such a way that the stress is in a [100], a [110] or a [111] direction. Such experiments are in progress; no definite conclusion can be drawn before they are finished.

8. KUCZYNSKI-TYPE SINTERING

In this type of experiments the sintering is observed between single crystal spheres held in mutual contact.

The optical measurement of the diameter of the "necks" formed between the spheres, or between the spheres and a plate, as a function of time, temperature and composition allow us to discern possible sintering mechanisms and to study some important sintering parameters.

The main difficulty encountered in these experiments is the temperature stabilization. A furnace suitable for long operation at temperatures of about 1700°C with the possibility of applying a controlled oxygen atmosphere has been constructed.

The first results seem to point to a neck growth proportional to the square root of time (Fig. 52). According to the theoretical calculation of Kuczynski, this would be due to viscous or plastic flow. Insufficient number of experiments, however, were carried out (sintering for 3, 7 and 16 h) to draw a definite conclusion. Fig. 53 and 54 show necks between two spheres sintered at 1700°C for 3 and 7 h.

Some sintering experiments were carried out in controlled oxygen atmosphere. Although quantitative data cannot be given, it was observed that in this atmosphere sintering was much faster.

9. MAGNETIC SUSCEPTIBILITY

The magnetic susceptibility of UO_{2+x} single crystals with $0 < x < 0.25$ has been measured between 7 and 11 kOe at temperatures ranging from 90° to 300°K. The samples were obtained by oxidizing $UO_{2.00}$ single crystals.

As stated before [49], the measured values of the susceptibility χ_m depend on the magnetic field strength H , indicating the presence of parasitic ferromagnetism. The largest difference between the values of χ_m at a given temperature was about 6 %, a relatively small percentage. However, the inaccuracy in the real value of the susceptibility χ obtained by extrapolation is too large to predict:

1. the paramagnetism of the UO_{2+x} samples is due to spins only ;
2. the more oxidized ions in UO_{2+x} with $x < 0.25$ are either in a 5+ or 6+ state.

The susceptibility of a $UO_{2.056}$ sample, irradiated to a dose of 3.3×10^{17} neutrons cm^{-2} , was about 4 to 10 % lower than that of an unirradiated reference crystal. WEIL and COHEN [50] reported an increase of a few per cent after irradiation. However, their UO_2 samples were polycrystalline and were submitted to a much lower neutron dose (8.6×10^{15} n cm^{-2}). The decrease in our crystal seems to be mostly due to the reduction of the ferromagnetic component of the susceptibility. This ferromagnetic contribution saturates between 8 and 11 kOe. Even with the application of these fields it cannot be determined accurately as it is only a small fraction of χ .

The magnetic moment per uranium ion for bulk $UO_{2.00}$ reported by ARROTT and GOLDMAN [51] is within 3.07 to 3.20 μ (μ = Bohr magneton). When UO_2 is diluted

with ThO_2 in solid solution a moment of 2.83μ is found [52]. This difference in moments found by the same measuring technique gives no evidence for the presence of ferromagnetic impurities. It seems difficult to accept that such impurities should be present only in UO_2 and not in ThO_2 .

In the next paragraphs our results will be discussed.

Six crystals, designated by the letters from A to F, were measured. The O/U ratio of these samples is equal to 2.00, 2.00, 2.056, 2.056, 2.15 and 2.22 respectively. The reciprocal of the susceptibility has been plotted versus the absolute temperature T for each of these specimens. This is shown in Fig. 55 for sample A. The data obey the Curie-Weiss (C.W.) law :

$$\frac{1}{\chi} = \frac{T - \theta}{C} \quad (1)$$

where θ is the Weiss constant which is obtained by extrapolating the straight line in the $1/\chi$, T diagram to $1/\chi = 0$. With the aid of this value the Curie constant C can be obtained. The values of θ and C for different samples are plotted versus x in Fig. 57 and 58. From our experimental results one θ and one C can be deduced for every specimen except for F. For this sample with composition O/U = 2.22, the experimental points do not fall on a single straight line, as shown in Fig. 56. When measuring only either in the lower or in the higher temperature range one would have found two different straight lines, leading to two different values of θ . This means that within the limits of precision of the measurements the C.W. law is found to hold in a restricted temperature range. If one considers the whole temperature range a line with $\theta = -100^\circ$ can be chosen so that the value at any temperature approaches the corresponding χ to better than 2%. Although this difference is small, it is the systematic deviation that forces us to conclude that the C.W. law is not obeyed in this case. GATOO et al [53] found that their χ values can be represented by the equation

$$\chi = \frac{C}{T - \theta} + B \quad (2)$$

Here, B is a temperature independent term. We calculated the constants of this equation using our χ values, obtained at three different temperatures. For sample F a double analysis has been made on two different series of experimental points. The values obtained in both cases are :

1. $\theta = -38.5^\circ$	$B = 707 \times 10^{-6} \text{ mole}^{-1}$	$C = 0.434 \text{ mole}^{-1}$
2. $\theta = -77.6^\circ$	$B = 238 \times 10^{-6} \text{ mole}^{-1}$	$C = 0.663 \text{ mole}^{-1}$

The appreciable differences are an indication that the analysis is very sensitive to minor deviations from the real susceptibilities due to errors in the measurements. In order to check this we added a variable fraction to the χ values in the formula (2). The fractions were chosen so that $+\frac{\Delta_{T_1}}{T_1} = -\frac{\Delta_{T_2}}{T_2} = +\frac{\Delta_{T_3}}{T_3}$. The subscripts indicate the temperature at which the respective χ 's were measured.

Changing this relative error from + 1 to - 1 % causes the calculated B values to change from $+ 715 \times 10^{-6} \text{ mole}^{-1}$ to $- 583 \times 10^{-6} \text{ mole}^{-1}$, while C varies from 0.426 to 0.850 mole^{-1} . The θ values went from - 24.8 to - 170°.

Using equations (1) and (2) one can deduce values for θ , B and C which are very close to those given by Gotoo et al. All these different mathematical approaches therefore describe the same physical situation.

In the next paragraph a physical model supporting the former equations will be presented.

The mean magnetic moment in the x direction $\langle \mu_x \rangle$ of a free ion is related to the temperature and the field strength by the Brillouin function [54]

$$\langle \mu_x \rangle = \mu B_j(z) \quad (3)$$

Here μ is the maximum value of the ion in the x direction and

$$B_j(z) = \left[\left(1 + \frac{1}{2j} \right) \coth \left(1 + \frac{1}{2j} \right) z - \frac{1}{2j} \coth \frac{1}{2j} z \right] \quad (4)$$

wherein the Langevin variable is given by

$$z = \frac{\mu H}{kT} \quad (5)$$

In magnetic materials the ions are no more free but interact mutually. The result of this interaction is expressed in the formulation as an effective field added to the external one.

Therefore, the Langevin variable becomes

$$z = \frac{\mu_i}{kT} \left[H + \sum_{j=1}^{j=N} w_{ij} \mu_j \right] \quad (6)$$

Here, μ_j is the moment of the ion in the neighbourhood of the considered one which is labelled i and w_{ij} is a proportionality constant relating the effect of the j-th ion on the i-th one to an effective field. The summation must be carried out over all ions influencing the i-th one.

When z is small, one has in a good approximation

$$B_j(z) = \frac{z}{3} \left(1 + \frac{1}{j} \right) = \frac{cst}{T} \times H \quad (7)$$

For antiferromagnetic and ferrimagnetic materials above the Néel temperature, the mean moment per ion is less than that of the free ion. The mutual interactions tend to put the moments antiparallel. In a crystal built up by two magnetic sublattices, Néel described the phenomenon by a mutual interaction between the sublattices.

In analogy with equation (3) and in the region where equation (7) holds one has

$$M = \sum_{i=1}^{i=l} M_i = \sum_{i=1}^{i=l} \frac{C_i}{T} H + \sum_{j=1}^{j=l} W_{ij} M_j \quad (8)$$

Here, M is the mean magnetic moment of the sample ;

M_i is the mean magnetic moment of the sublattices ;

W_{ij} is a proportionality constant expressing the effect of M_j on M_i ;

and C_i is the Curie constant for the sublattice.

Eq. (8) gives

$$\lambda = \frac{C}{T - \theta} + D \quad (9)$$

$$\text{where } C = C_1 + C_2 \quad (10)$$

$$\theta = C_1 W_{11} + C_2 W_{21} \quad (11)$$

$$\text{and } D = D_0 (C_2 W_{22} + C_1 W_{12}) - (C_1 W_{11} + C_2 W_{21}) \quad (12)$$

In the case that the two sublattices are identical i.e. when $(C_2 W_{22} + C_1 W_{12}) = (C_1 W_{11} + C_2 W_{21})$ the value of D vanishes and eq. (9) equals eq. (1). In UO_2 such a situation is present. In this material there is only one kind of magnetic ions, i.e. the U^{4+} ion. The ions are situated on two sublattices, both identical. Therefore, $C_1 = C_2$, $W_{22} = W_{11}$ and $W_{21} = W_{12}$. Eq. (1) is found to be in good agreement with the experiment (Fig. 55). In U_4O_9 the two sublattices can be different, independent of the fact that the formula can be written as $(UO_2)_2U_2O_5$ or as $(UO_2)_3UO_3$. Here D appears in the formula. This is in agreement with the experimental results. It has been tried to calculate the D value taking into account the deviation of the λ values from a Curie-Weiss law. It was already mentioned that this deviation is small, so it becomes difficult to obtain an accurate value for D . Moreover, it is impossible to determine its temperature dependence and to compare it with the theoretical prediction. This is the reason why eq. (9) practically equals eq. (1).

Concluding, the temperature behaviour of the magnetic susceptibility of UO_{2+x} supports Néel's model for antiferromagnetic and ferrimagnetic materials showing two magnetic sublattices. The measurements, however, are not precise enough to determine the valency state of the more oxidized uranium ions. One of the major causes of the uncertainties on the λ values seems to be a parasitic ferromagnetism. An accurate value of λ could be obtained by using extremely pure material (purity better than 99.999 %).

REFERENCES

- [1] A. CHAPMAN and R. MEADOWS, ORNL-2587
- [2] J. AMBLER and G. SLATTERY, J. Nucl. Mat. 4, 90 (1961)
- [3] H. KIRKPATRICK and S. AMELINCKX, Rev. Sci. Instr. 33, 488 (1962)
- [4] H. BLANK and S. AMELINCKX, Z. Metallk. 55, 460 (1964)
- [5] H. HASHIMOTO, A. HOWIE and M. WHELAN, Phil. Mag. 5, 957 (1960)
- [6] R. NELSON, AERE-R.4564
- [7] J. MACKENZIE, J. Phys. Chem. Solids 23, 185 (1962)
- [8] O. BETHOUX, P. THOMAS and L. WEIL, Compt. Rend. 253, 2043 (1961)
- [9] M. HOLLAND and C. RUBIN, Rev. Scient. Instr. 33, 923 (1962)
- [10] W. JONES, J. GORDON and E. LONG, J. Chem. Phys. 20, 695 (1952)
- [11] L. VAN DER PAUW, Philips Res. Rept. 13, 1 (1958)
- [12] H. JURETSCHKE, R. LANDAUER and J. SWANSON, J. Appl. Phys. 27, 338 (1955)
- [13] L. FRIEDMAN and T. HOLSTEIN, Annals of Physics 21, 494 (1963)
- [14] Yu A. FIRSOV, Fizika Tverdogo Tela 5, 2149 (1963)
- [15] M. KLINGER, phys. stat. sol. 11, 499 (1965)
- [16] J. SCHNAKENBERGH, Z. für Phys. 185, 123 (1965)
- [17] L. FRIEDMAN, Conf. on Electronic Processes in low mobility solids, Sheffield (1966)
- [18] R. WOLFE, WAPD-270 (1963)
- [19] R. DE CONINCK in "Physical properties of UO₂ single crystals" EURAEC Report, R.2362 (1965)
- [20] R. ADAMS and E. DAVISSON, ORNL-3649 (1955)
- [21] R. DE CONINCK and M. HEERSCHAP, "Colloque de la Soc. Européenne d'Energie Atomique, Grenoble, 25-27 juin (1962)
- [22] J. BATES, Proc. Symposium "Thermodynamics", I.A.E.A., Vienna, Austria, July 22-27 (1965)
- [23] S. ARONSON, J. RULLI and B. SCHANER, J. Chem. Phys. 35, 1382 (1961)
- [24] M. KARKHANAVALA and R. CARROLL, ORNL-3093 (1961)
- [25] G. ACKET, Thesis, University of Utrecht (1965)
- [26] R. HOWARD and A. LIDIARD, Rep. Progr. Phys. 27, 161 (1964)

- [27] K. WIRTZ, Phys. Z. 44, 221 (1943)
- [28] J. WILLIAMS, A report to a Panel of I.A.E.A., Vienna, March 16-20, 1964 (p.13)
- [29] G. DOLLING, R. COWLEY and A. WOODS, Can. J. Phys. 43, 1397 (1965)
- [30] J. BELLE, Uranium Dioxide properties and nuclear applications, USAEC (1961) (p. 223)
- [31] I. LANG and Yu FIRSOV, Soviet Phys. J. Exp. Theor. Phys. 16, 1301 (1963)
- [32] J. YAMASHITA and T. KUROSAWA, J. Phys. Chem. Solids 5, 34 (1958)
- [33] D. EAGLES, Phys. Rev. 130, 1381 (1963)
- [34] A. AUSKERN and J. BELLE, J. Nucl. Mat. 3, 311 (1961)
- [35] R. LINDNER and F. SCHMITZ, Z. Naturf. 16a, 1373 (1961)
- [36] P. McNAMARA, Thesis, London (1963)
- [37] L. DE JONGHE, W. VAN LIERDE and R. GEUENS, J. Sci. Instr. 43, 325 (1966)
- [38] J. LAURENT and J. BERNARD, J. Phys. Chem. Solids 7, 218 (1958)
- [39] M. SHIM and W. MOORE, J. Chem. Phys. 26, 802 (1957)
- [40] Physical properties of UO₂ single crystals, EUR 1414e (1965)
- [41] A. OVERHAUSER, Phys. Rev. 94, 1551 (1954)
- [42] Physical properties of UO₂ single crystals, EUR 2042e (1965)
- [43] M. BALARIN and A. ZETZSCHE, phys. stat. sol. 2, 1670 (1962)
- [44] M. BALARIN and A. ZETZSCHE, phys. stat. sol. K387 (1963)
- [45] Present report, paragr. 7!
- [46] A. AUSKERN and J. BELLE, J. Nucl. Mat. 3, 267 (1961)
- [47] B. WILLIS, AERE-R.4487 ; Nature, London 197, 755 (1963)
- [48] A. NOWICK and W. HELLER, Adv. in Phys. 12, 251 (1963)
- [49] Physical Properties of UO₂ single crystals, Quarterly Report No. 12, R.2354 (1965)
- [50] L. WEIL and J. COHEN, J. Phys. Rad. 24, 76 (1963)
- [51] A. ARROTT and J. GOLDMAN, Phys. Rev. 108, 948 (1957)
- [52] W. TRZEBIATOWSKI and P. SELWOOD, J. Am. Chem. Soc. 72, 4504 (1950)
- [53] K. GOTOO, S. NOMURA and K. NAITO, J. Phys. Chem. Solids 26, 1679 (1965)
- [54] M. VERSCHUEREN, SCK-R.2280 (1964)

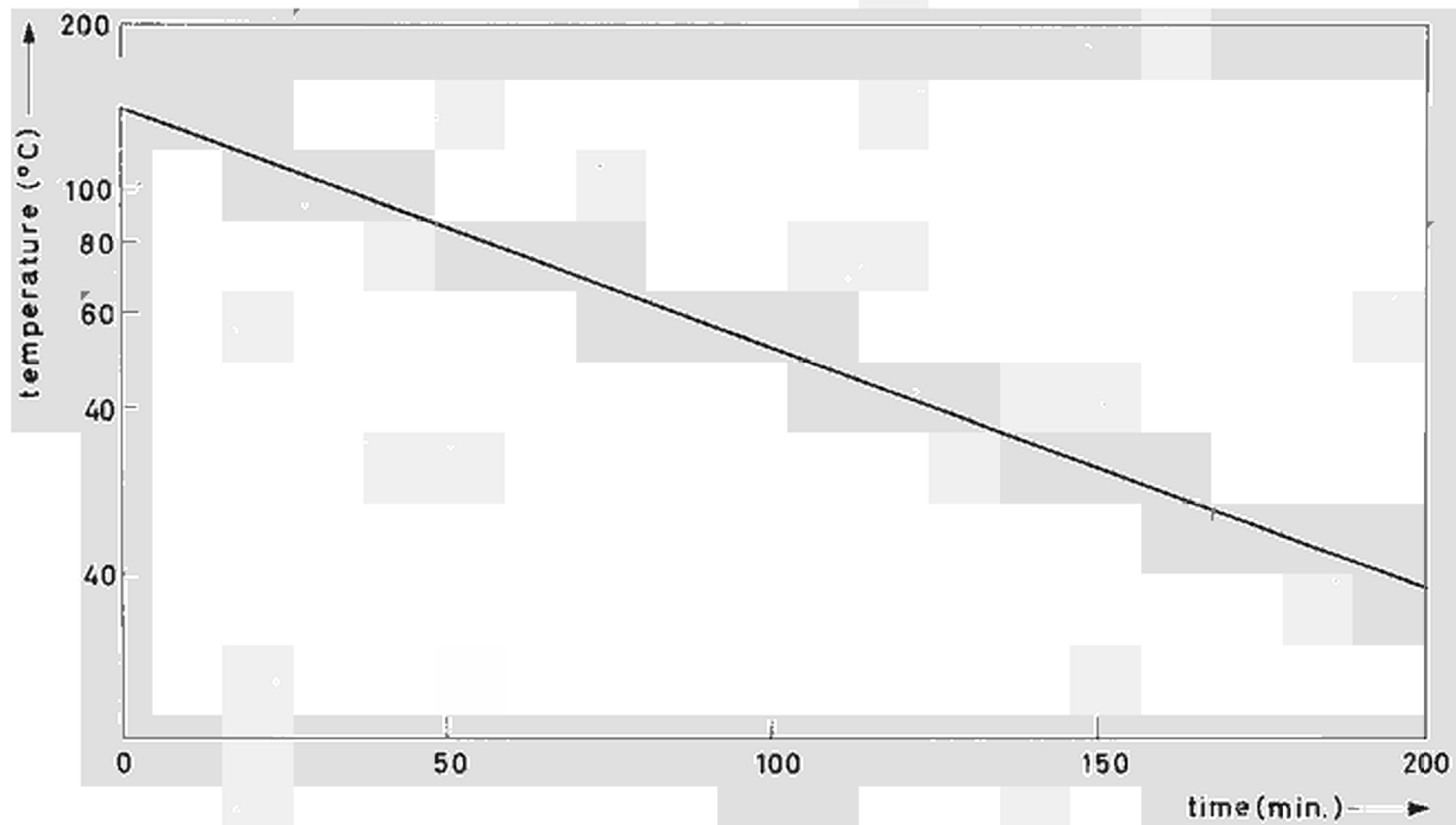
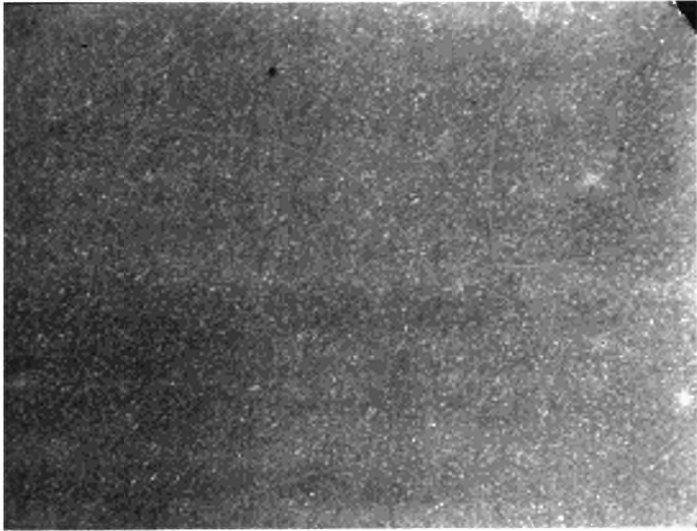


Fig. 1

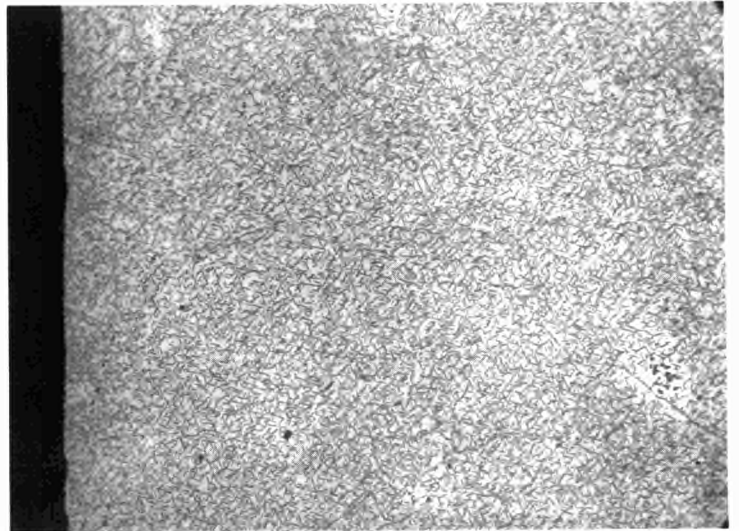
Cooling rate of UO_2 single crystals after oxidation at 1400°C

Fig. 2

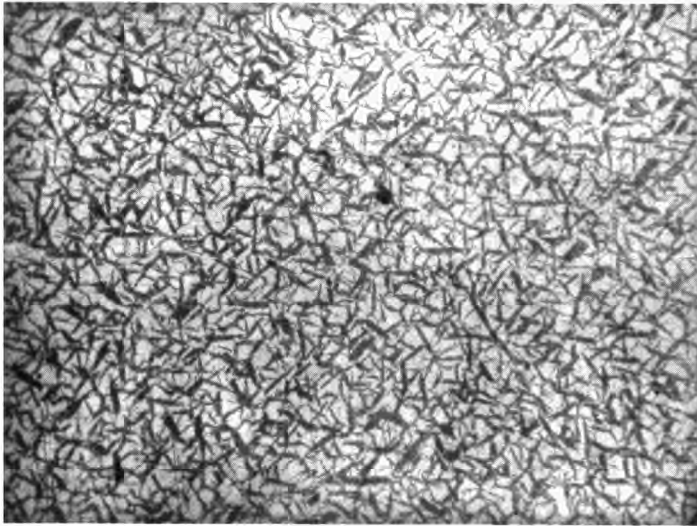
polished and stain-etched surfaces of UO_2 single crystals as observed by reflection in the optical microscope



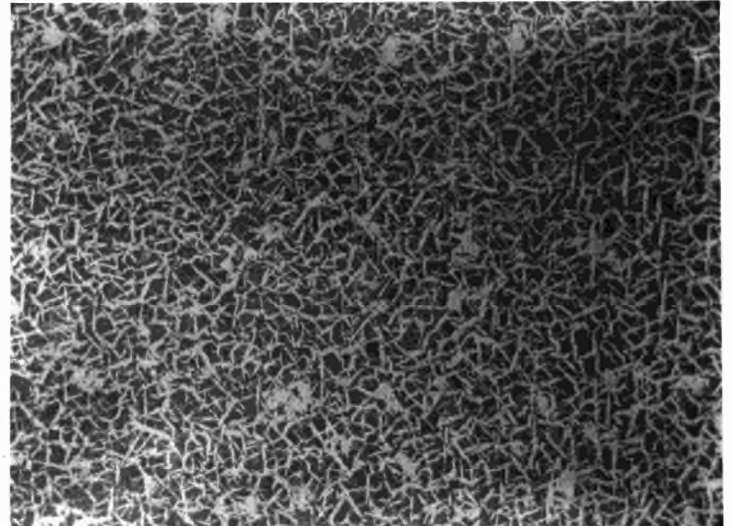
a) U_4O_9 bright regions, $O/U = 2.013$ ($\times 150$)



b) U_4O_9 dark regions, $O/U = 2.041$ ($\times 150$)



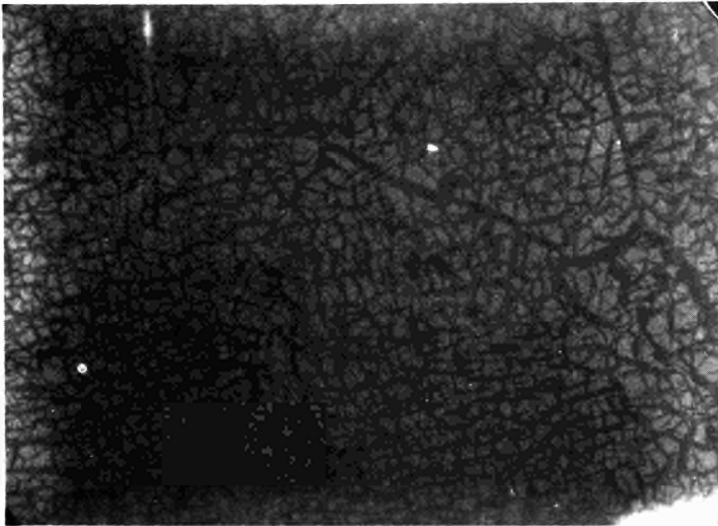
c) U_4O_9 dark regions, $O/U = 2.08$ ($\times 150$)



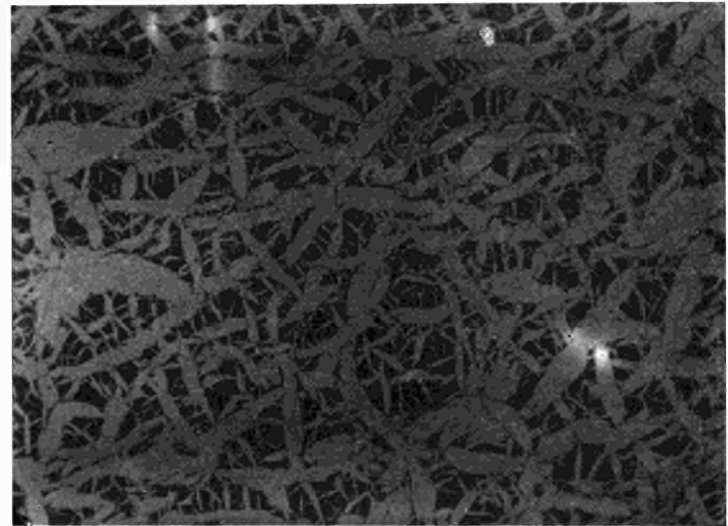
d) U_4O_9 bright regions, $O/U = 2.11$ ($\times 150$)

Fig. 2

Polished and stain-etched surfaces of UO_2 single crystals as observed by reflection in the optical microscope



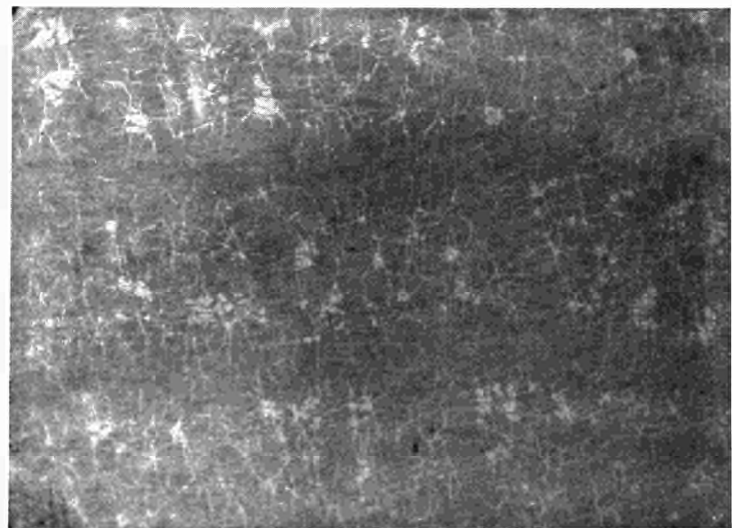
e) U_4O_9 dark regions, $O/U = 2.12$ ($\times 150$)



f) U_4O_9 bright regions, $O/U = 2.17$ ($\times 150$)



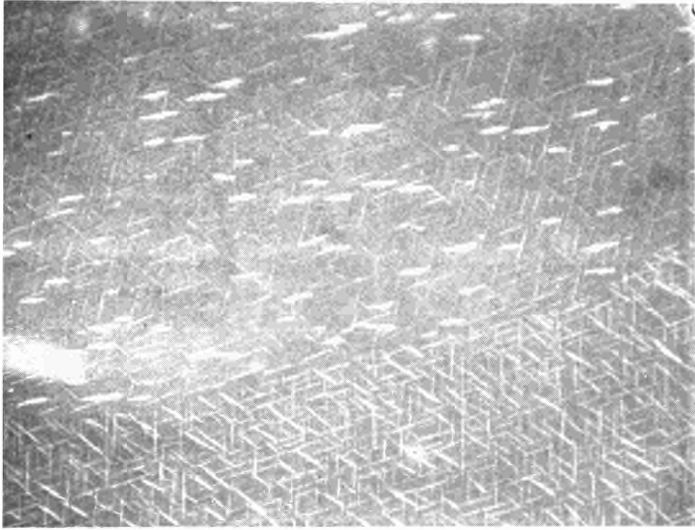
g) U_4O_9 dark regions, $O/U = 2.19$ ($\times 150$)



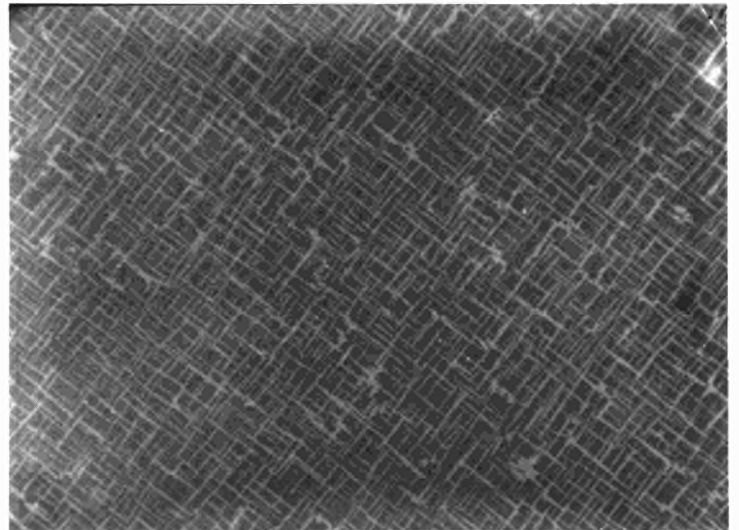
h) U_4O_9 bright regions, $O/U = 2.23$ ($\times 150$)

Fig. 2

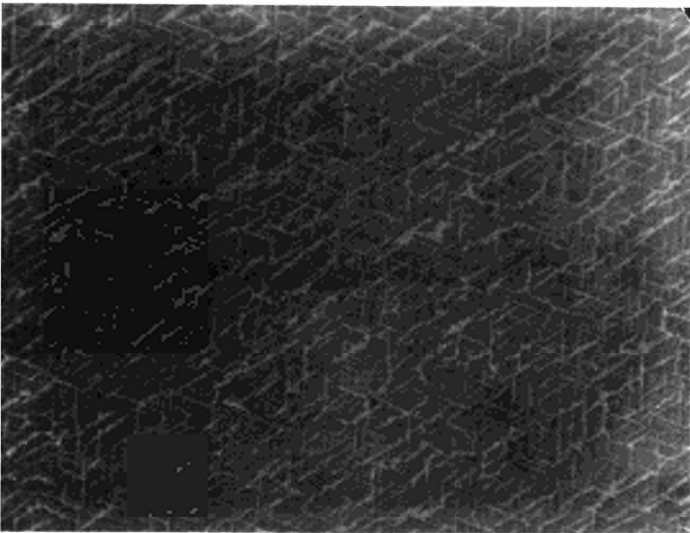
polished and stain-etched surfaces of UO_2 single crystals as observed by reflection in the optical microscope



i) U_4O_9 bright regions, $\text{O}/\text{U} = 2.05$ ($\times 400$)



j) U_4O_9 bright regions, precipitations in the $\{100\}$ plane, $\text{O}/\text{U} = 2.056$ ($\times 400$)



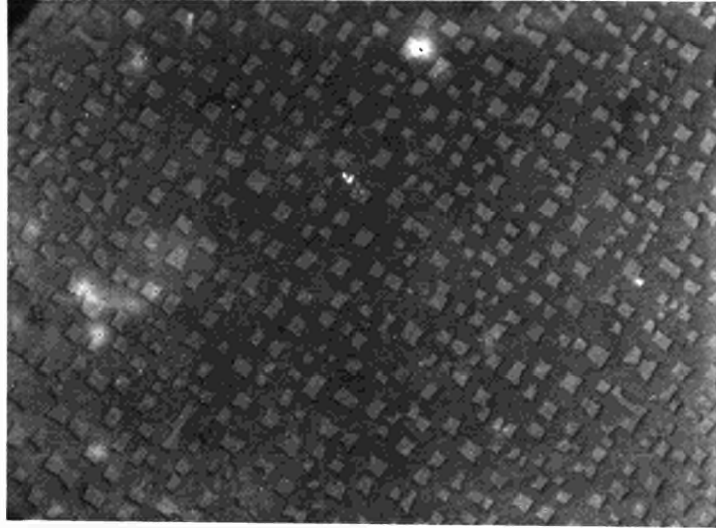
k) U_4O_9 bright regions, precipitations in the $\{110\}$ plane, $\text{O}/\text{U} = 2.056$ ($\times 400$)



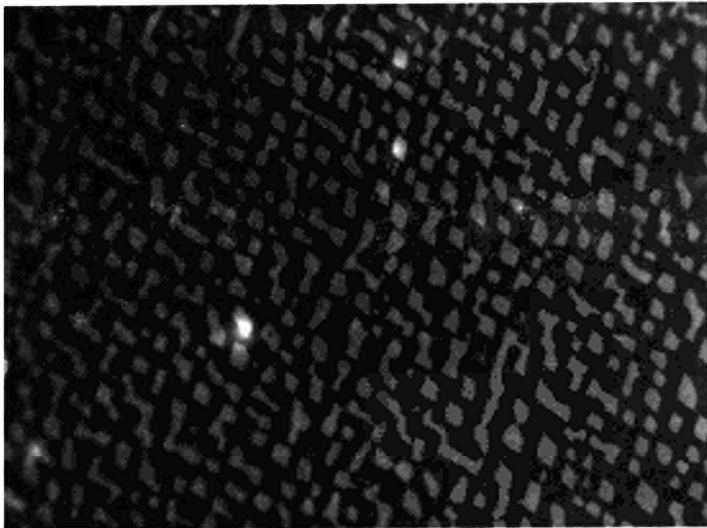
l) U_4O_9 bright regions, precipitations in the $\{111\}$ plane, $\text{O}/\text{U} = 2.056$ ($\times 400$)

Fig. 2

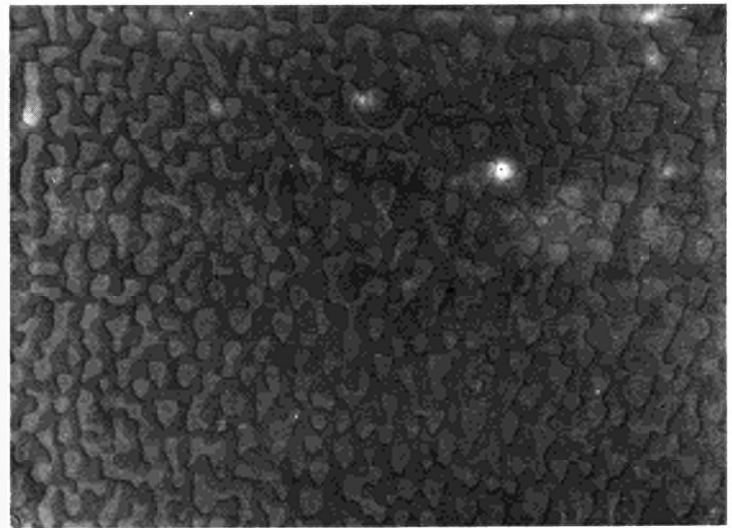
Polished and stain-etched surfaces of UO_2 single crystals as observed by reflection in the optical microscope



m) U_4O_9 bright regions, surface precipitations
in the $\{100\}$ plane, $O/U = 2.056$ ($\times 400$)



n) U_4O_9 bright regions, surface precipitations
in the $\{110\}$ plane, $O/U = 2.056$ ($\times 400$)



o) U_4O_9 bright regions, surface precipitations
in the $\{111\}$ plane, $O/U = 2.056$ ($\times 400$)

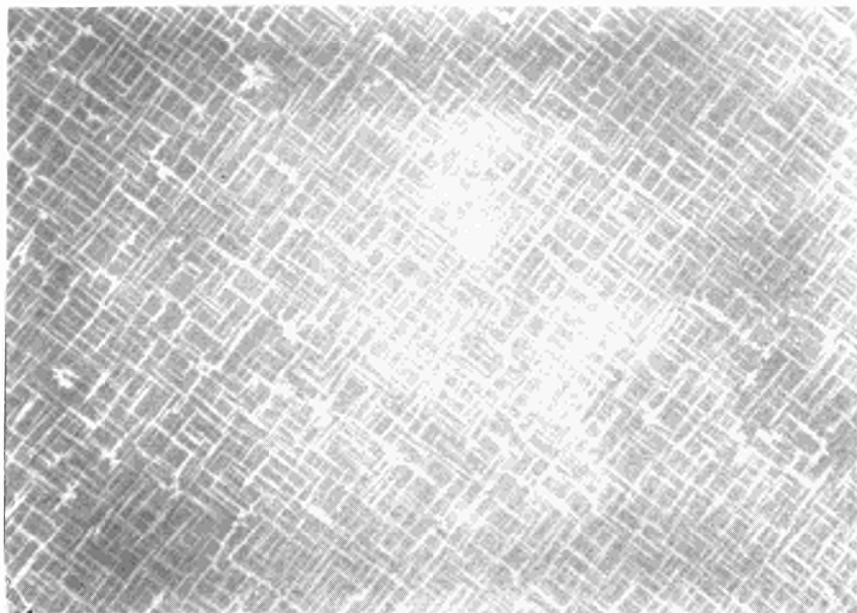


Fig. 3

Polished and stain-etched surface of a $\text{UO}_{2.056}$ single crystal as observed in the optical microscope ($\times 400$)

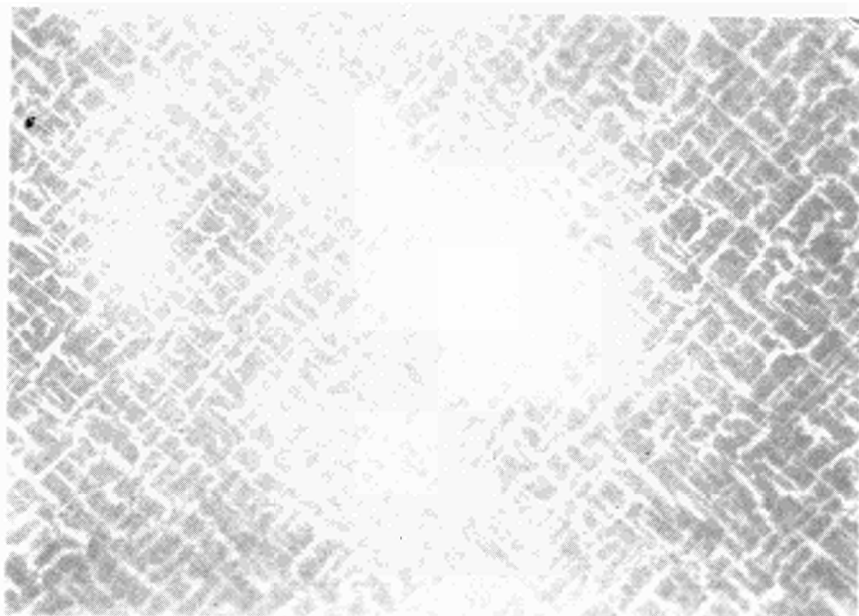


Fig. 4

Surface of the same $\text{UO}_{2.056}$ single crystal after irradiation up to a dose $nvt=1.7 \times 10^{19}$ thermal neutrons. cm^{-2} ($\times 400$)

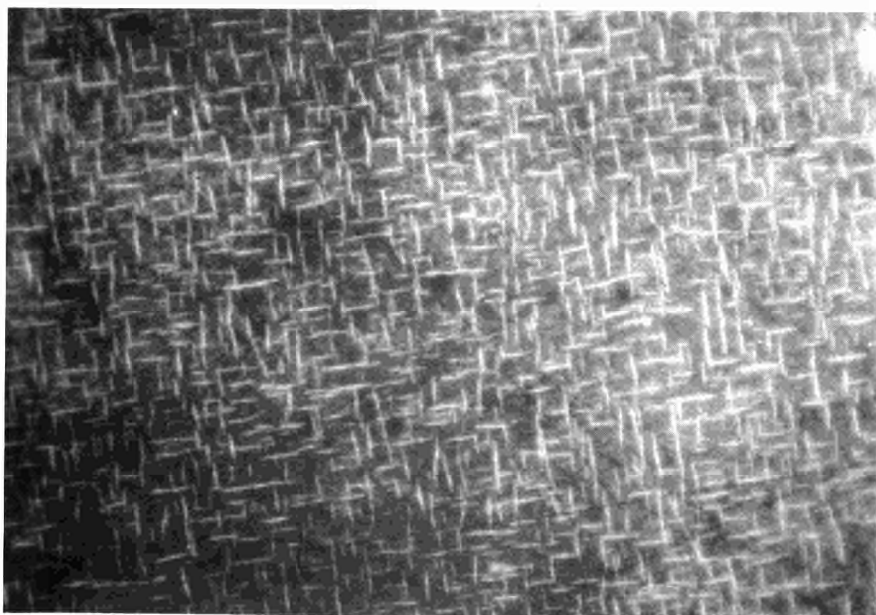


Fig. 5

Polished and stain-etched surface of a $\text{UO}_{2.056}$ single crystal as observed in the optical microscope ($\times 400$) - After irradiation to a dose of 10^{20} thermal neutrons. cm^{-2} no precipitates of U_4O_9 could be detected by optical microscopy

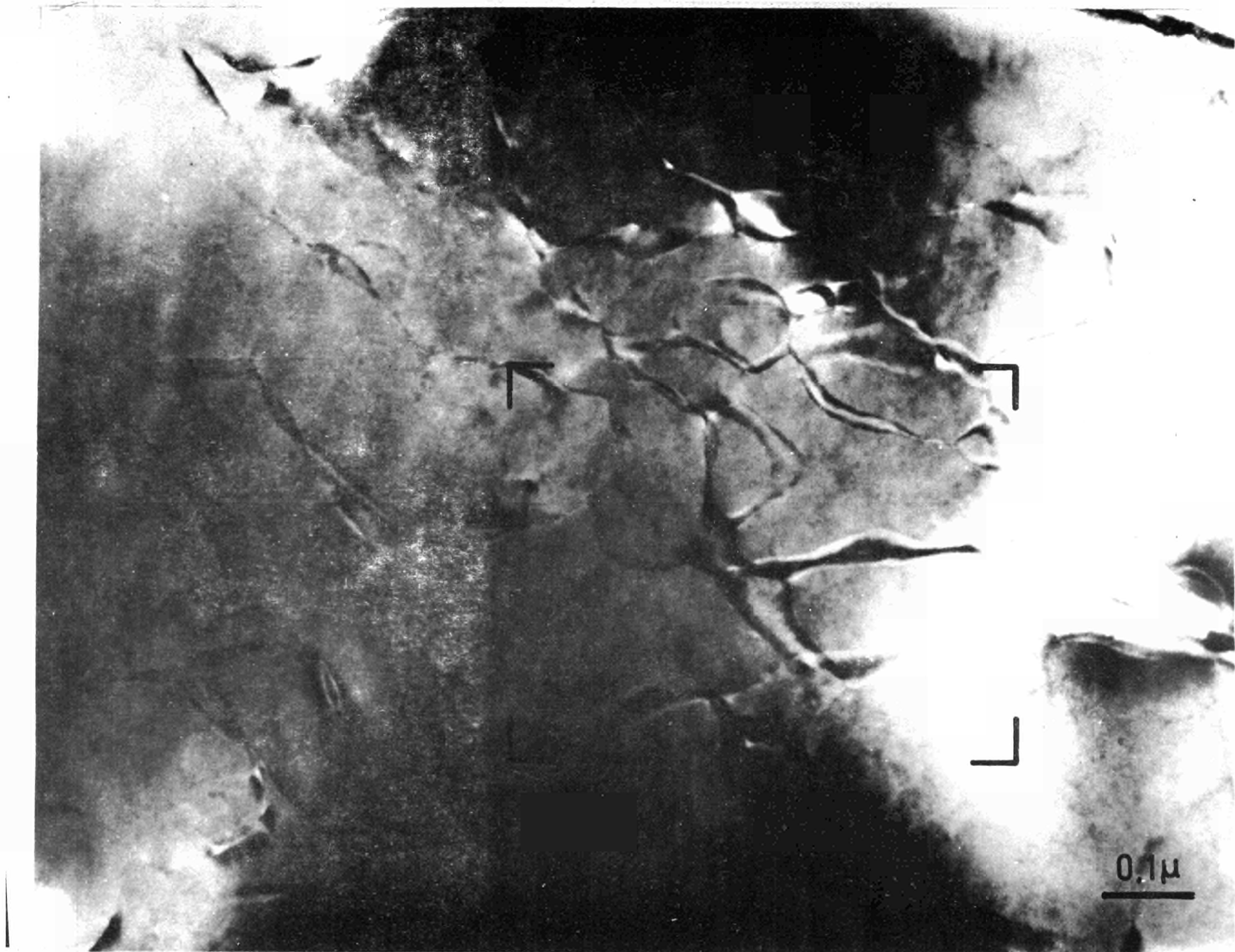


Fig. 6
antiphase boundaries in U_4O_9 crystals

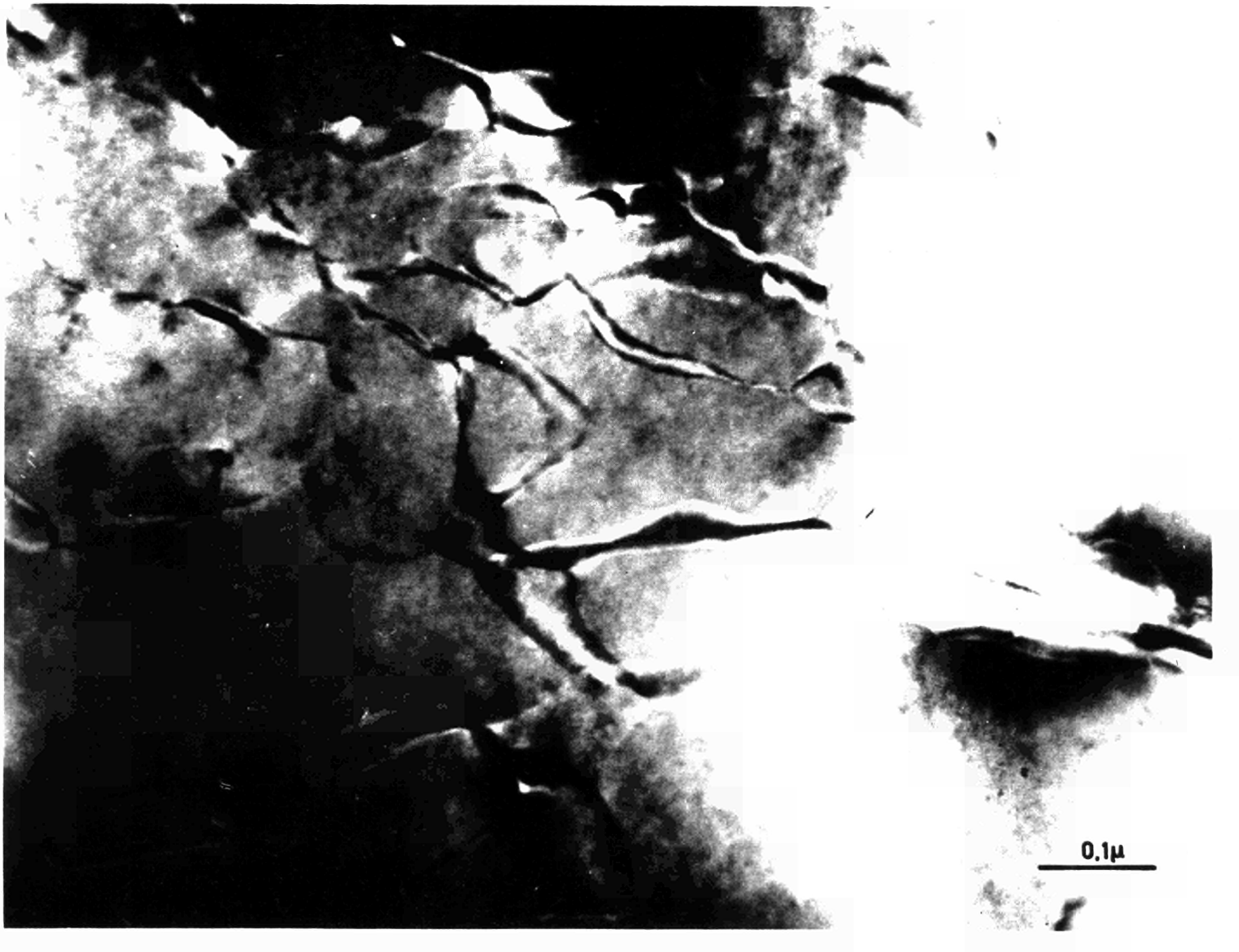


Fig. 7
Magnified part of Fig. 6 to show the detail of

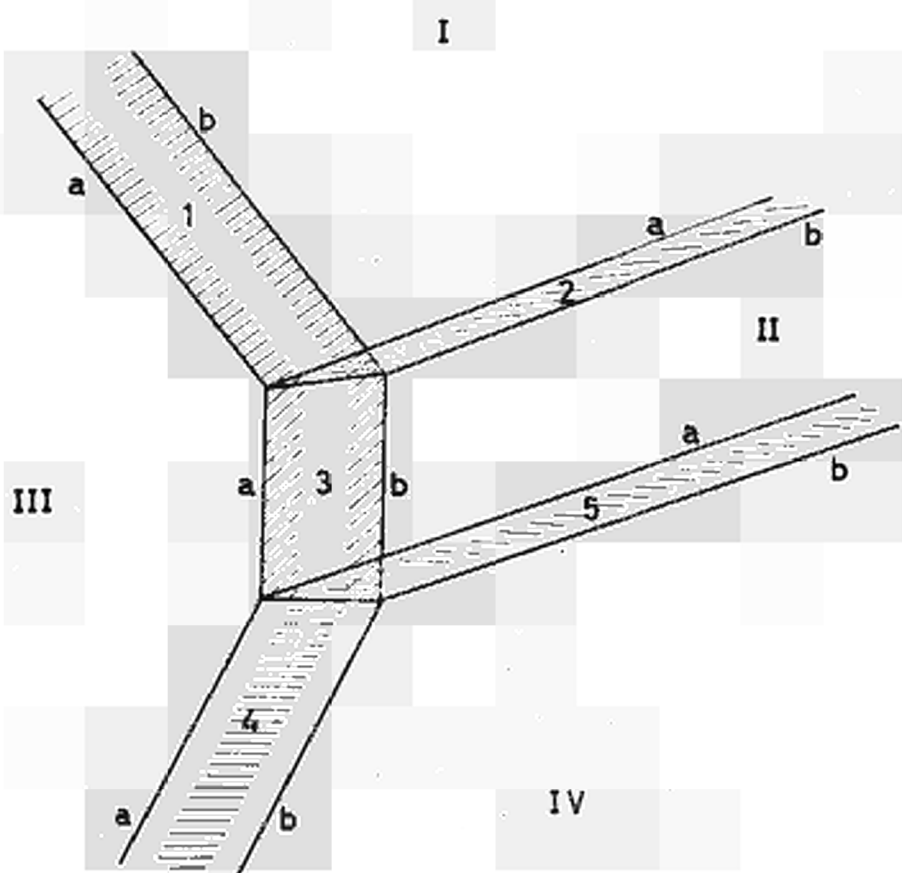


Fig. 8

Schematic representation of Fig. 7

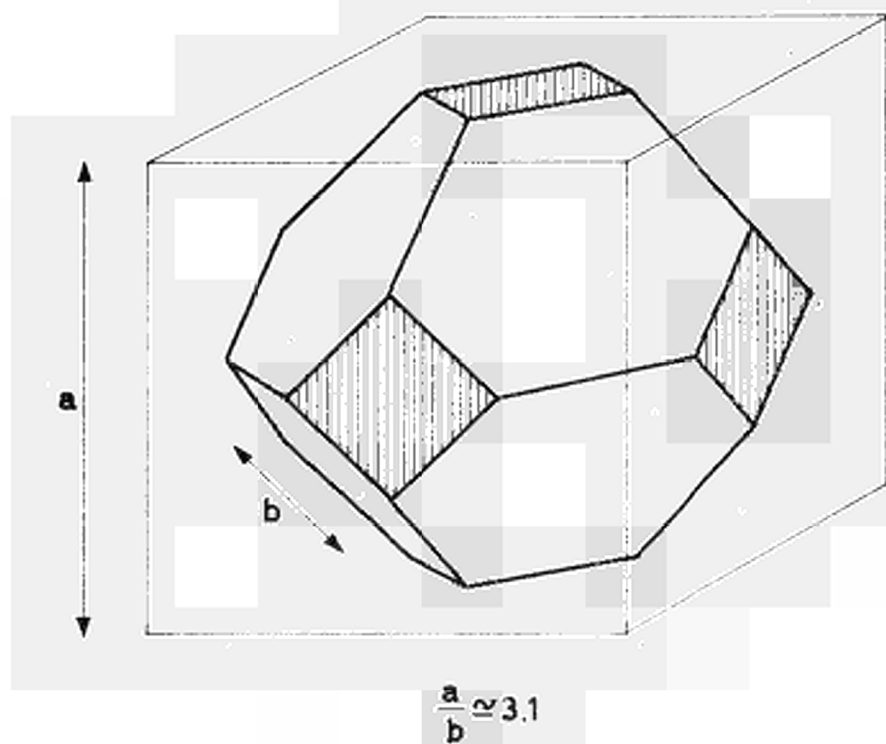
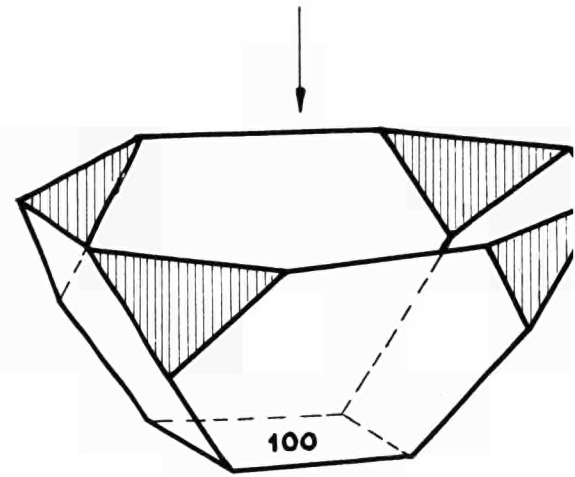
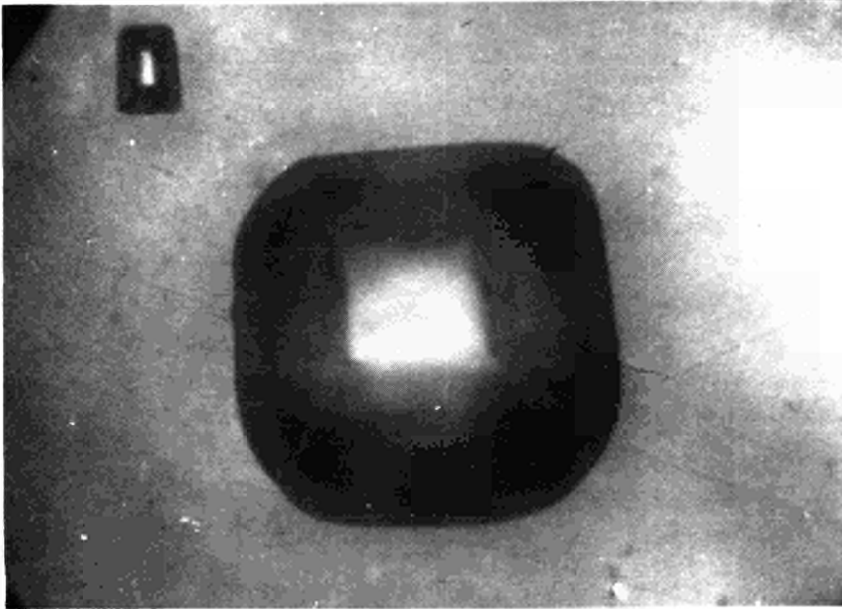


Fig. 9

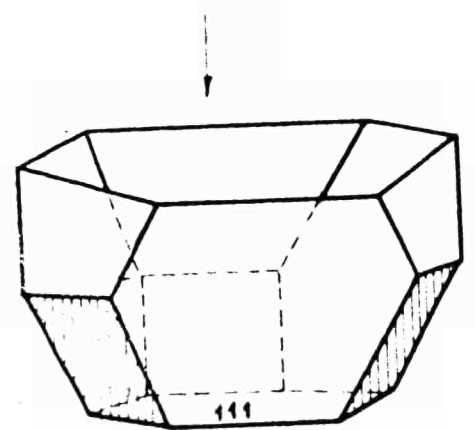
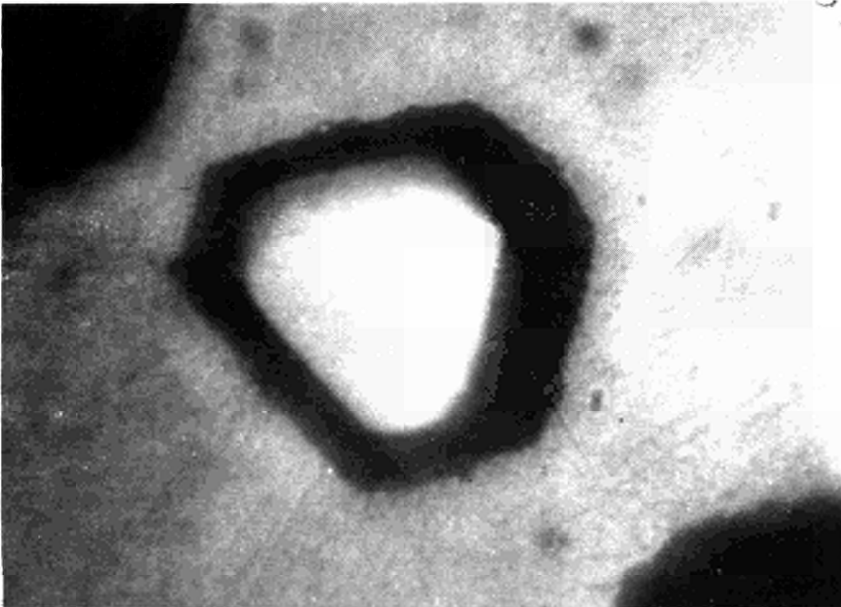
Theoretical pore having the form of a regular polyhedron and consisting of eight $\{111\}$ planes and six $\{100\}$ planes

Fig. 10

Shape of pores as observed after annealing at 1600-1700°C



a) Pore cut by a $\{100\}$ plane ($\times 1500$)



b) Pore cut by a $\{111\}$ plane ($\times 1500$)

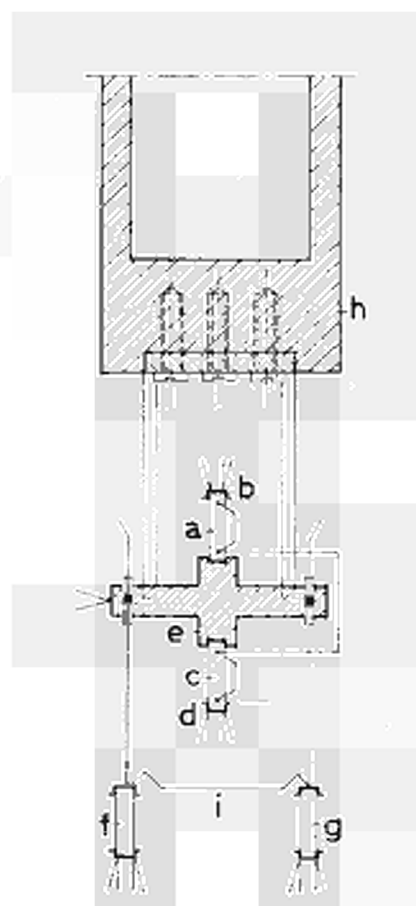


Fig. 11

Arrangement used for the measurement of the thermal conductivity at low temperatures

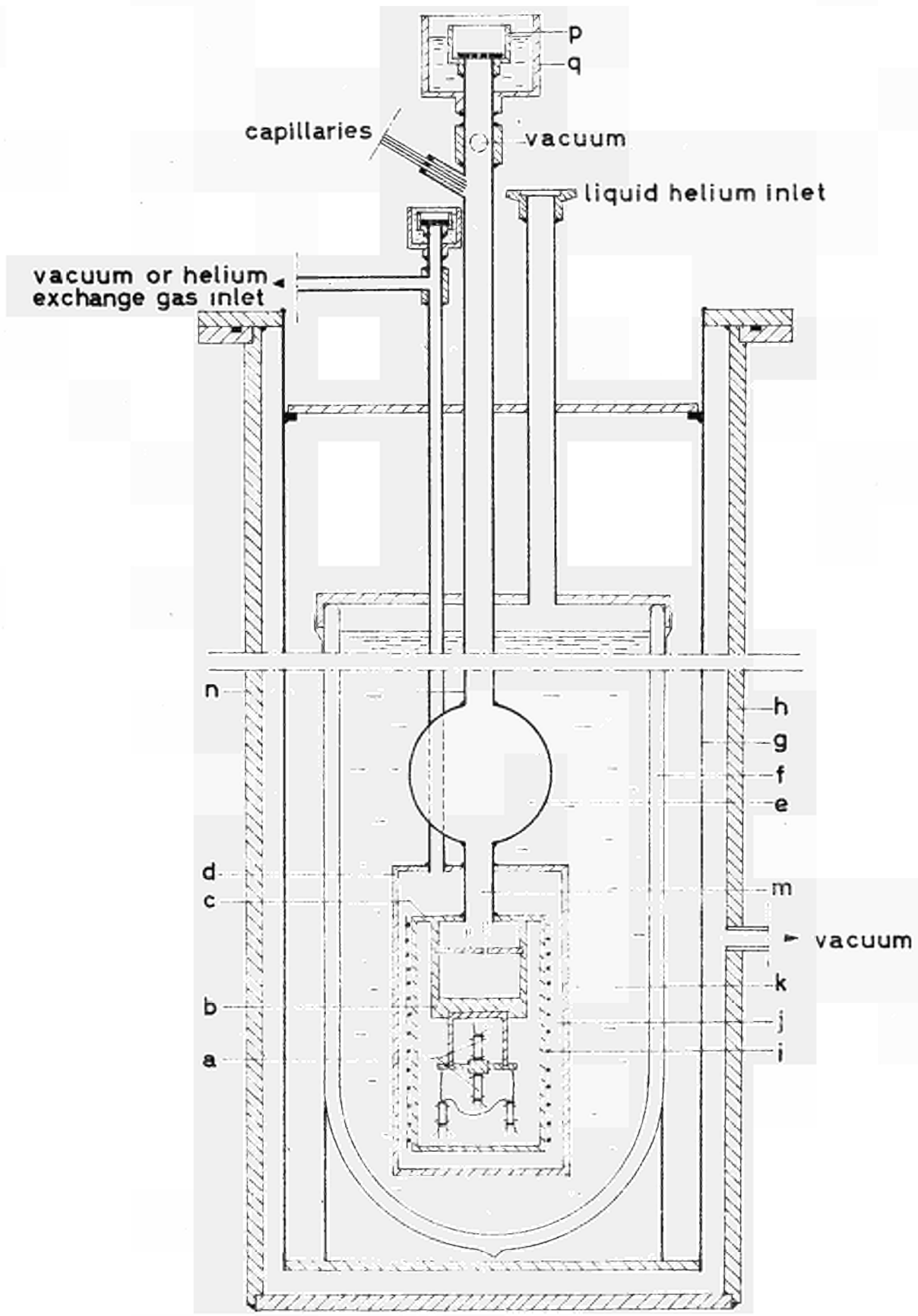


Fig. 12

Schematic drawing of the cryostat used for the thermal conductivity measurements

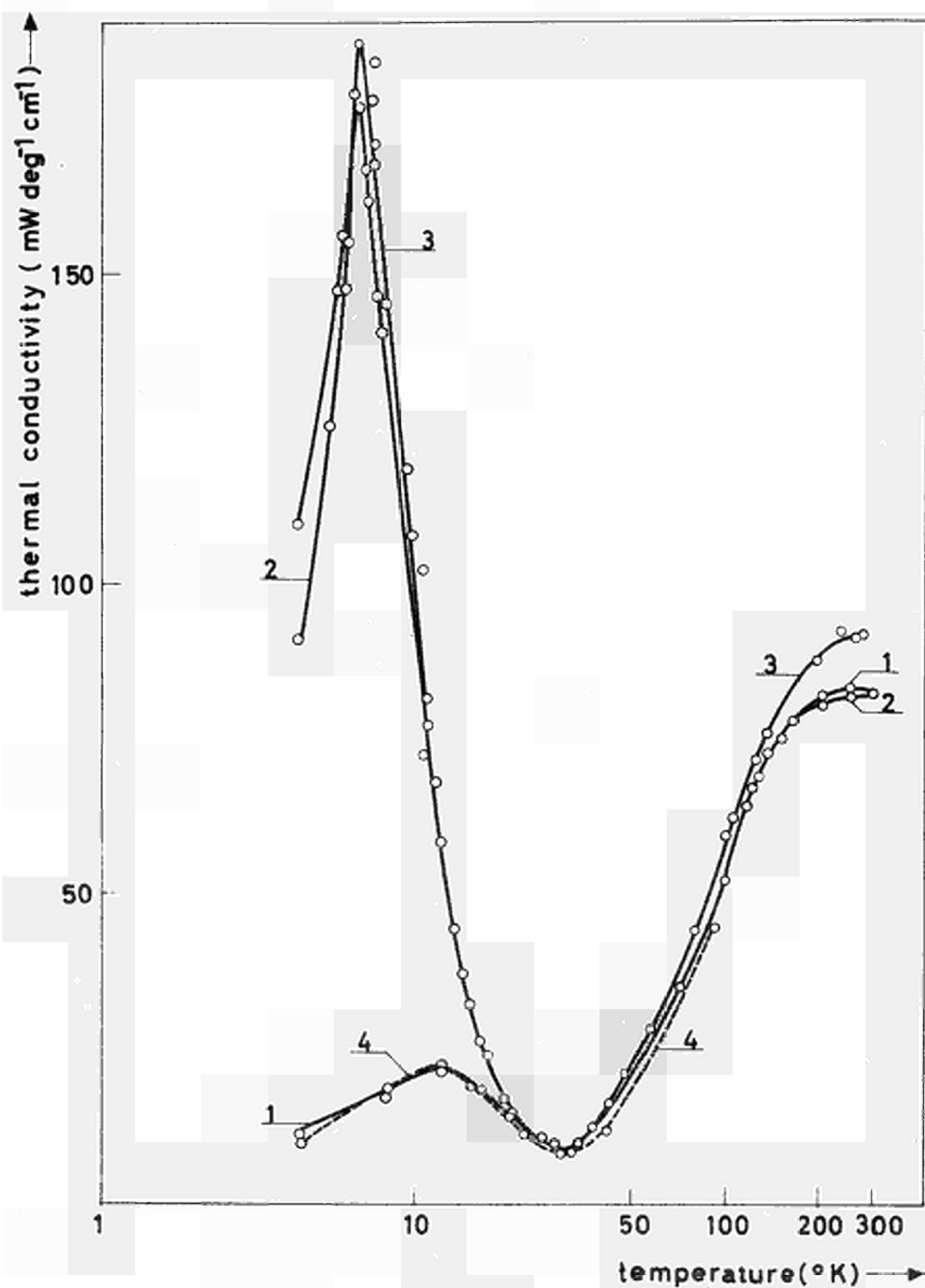


Fig. 13

Thermal conductivity of UO_2 single crystals as a function of temperature (curves 1, 2 and 3) - The dashed line (curve 4) corresponds to measurements made by Bethoux et al. on a sintered UO_2 polycrystal

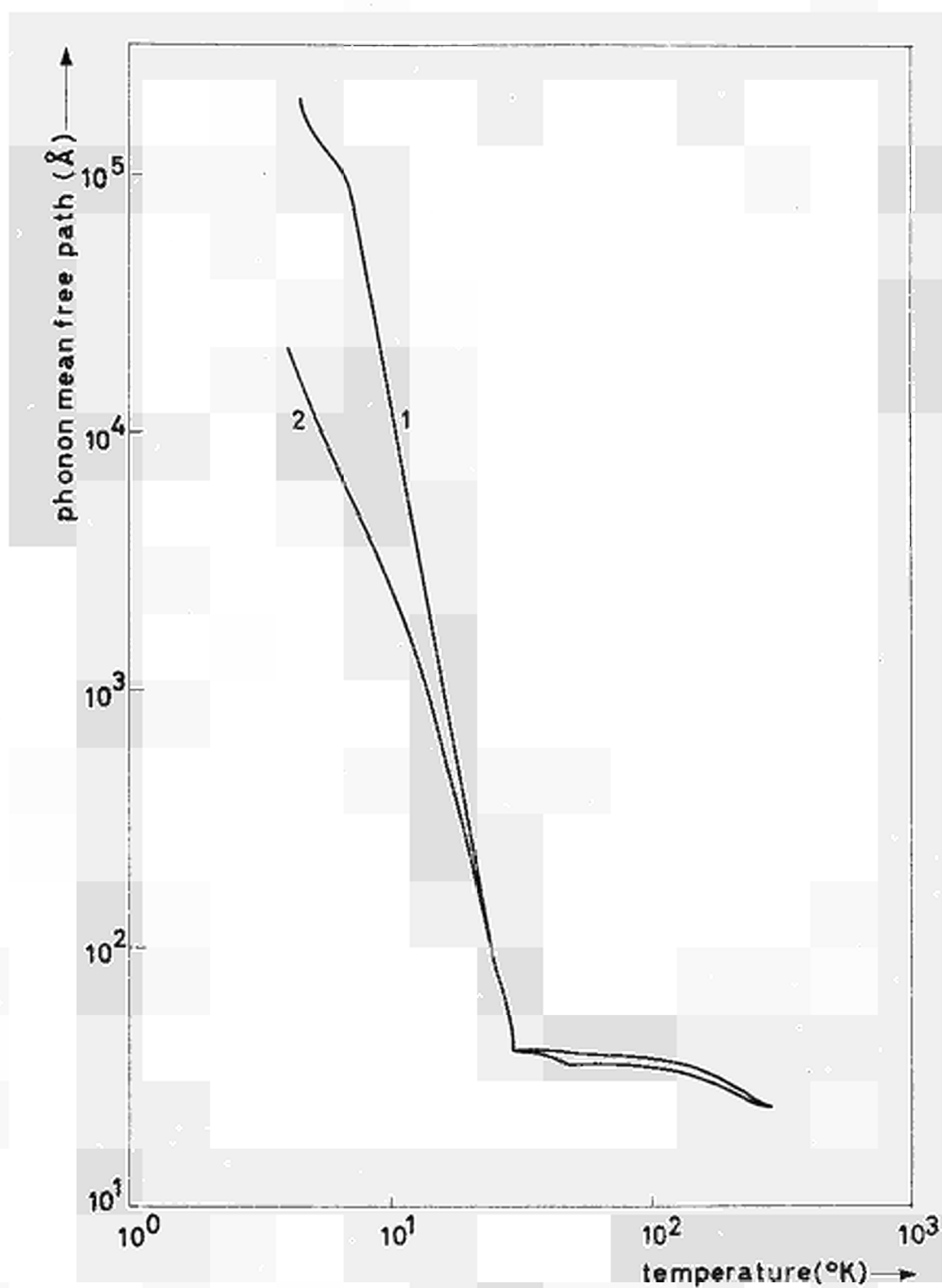


Fig. 14

Phonon mean free path in UO₂ as a function of temperature (curve 1 : nearly stoichiometric UO₂; curve 2 : slightly oxidized UO₂)

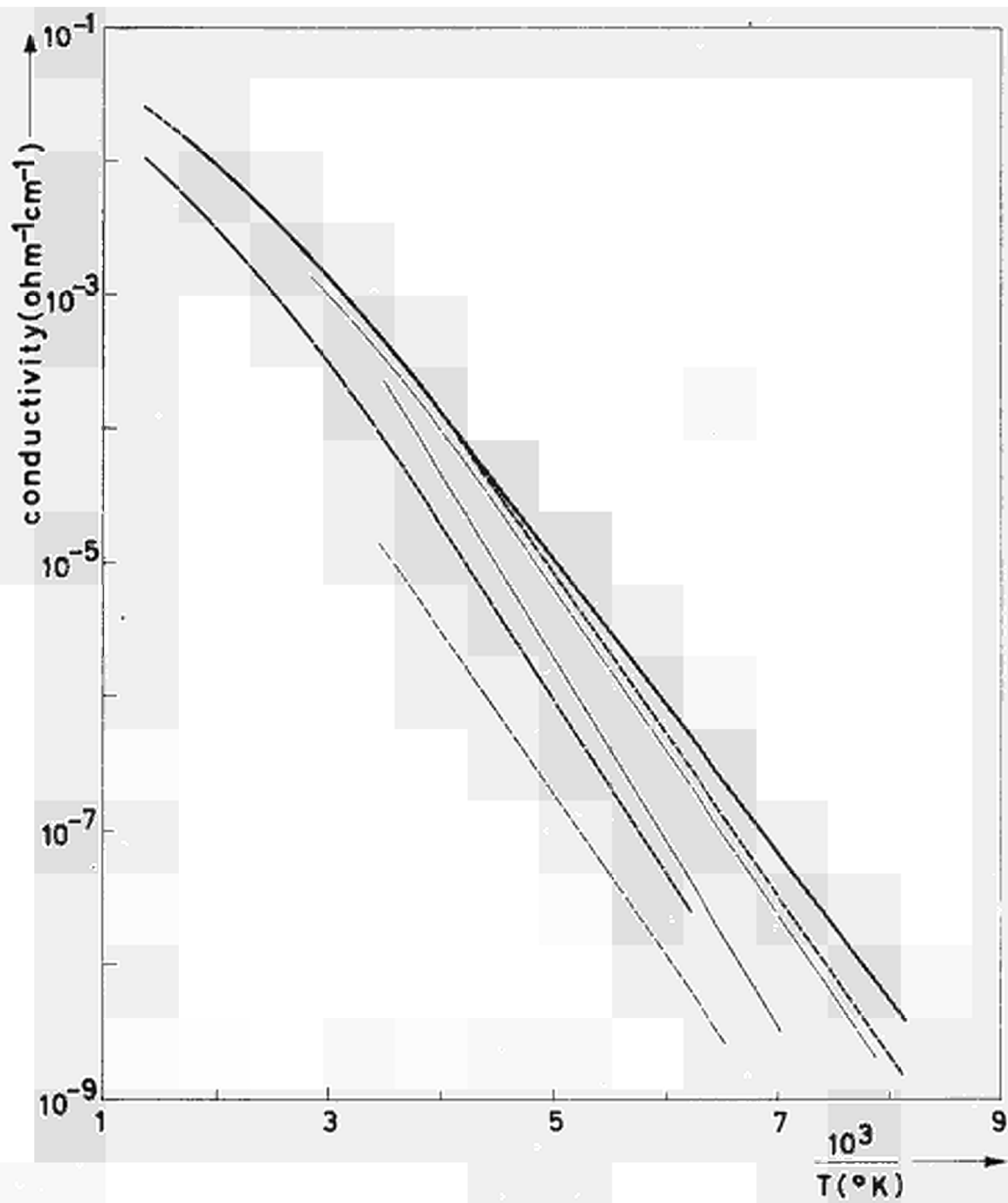


Fig. 15

Electrical conductivity of UO_2 single crystals with iO/U ratios smaller than 2,001

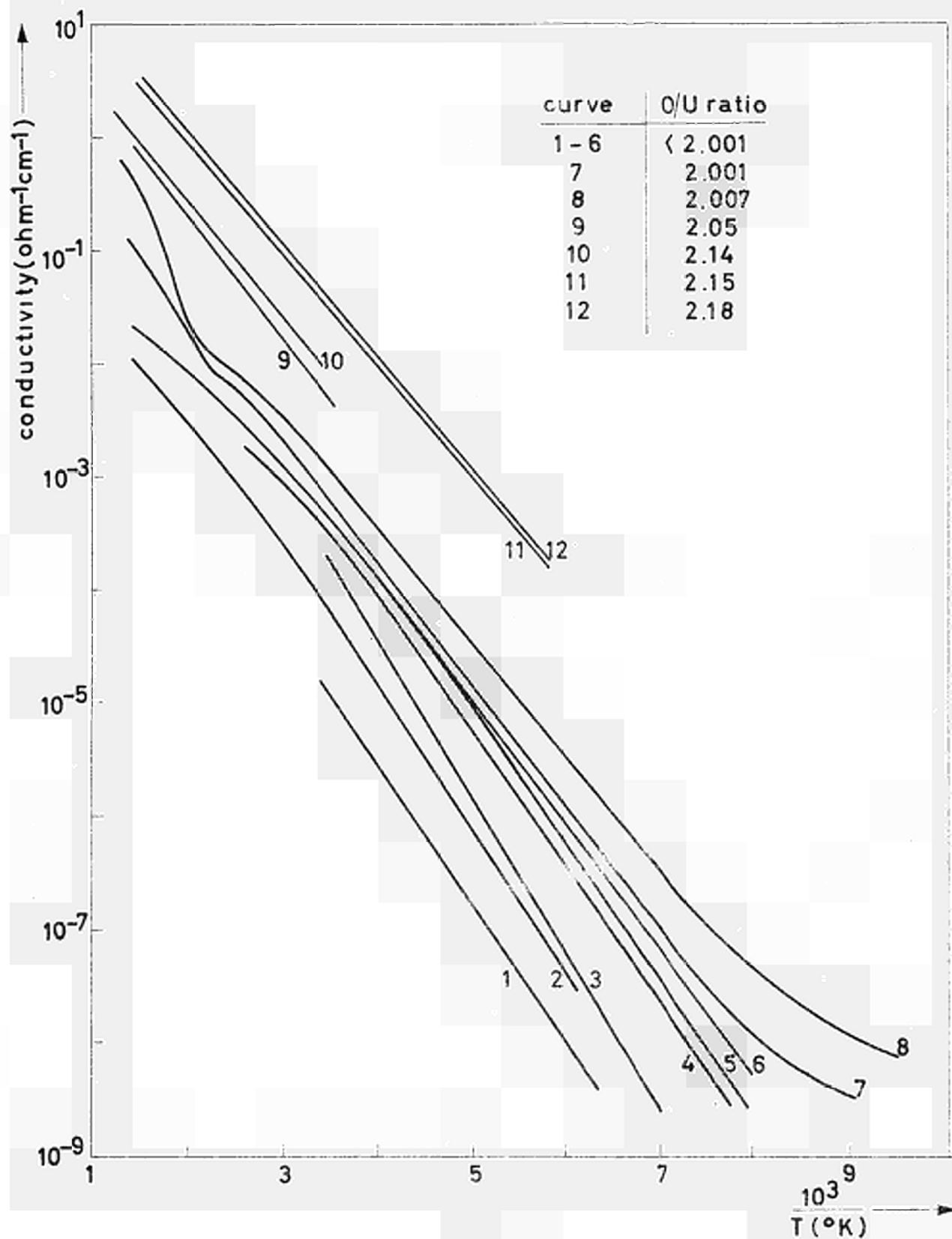


Fig. 16

Complete set of conductivity data of CO_2 single crystals with compositions $0 < x < 0.18$

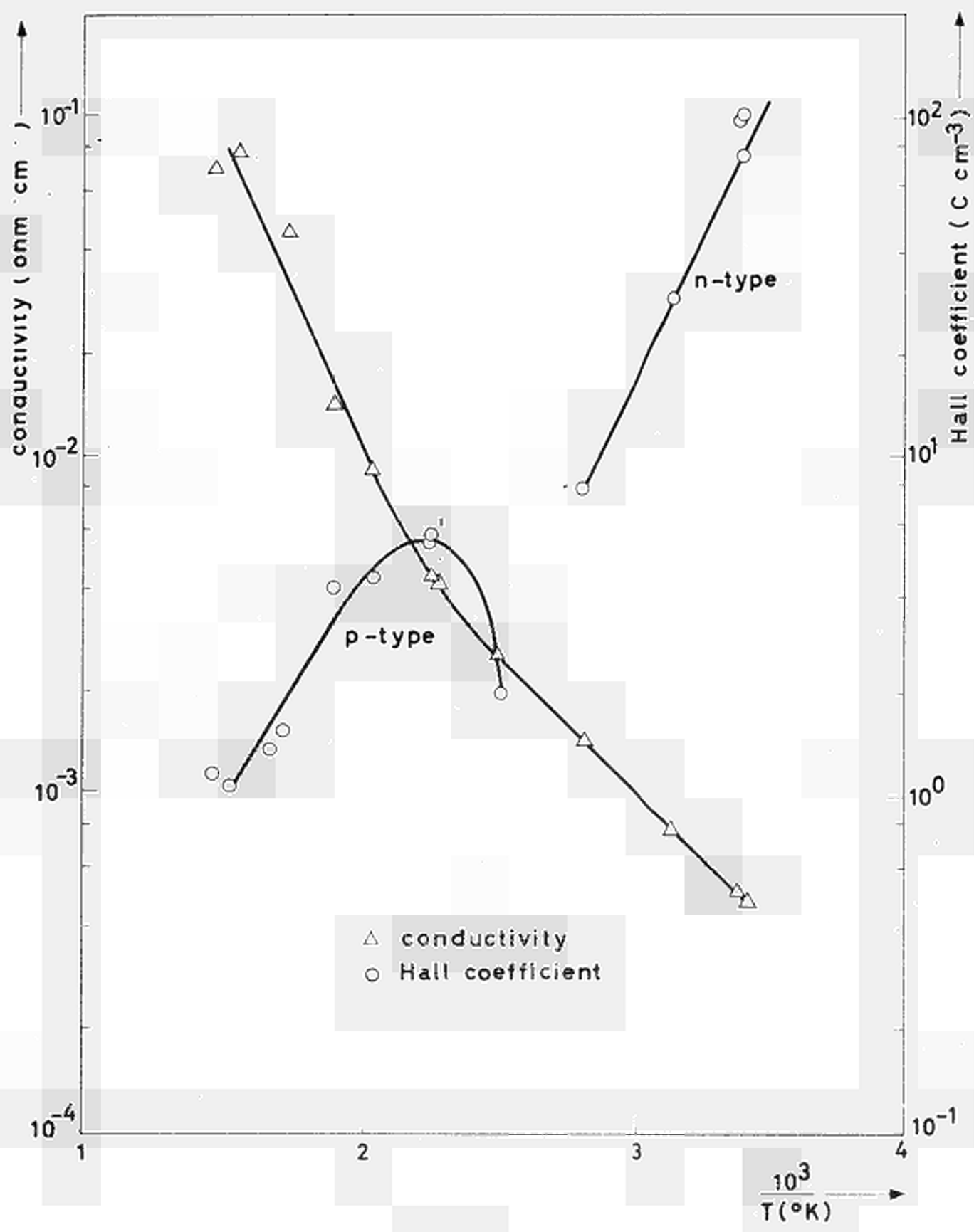


Fig. 17

Conductivity and Hall coefficient of a UO_2 single crystal with $O/U \approx 2.001$ - Notice the reversal of sign of the Hall coefficient

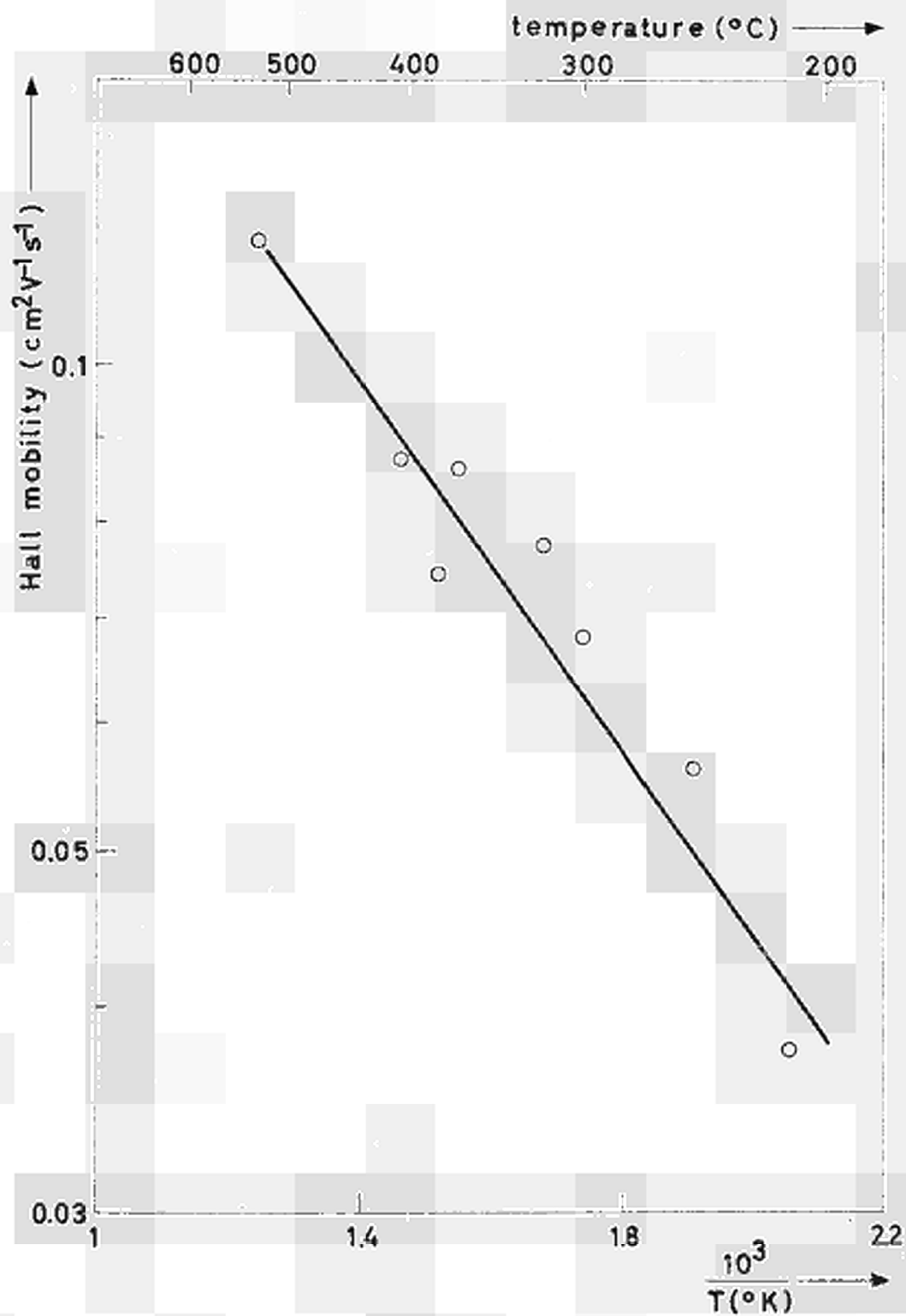


Fig. 18

Hall mobility of a reduced UO_2 single crystal ($0/U < 2,001$) as a function of the reciprocal temperature

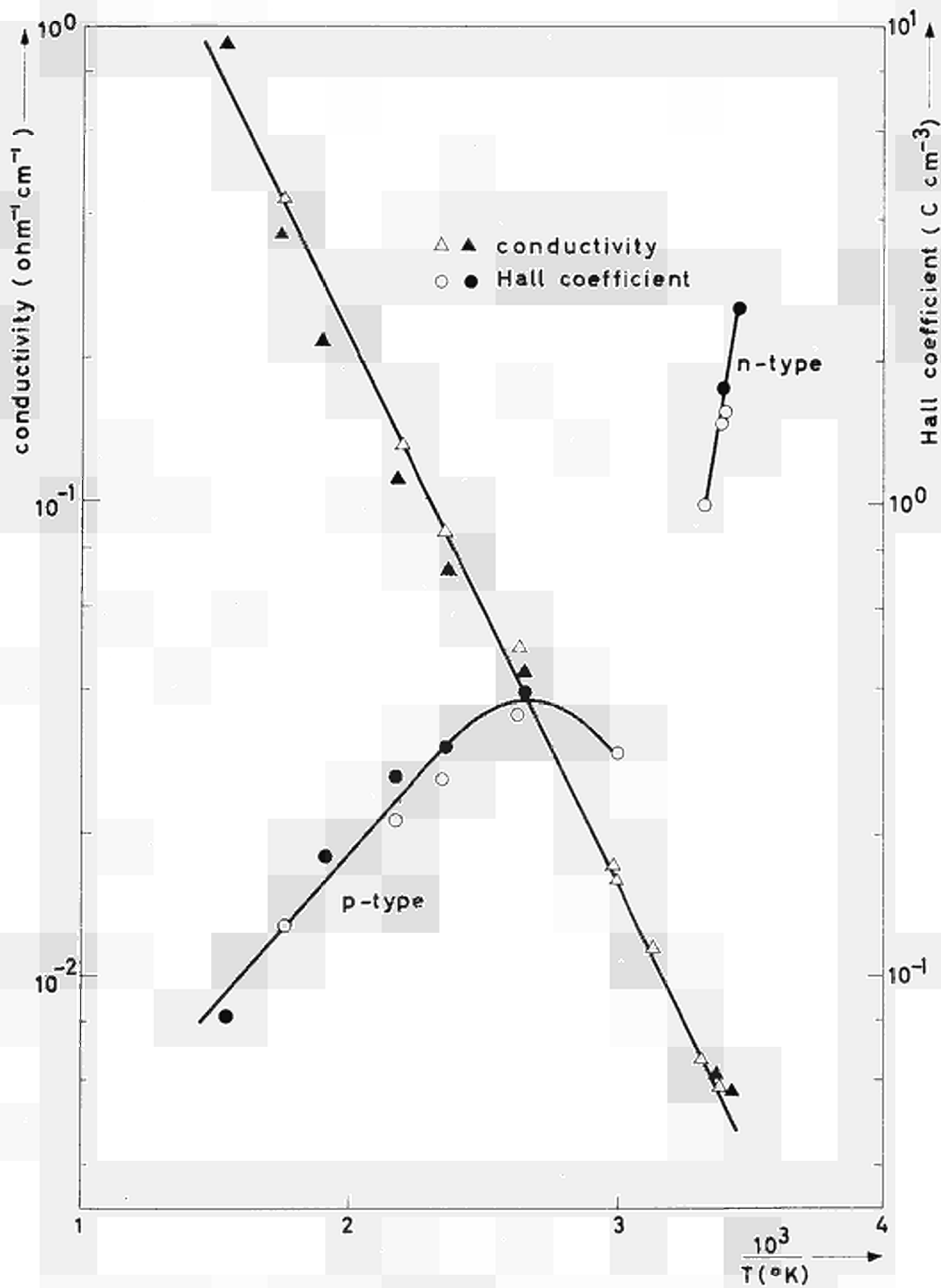


Fig. 19

Conductivity and Hall coefficient as a function of the reciprocal temperature of a UO_2 single crystal with $\text{O/U} \approx 2.03$

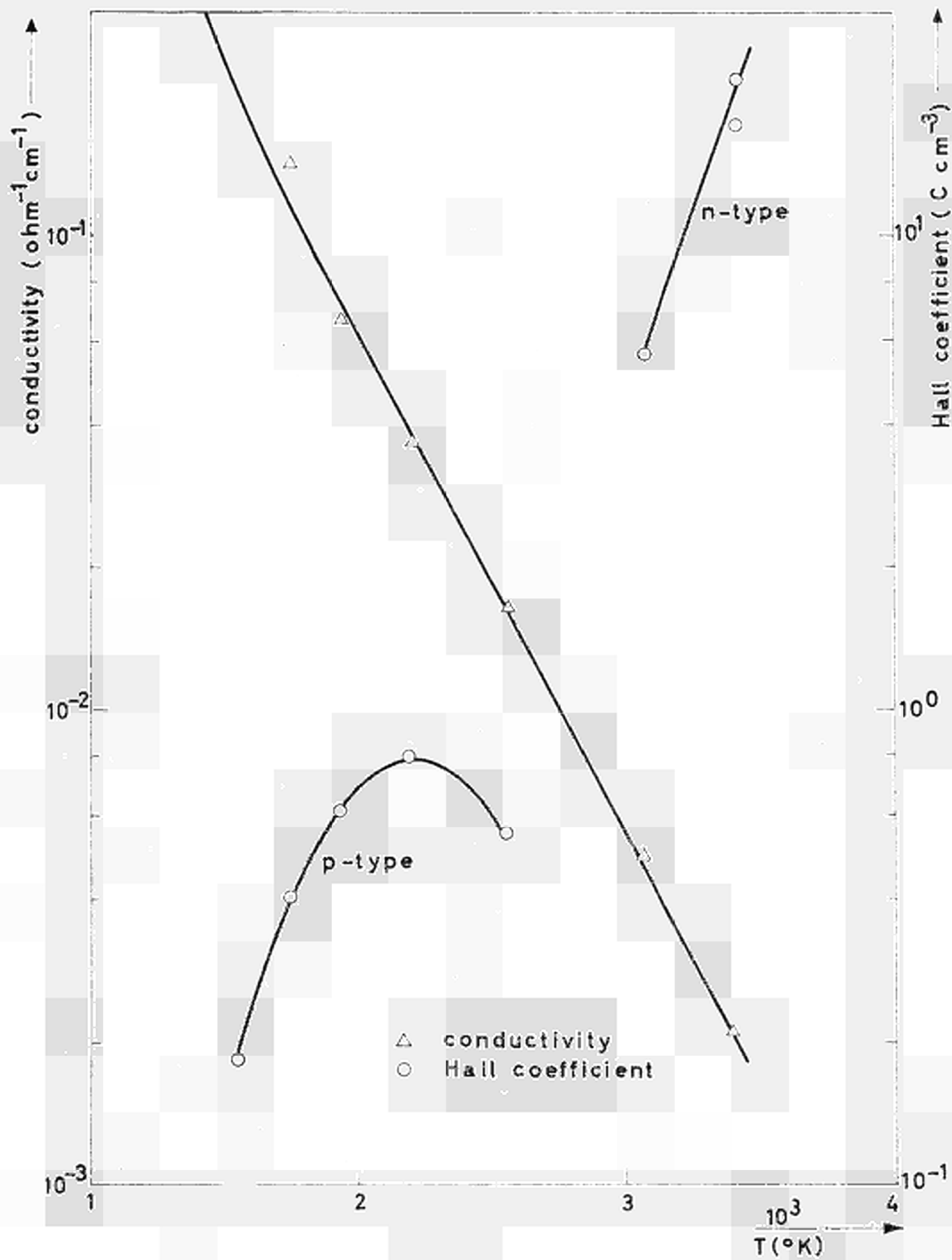


Fig. 40

Conductivity and Hall coefficient as a function of the reciprocal temperature of a UO_2 single crystal with $D/U \approx 2.10$

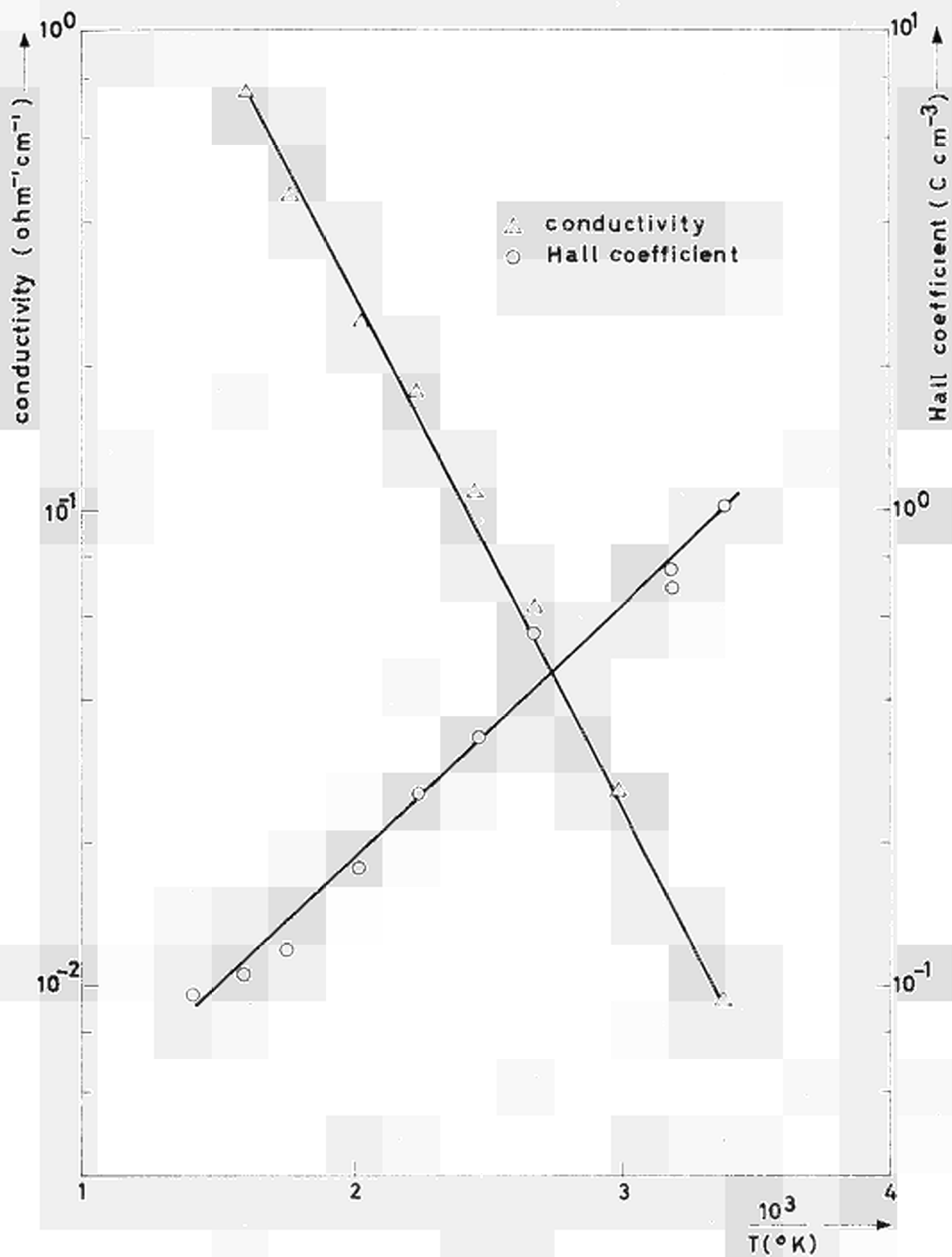


Fig. 21

Conductivity and Hall coefficient as a function of the reciprocal temperature of a UO_2 single crystal with $\theta/\theta_0 \approx 0.14$

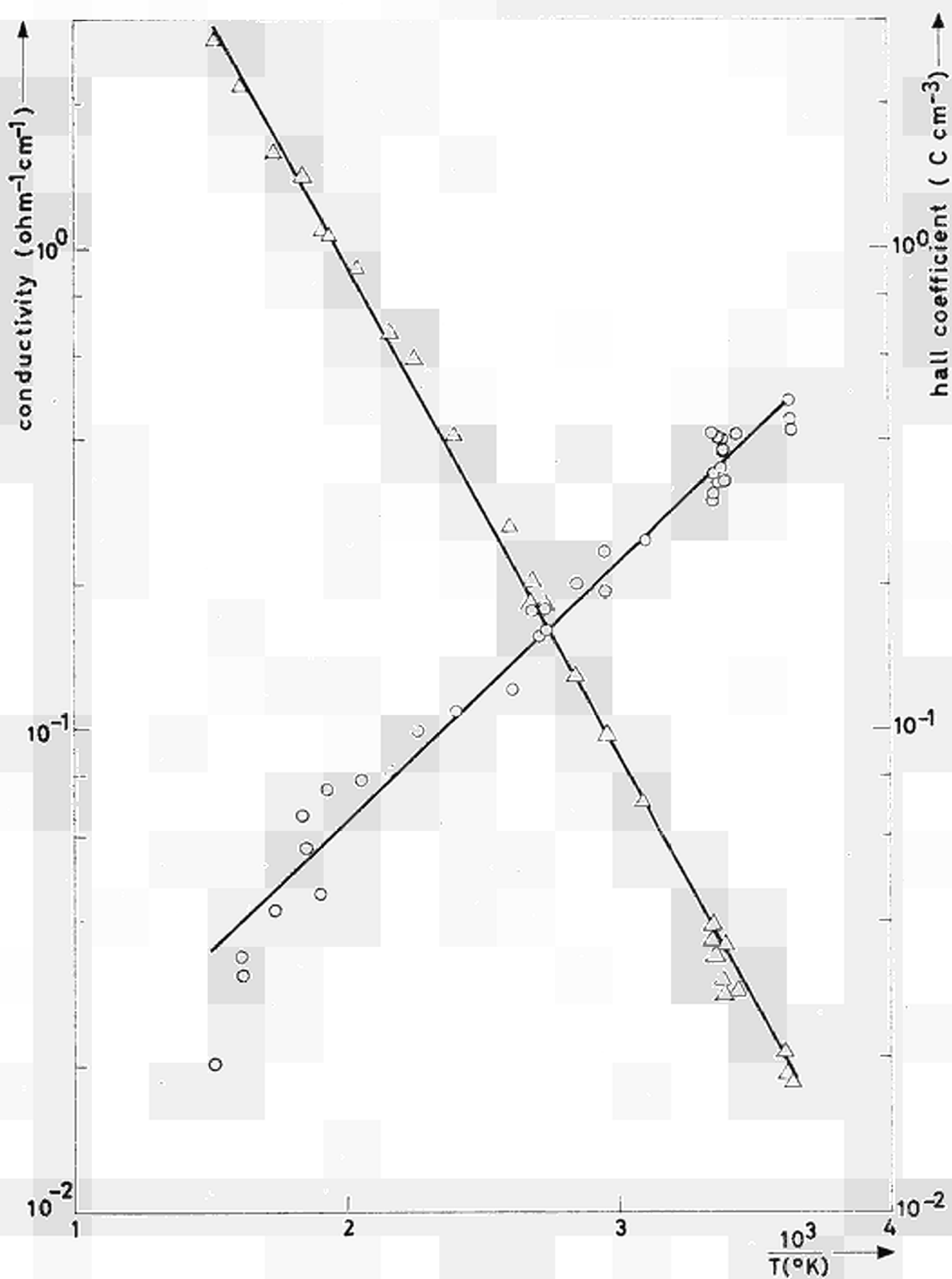


Fig. 22

Conductivity and Hall coefficient as a function of the reciprocal temperature of a UO_2 single crystal with $\delta/\text{U} \approx 2.15$

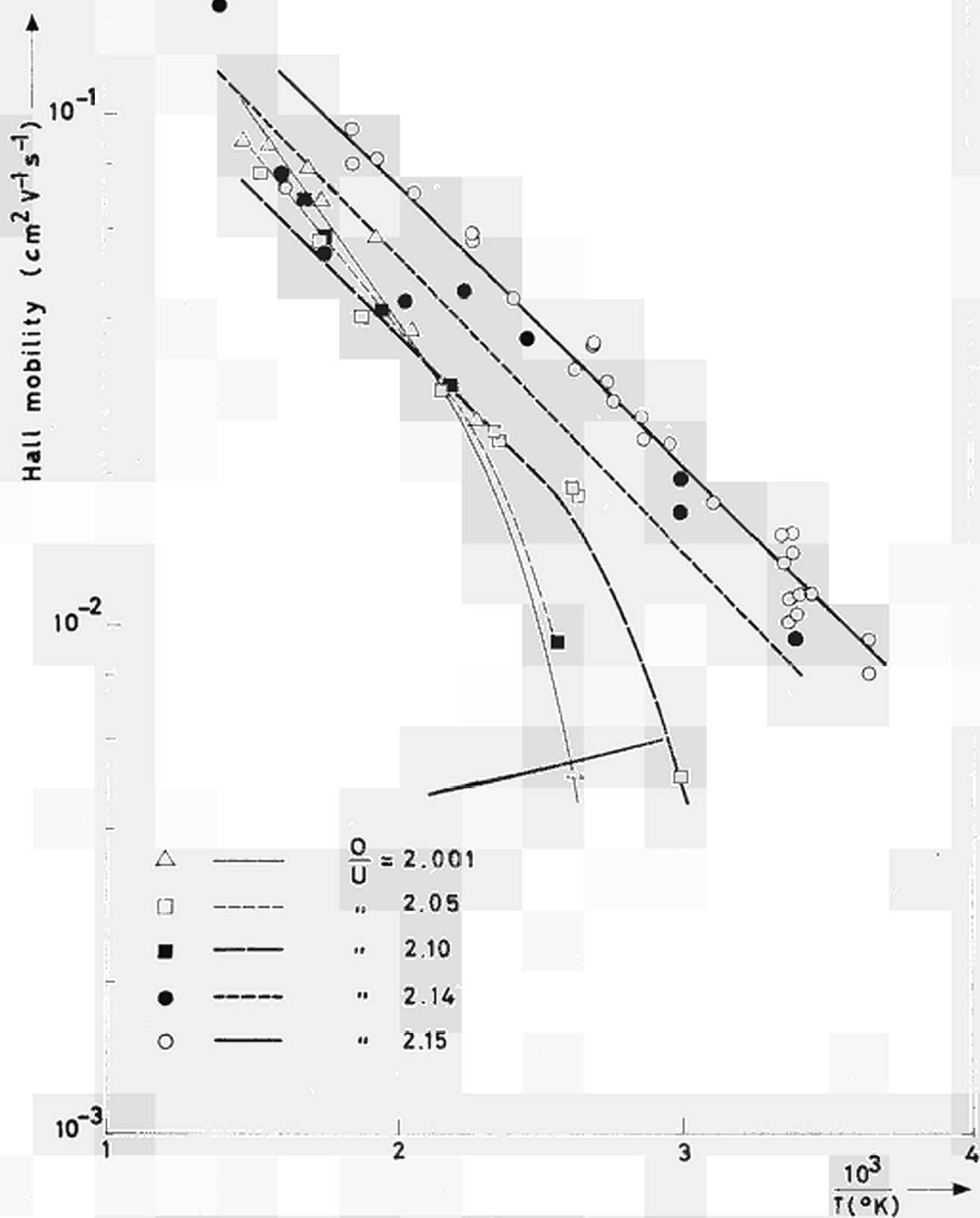


Fig. 23

Hall mobilities as a function of the reciprocal temperature of UO_2 crystals with O/U ratios varying between 2.05 and 2.15

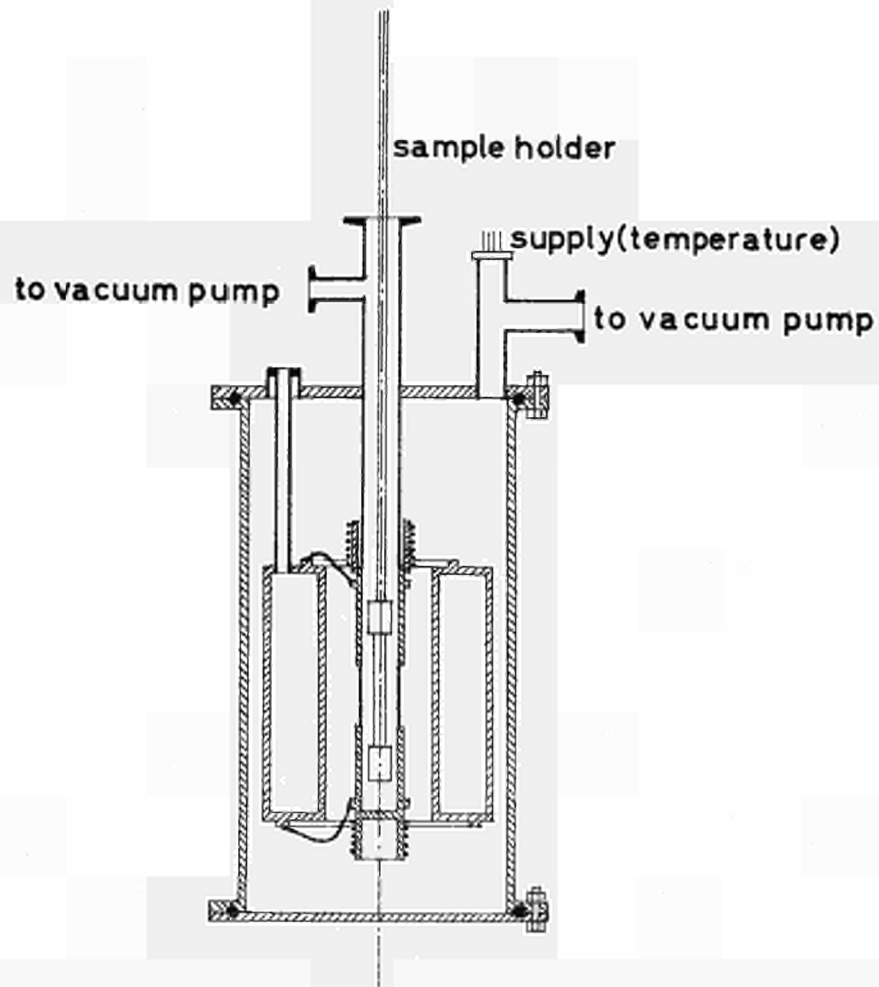


Fig. 24

Schematic drawing of the cryostat used for measurements of thermoelectric power and electrical conductivity

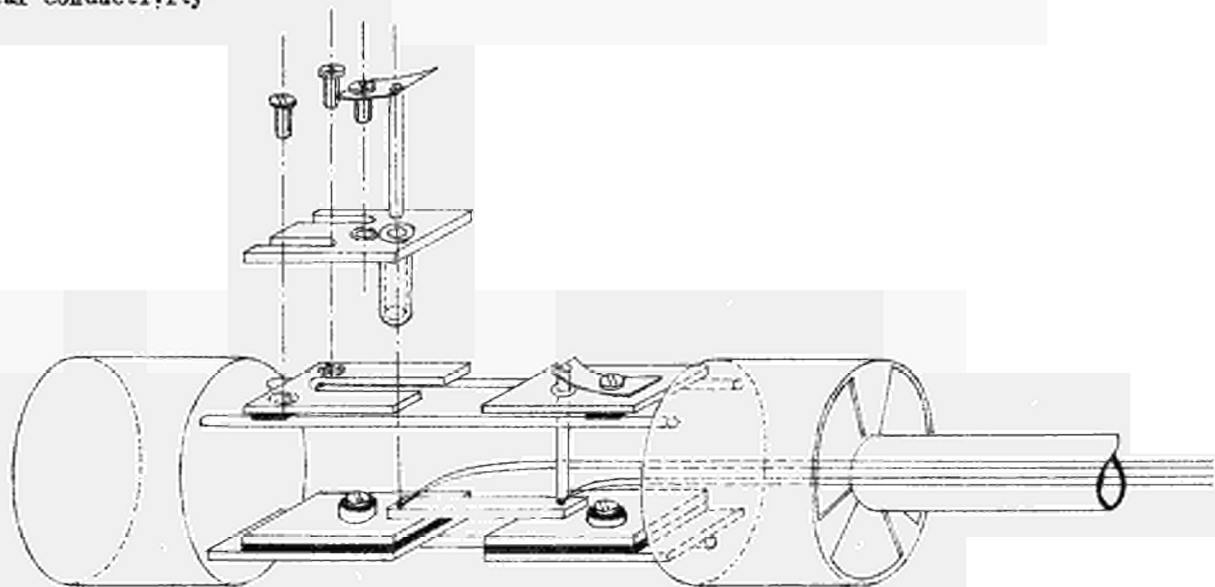


Fig. 45

Sample holder for measurement of thermoelectric power and electrical conductivity

Fig. 26

Switch system used for measurement of thermoelectric power and electrical conductivity

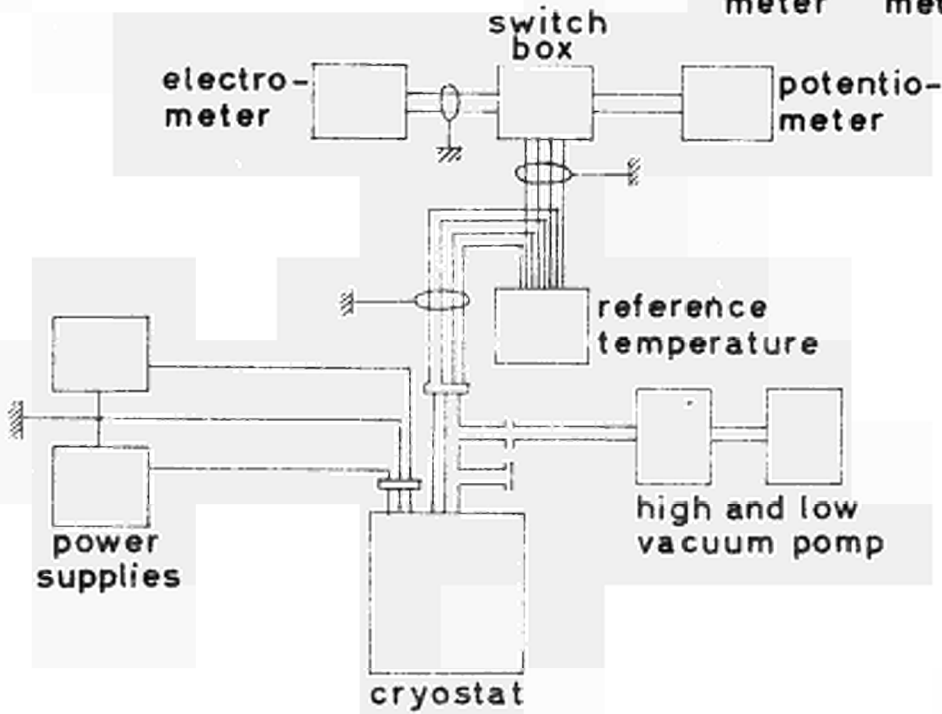
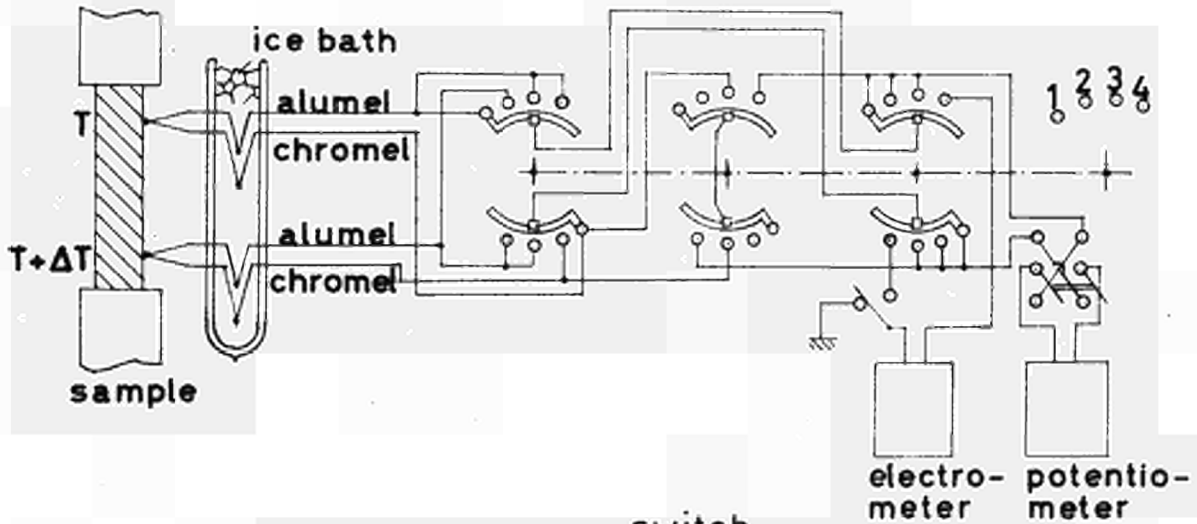


Fig. 27

General view of the apparatus for measurements of thermoelectric power and electrical conductivity

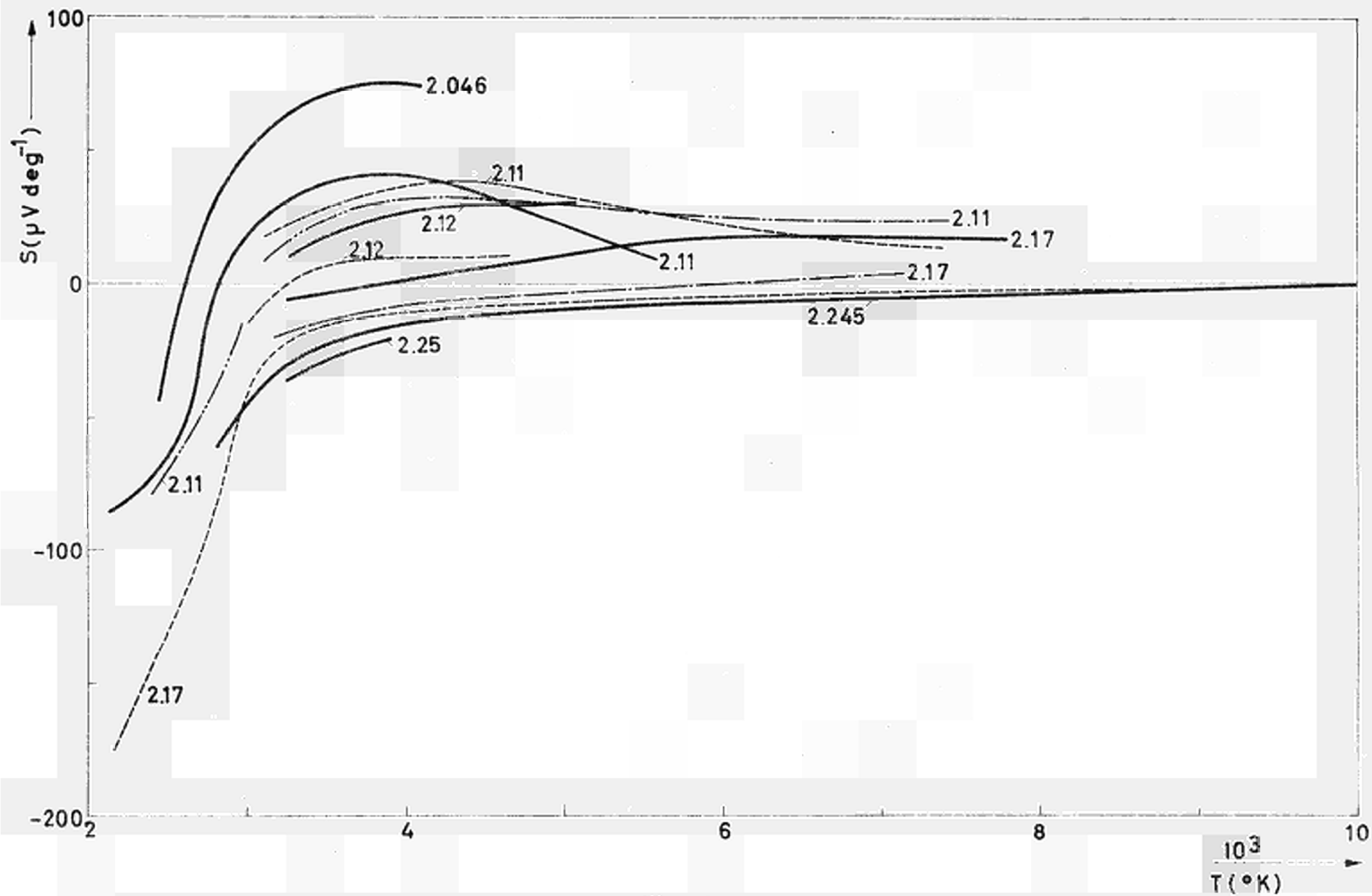


Fig. 28

Thermoelectric power as a function of the reciprocal temperature for oxidized UO_2 single crystals ($2.046 < 0/U < 2.25$)

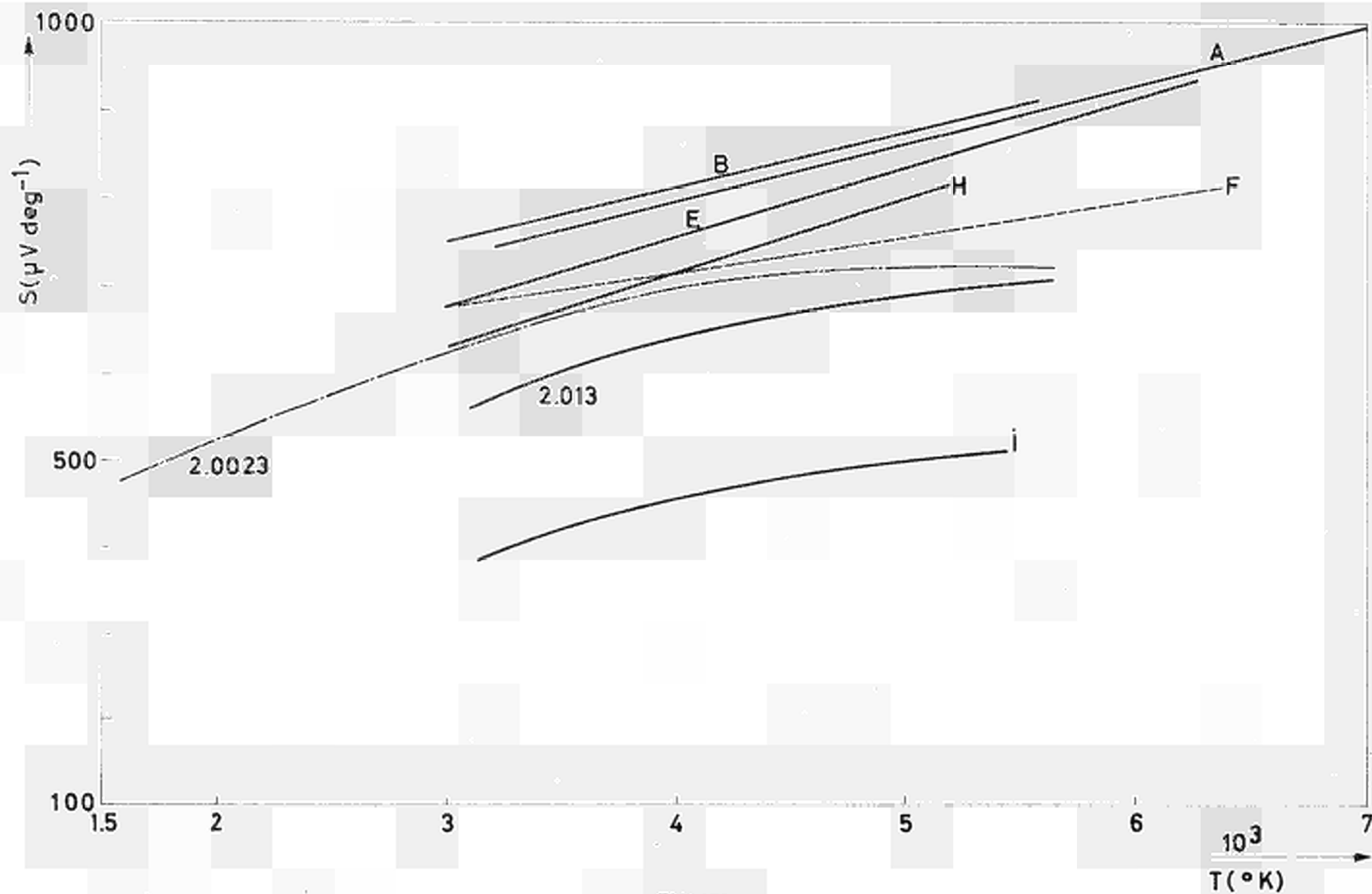


Fig. 29

Thermoelectric power as a function of reciprocal temperature for slightly oxidized UO_2 single crystals ($0.001 < x < 0.013$)

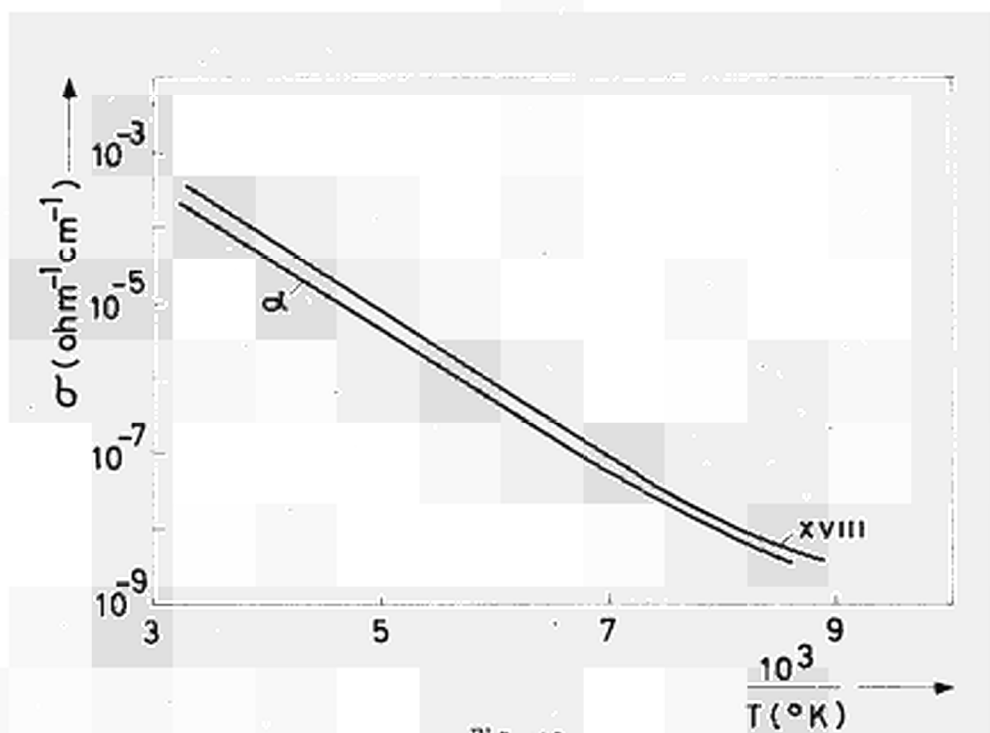


Fig. 30

Electrical conductivity of two as-grown crystals ($O/U \approx 2.005$) versus reciprocal temperature

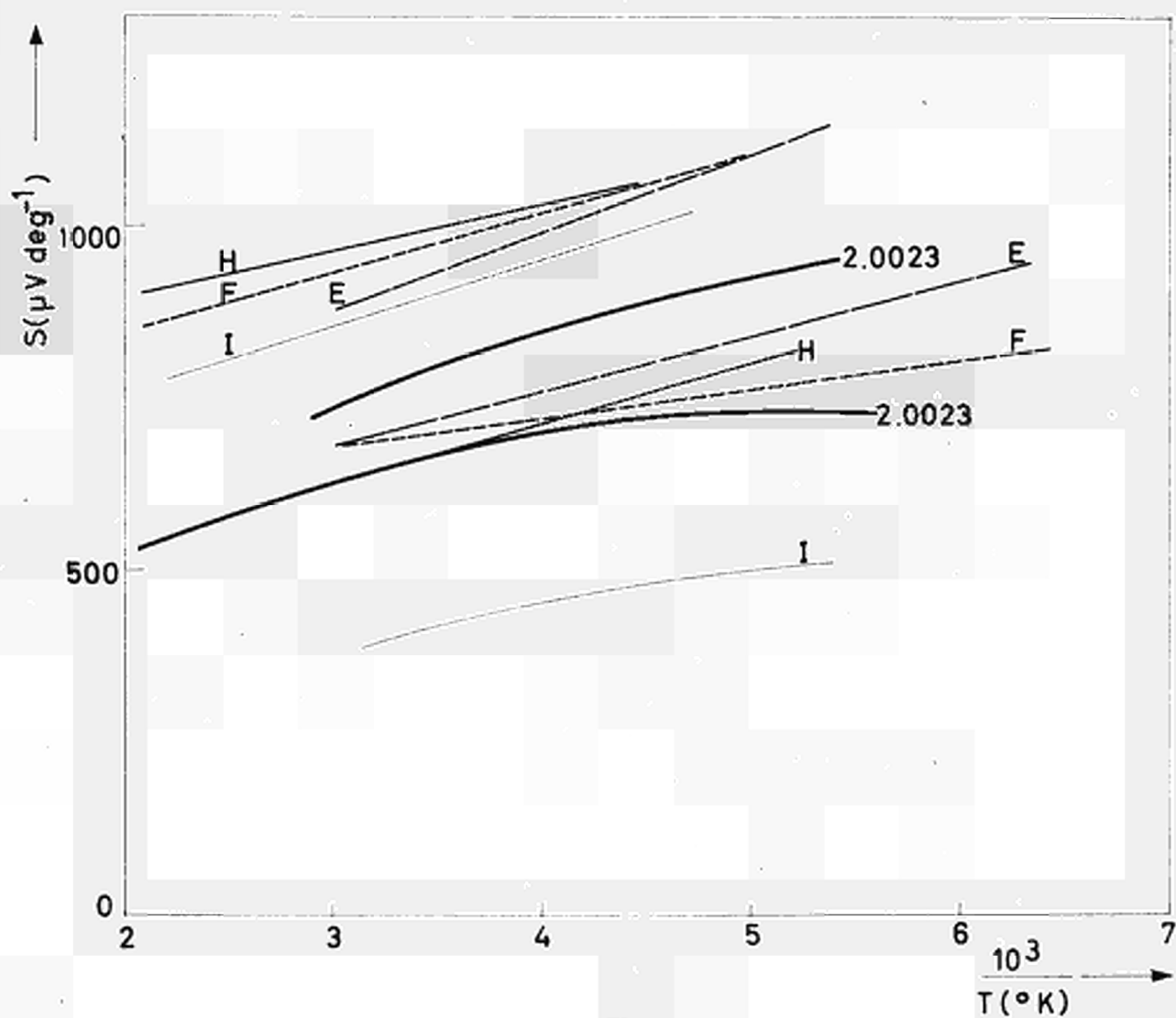


Fig. 31

Thermoelectric power as a function of reciprocal temperature for UO_2 crystals before and after reduction

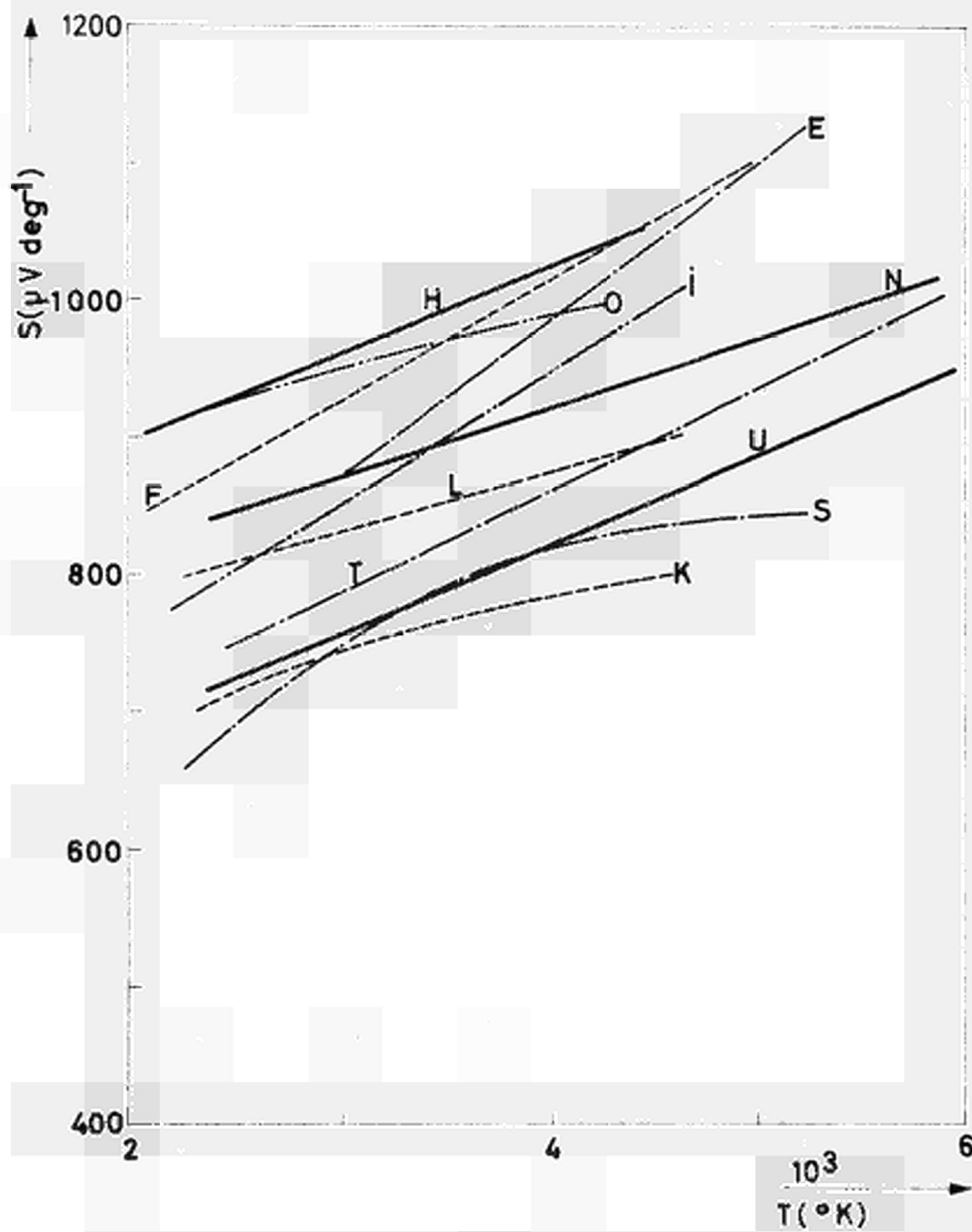


Fig. 34

Thermoelectric power of nearly stoichiometric UO_2 single crystals ($0.001 < x$) versus reciprocal temperature

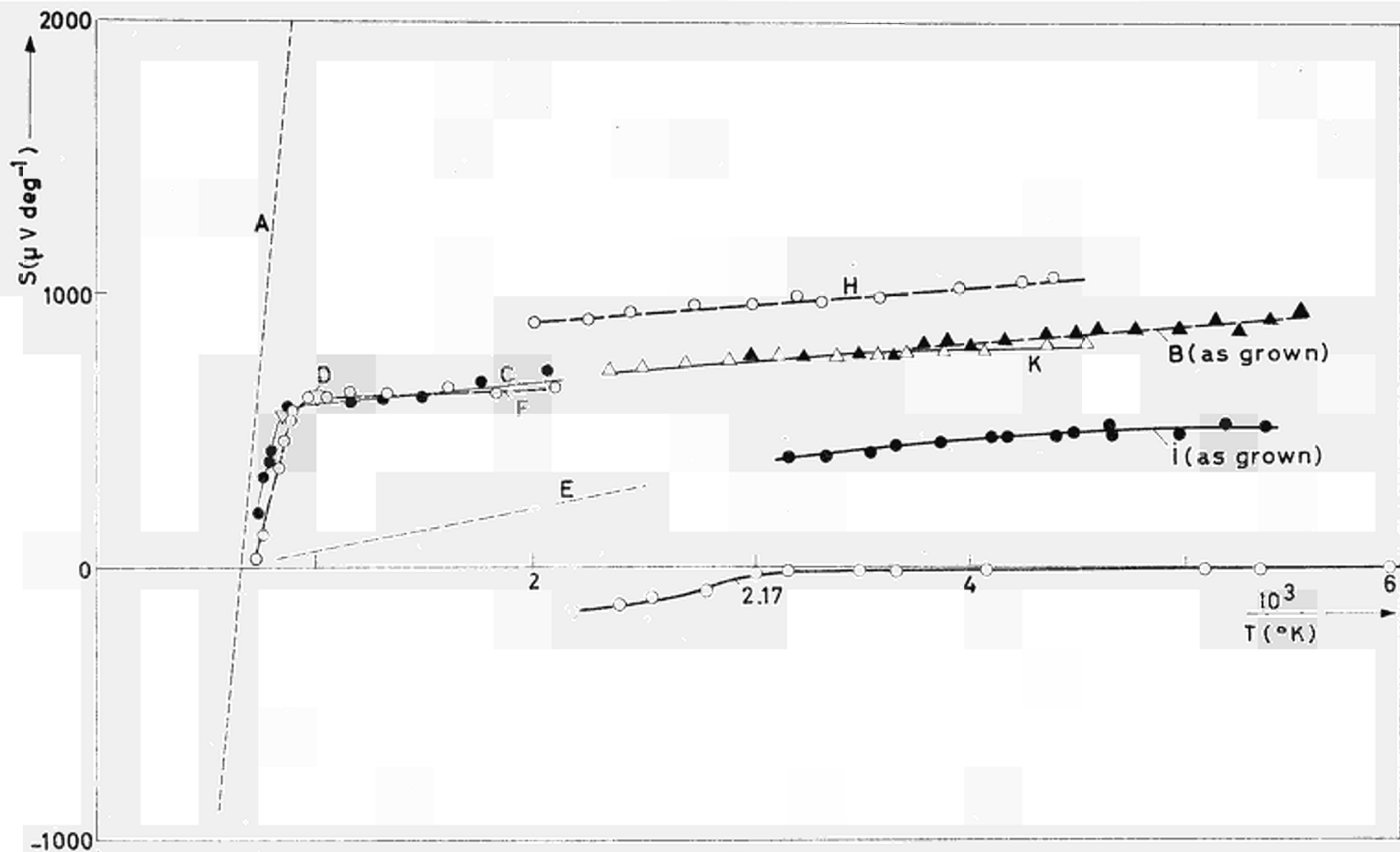


Fig. 33

Thermoelectric power measurements on UO_2 as reported by different authors: Bates (curve A), Wolfe (curves F and C), Aronson et al. (curve D), Karkhanavala et al. (curve B), present work (curves E, B, K and I)

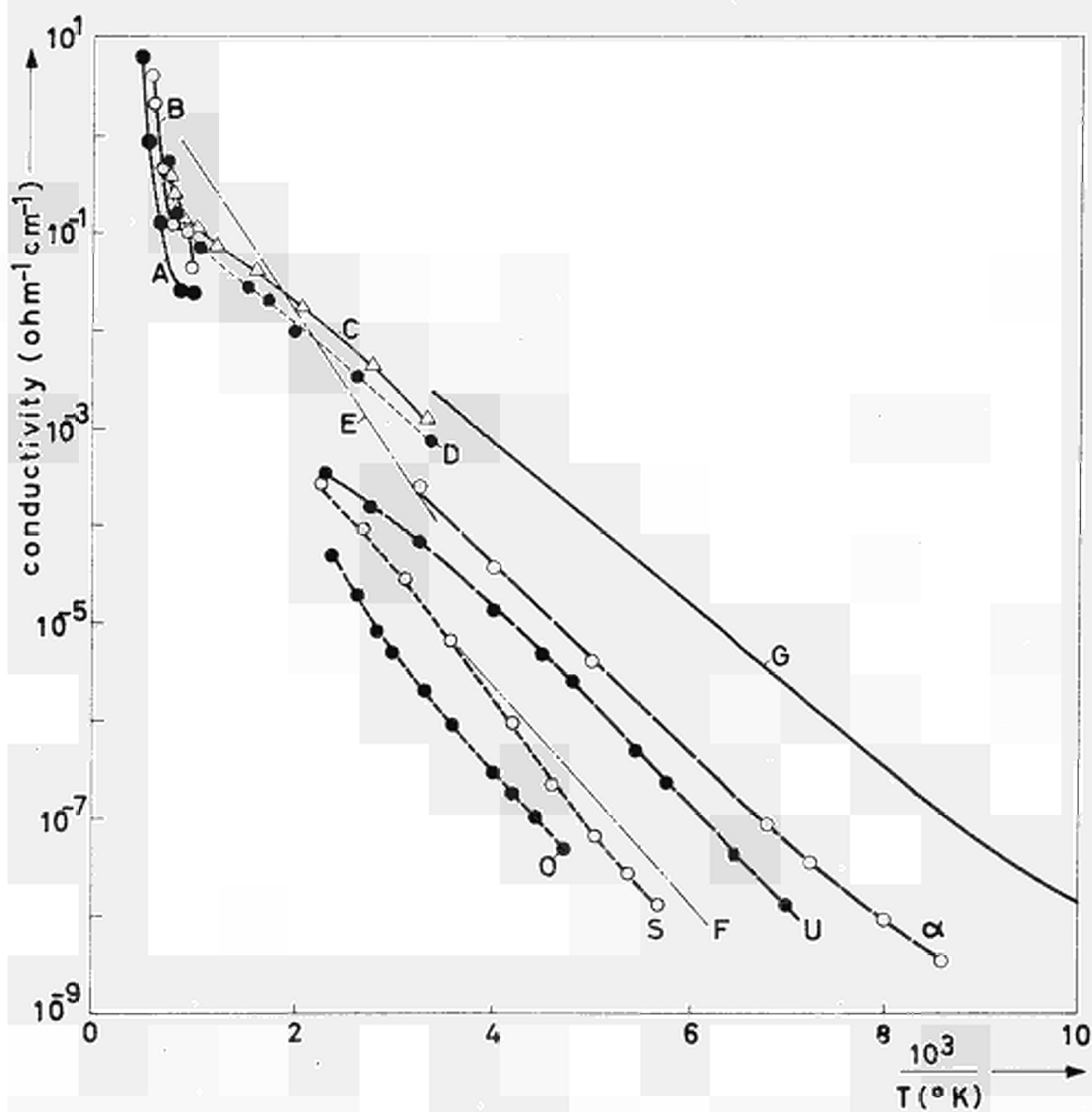


Fig. 34

Electrical conductivity measurements on UO_2 as reported by different authors : Bates (curves A and B), Wolfe (curves C and D), Karkhanavala et al. (curve E), present work (curves O, S, F, U, α and G)

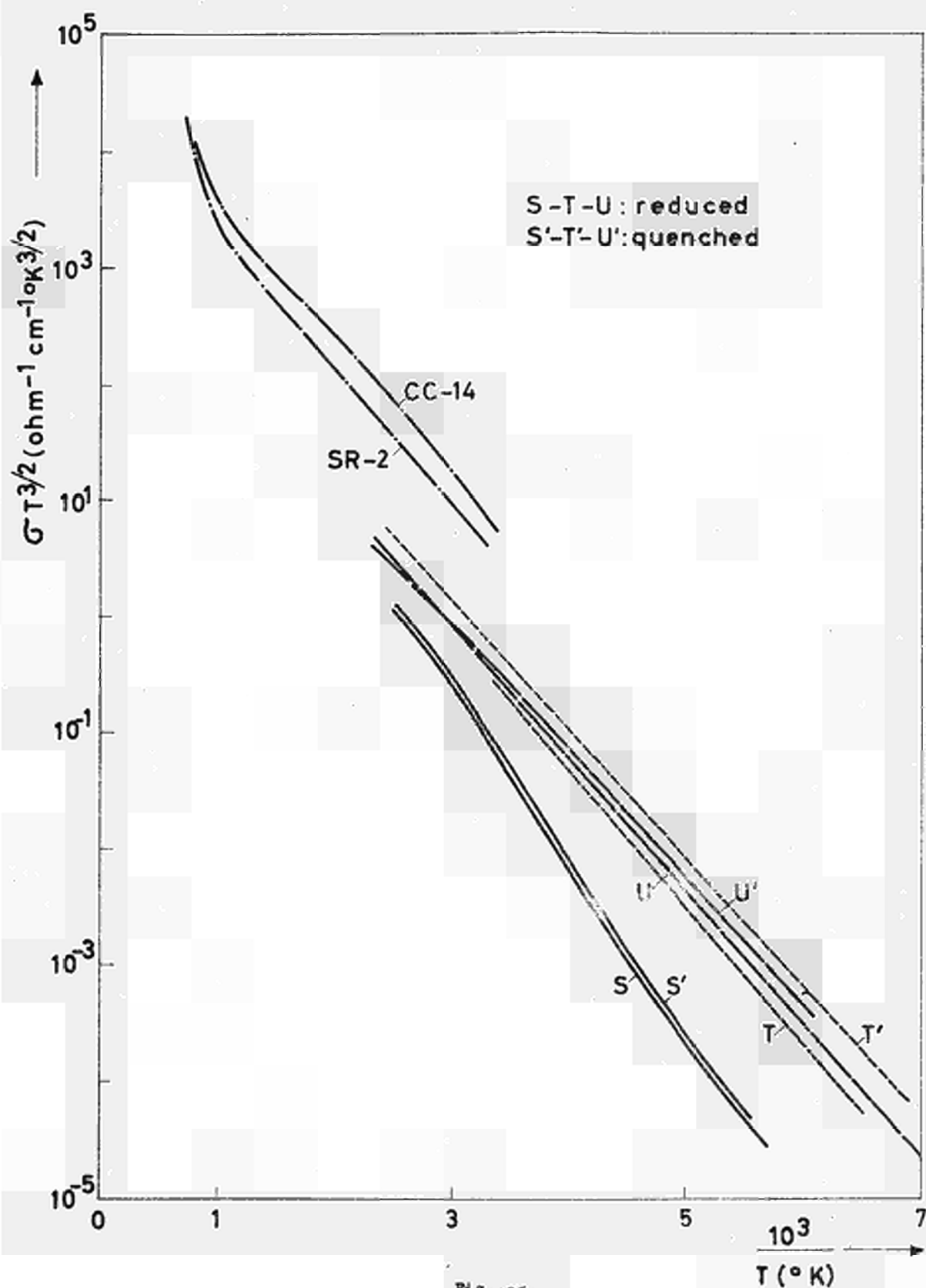


Fig. 35

Electrical conductivity of different specimens in a diagram $\log \sigma T^{3/2}$ versus reciprocal temperature - Curves SR-2 and CC-14 correspond to measurements made by Wolfe

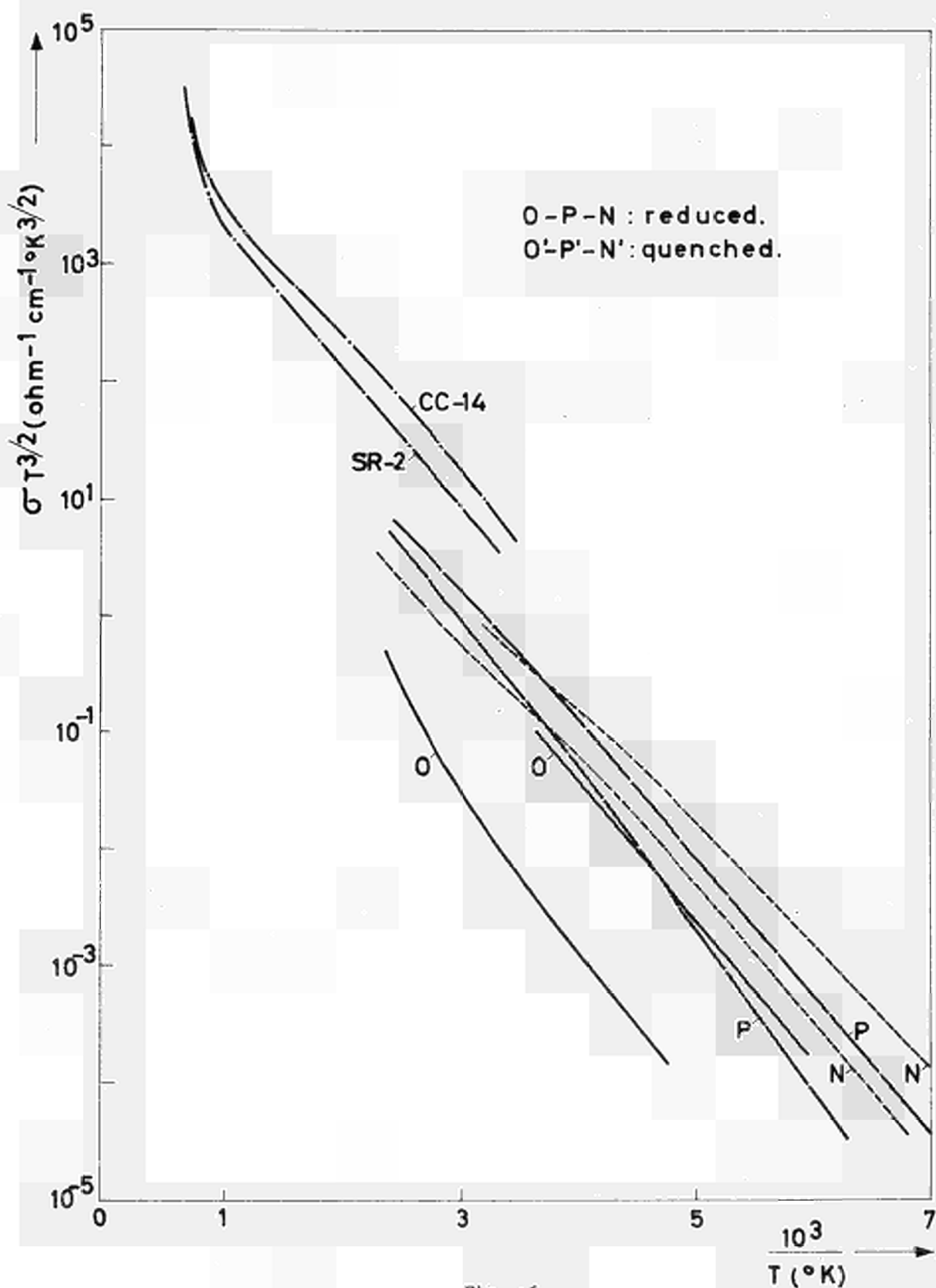


Fig. 36

Electrical conductivity of different specimens (other than Fig. 35) in a diagram $\log \sigma T^{3/2}$ versus reciprocal temperature - Curves SR-2 and CC-14 correspond to measurements made by Wolfe

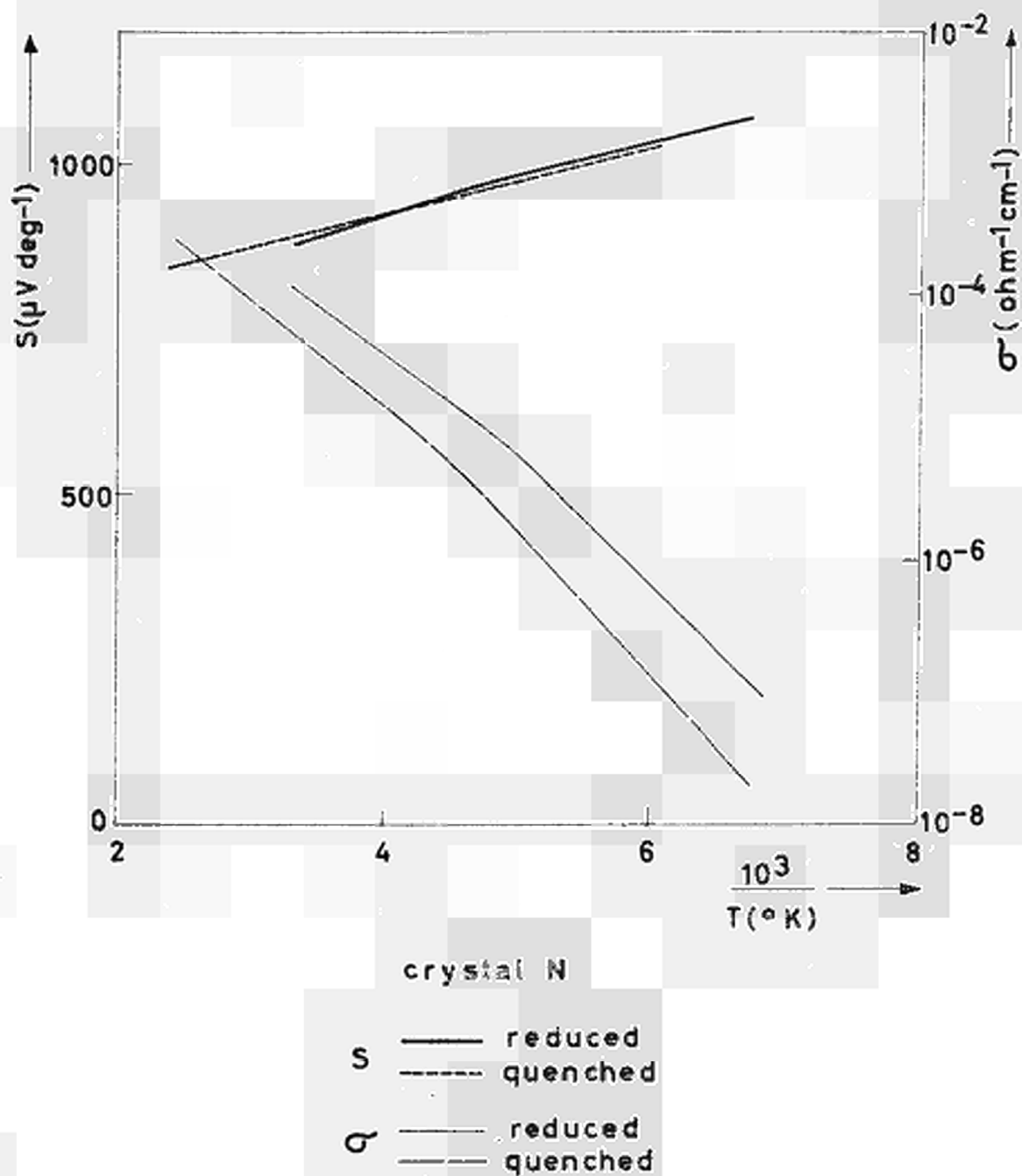


FIG. 37

Thermoelectric power and conductivity of a nearly stoichiometric UO_2 crystal (sample N) before and after quenching

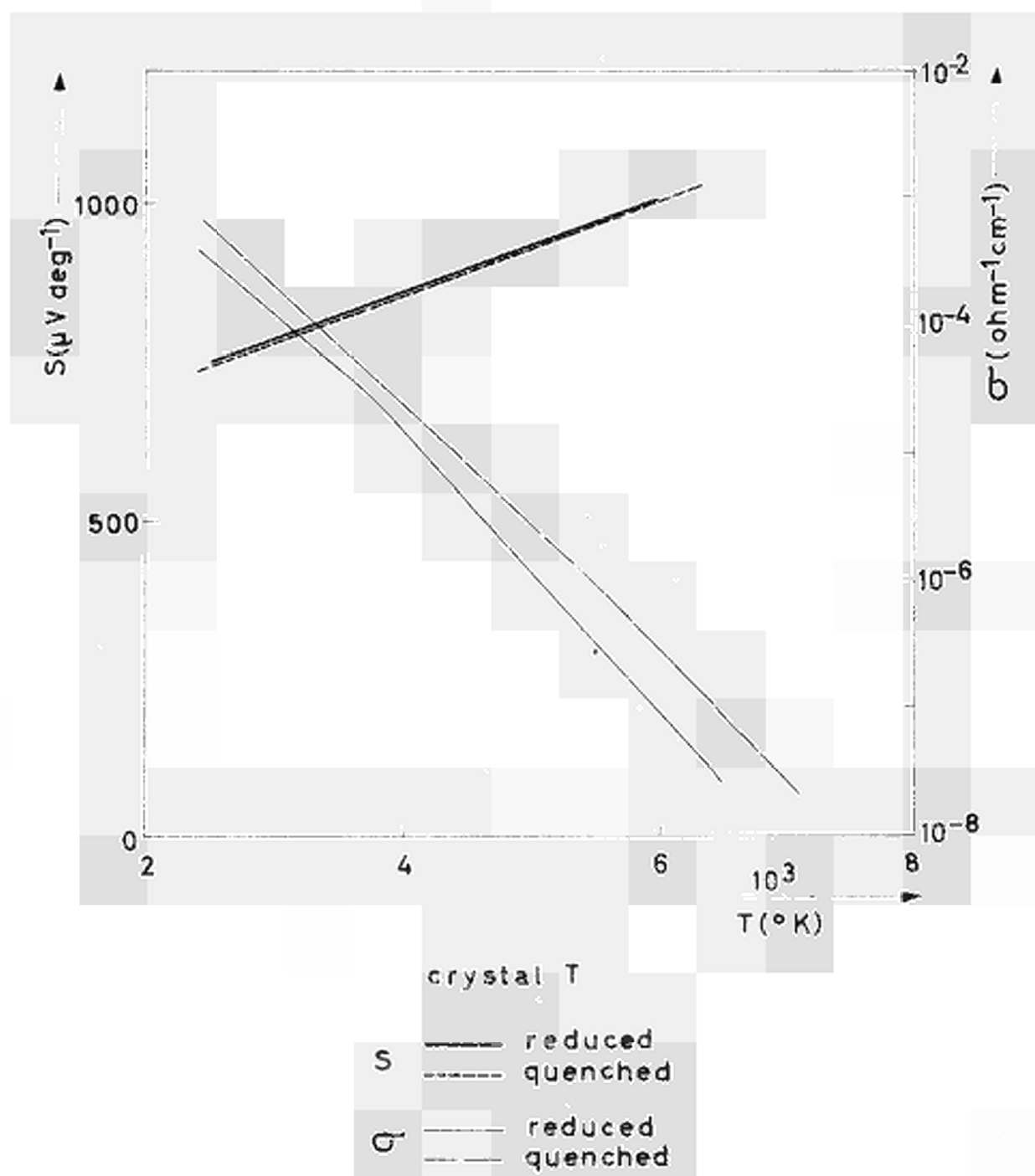


Fig. 36

Thermoelectric power and conductivity of a nearly stoichiometric SO_3 crystal (sample 2) before and after quenching

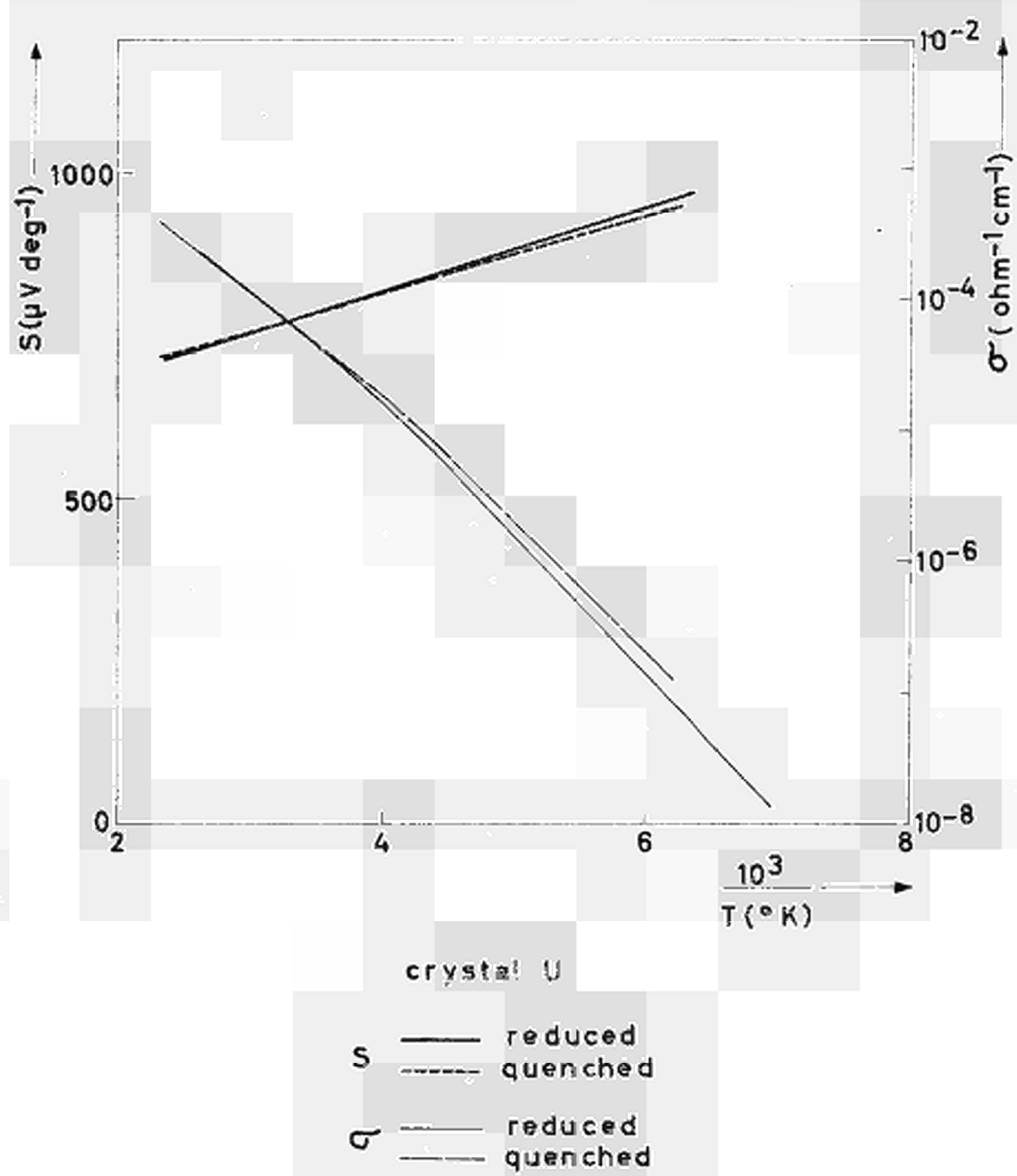


Fig. 39

Thermoelectric power and conductivity of a nearly stoichiometric UO_2 crystal (sample U) before and after quenching

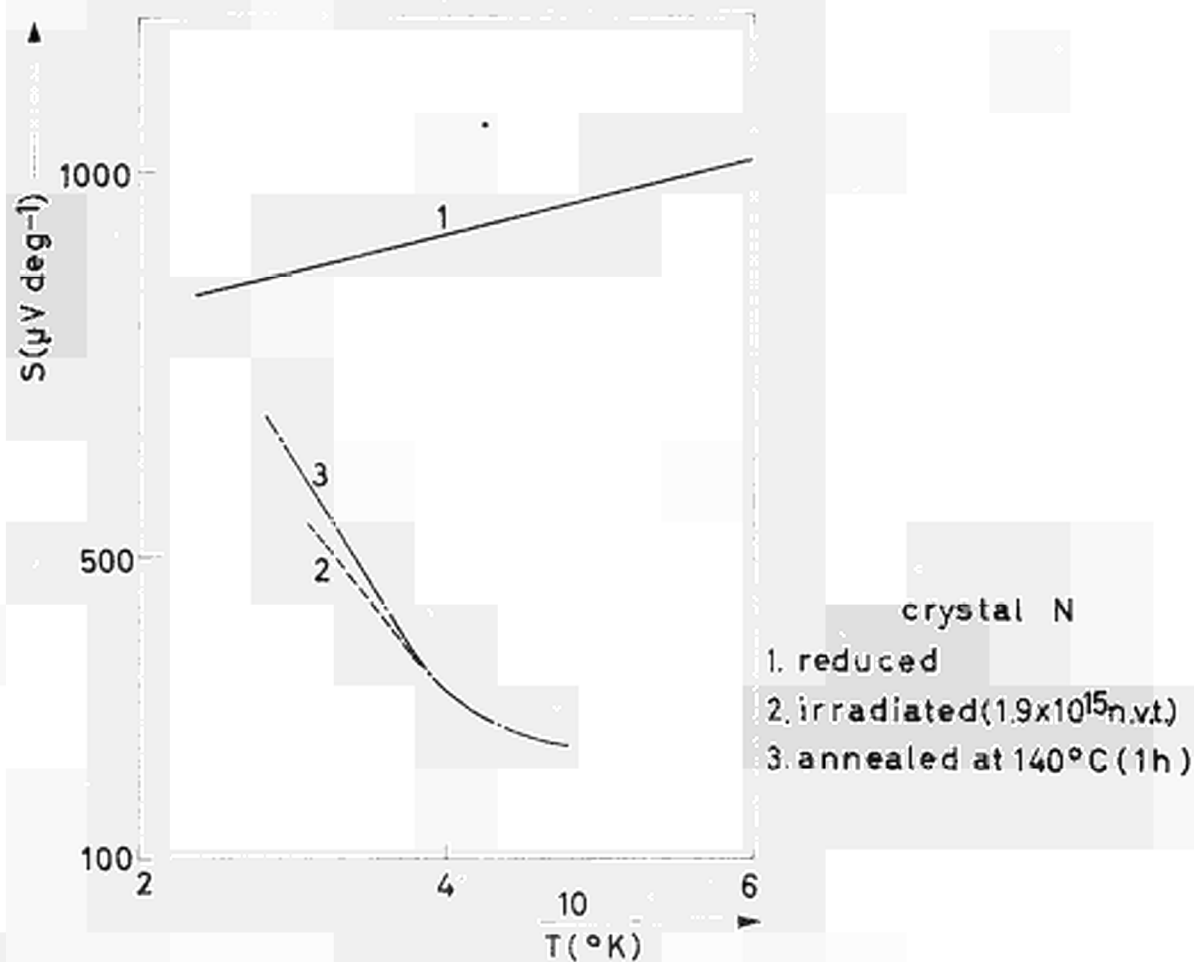


Fig. 40

Thermoelectric power as a function of reciprocal temperature for a nearly stoichiometric DO_2 crystal before and after irradiation

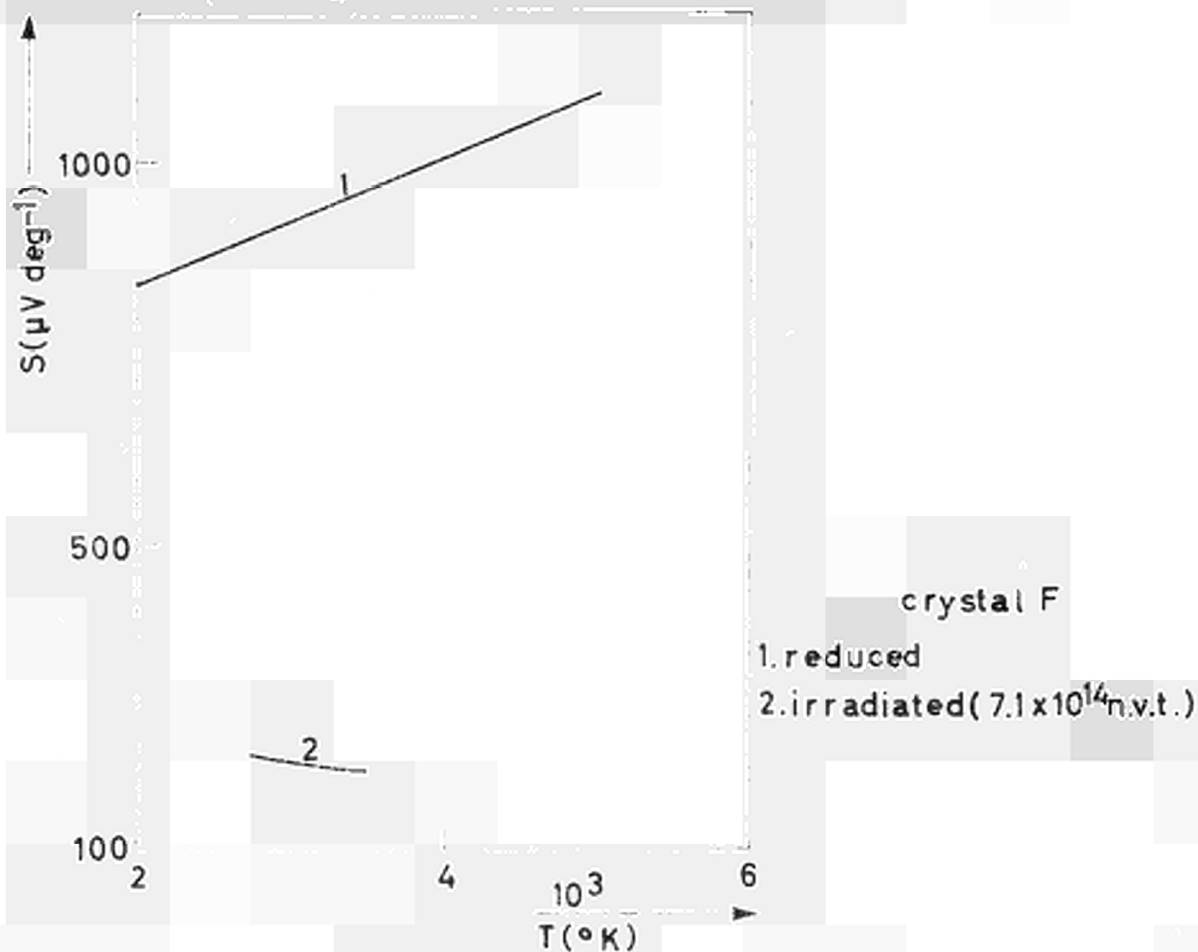


Fig. 41

Thermoelectric power as a function of reciprocal temperature for a nearly stoichiometric CO_2 crystal before and after irradiation

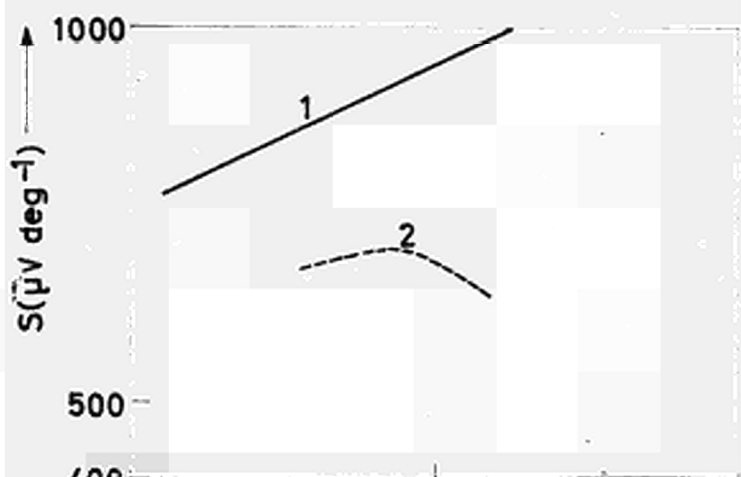


Fig. 42

crystal i

- 1. reduced
- 2. irradiated (8.5×10^{14} n.v.t.)

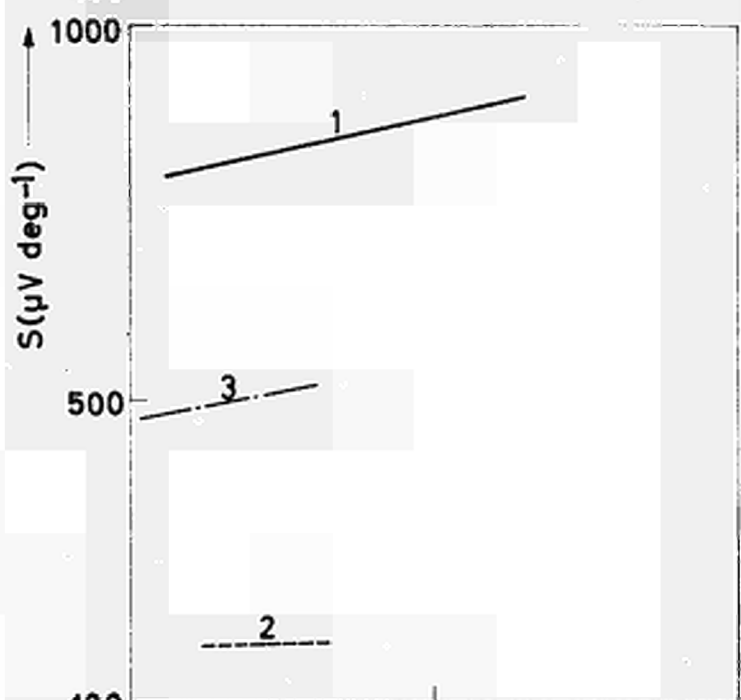


Fig. 43

crystal L

- 1. reduced
- 2. irradiated (10^{16} n.v.t.)
- 3. annealed at 300°C (1h)

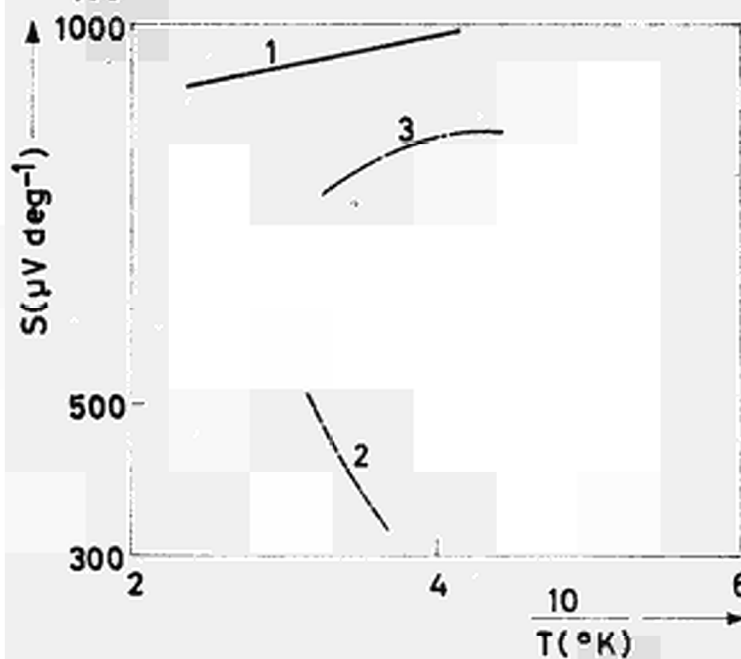


Fig. 44

crystal O

- 1 reduced
- 2 irradiated (1.5×10^{15} n.v.t.)
- 3 annealed at 350°C (1h)

Thermoelectric power as a function of reciprocal temperature for a nearly stoichiometric UO_2 crystal before and after irradiation

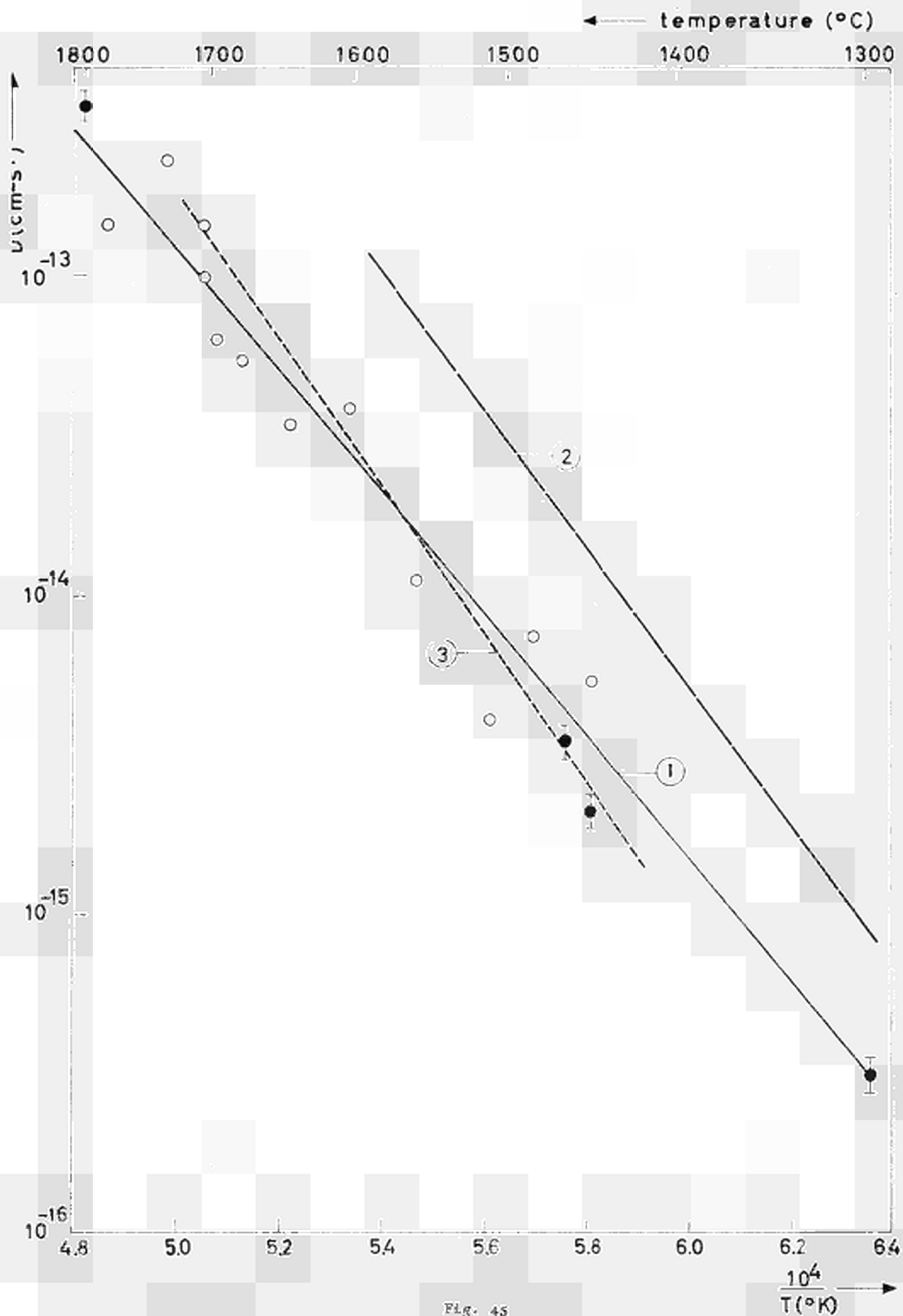


Fig. 45

Uranium self-diffusion data for UO_2 according to different authors - Curve 1 : Aushern et al. and present work ; curve 2 : Lindner et al. ; curve 3 : McManara

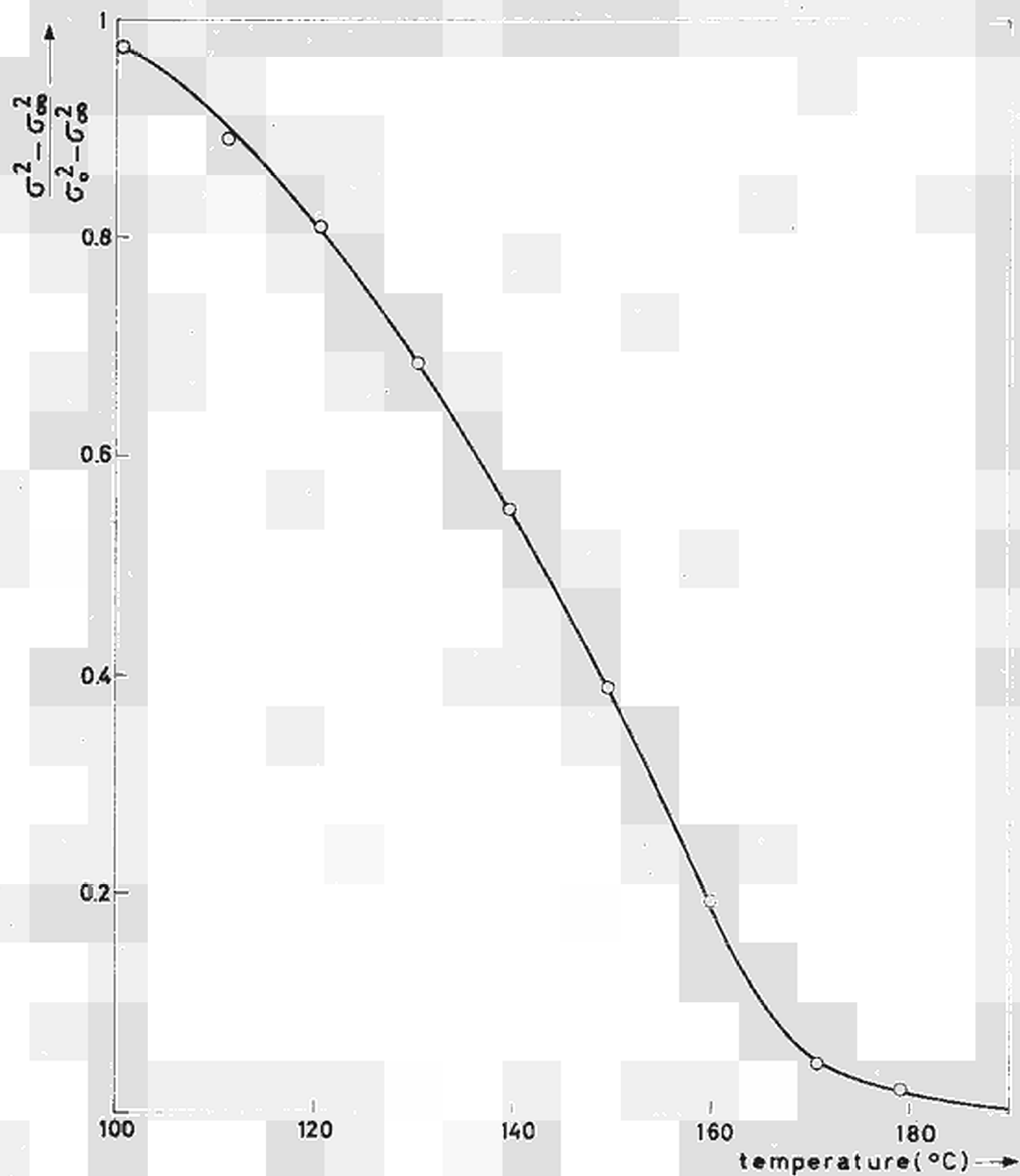


Fig. 46

Isochronal annealing of a quenched UO_{2+x} single crystal ($0/U \approx 2.005$)

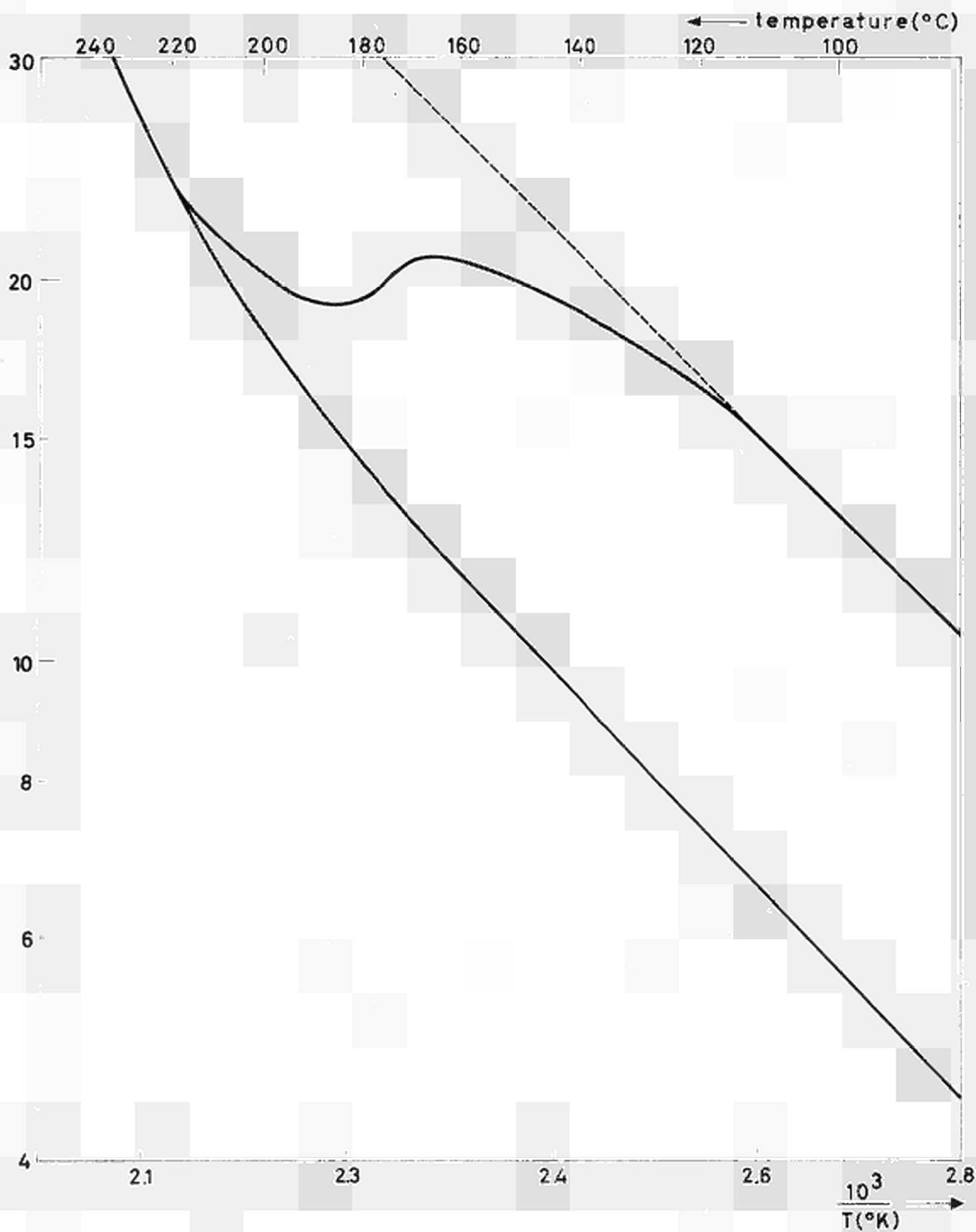


Fig. 47

Conductivity measurements during linear heating and cooling of a quenched $UC_{2,x}$ single crystal.

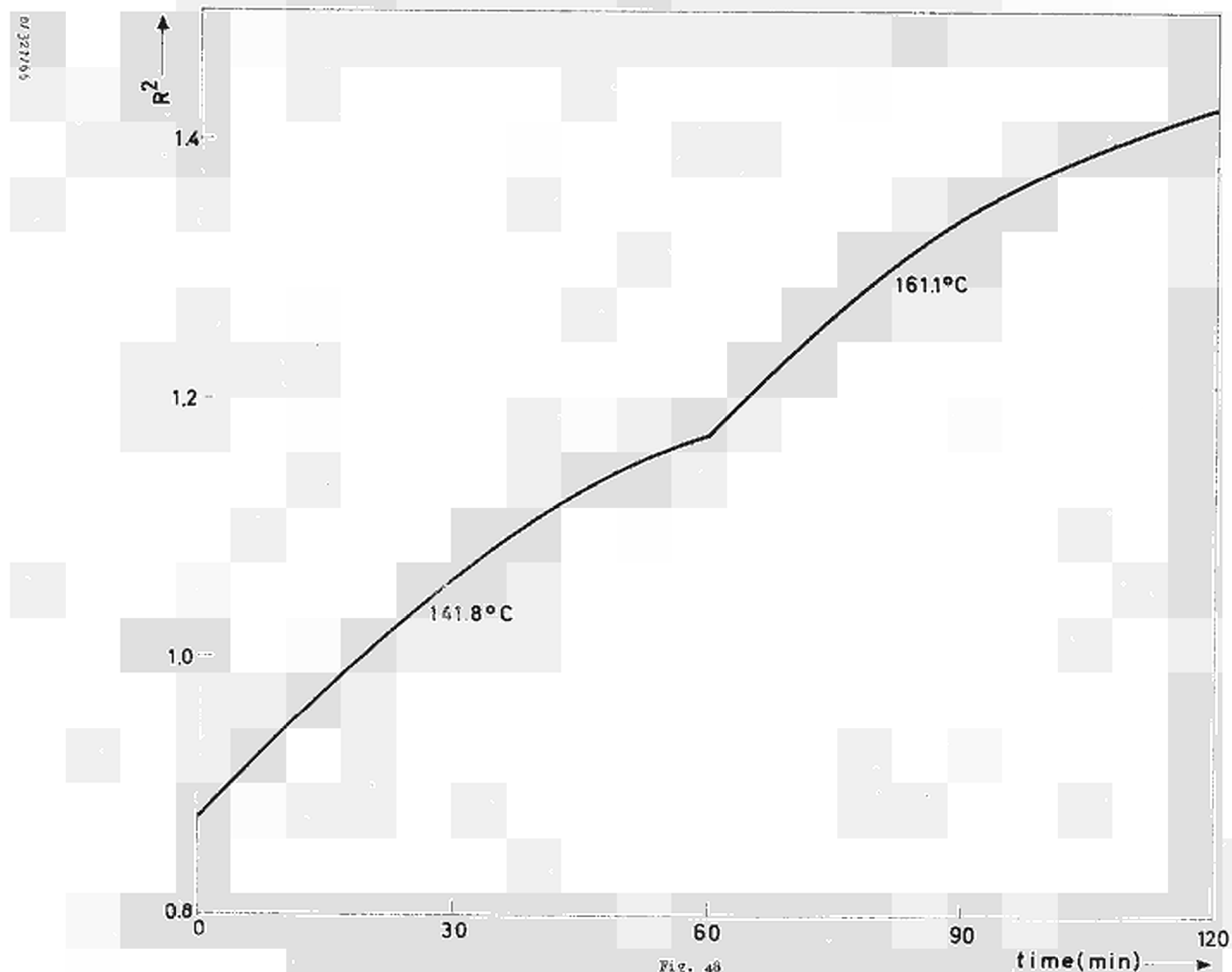


Fig. 48

Two successive isothermal annealing curves measured on a quenched UO_{2+x} crystal

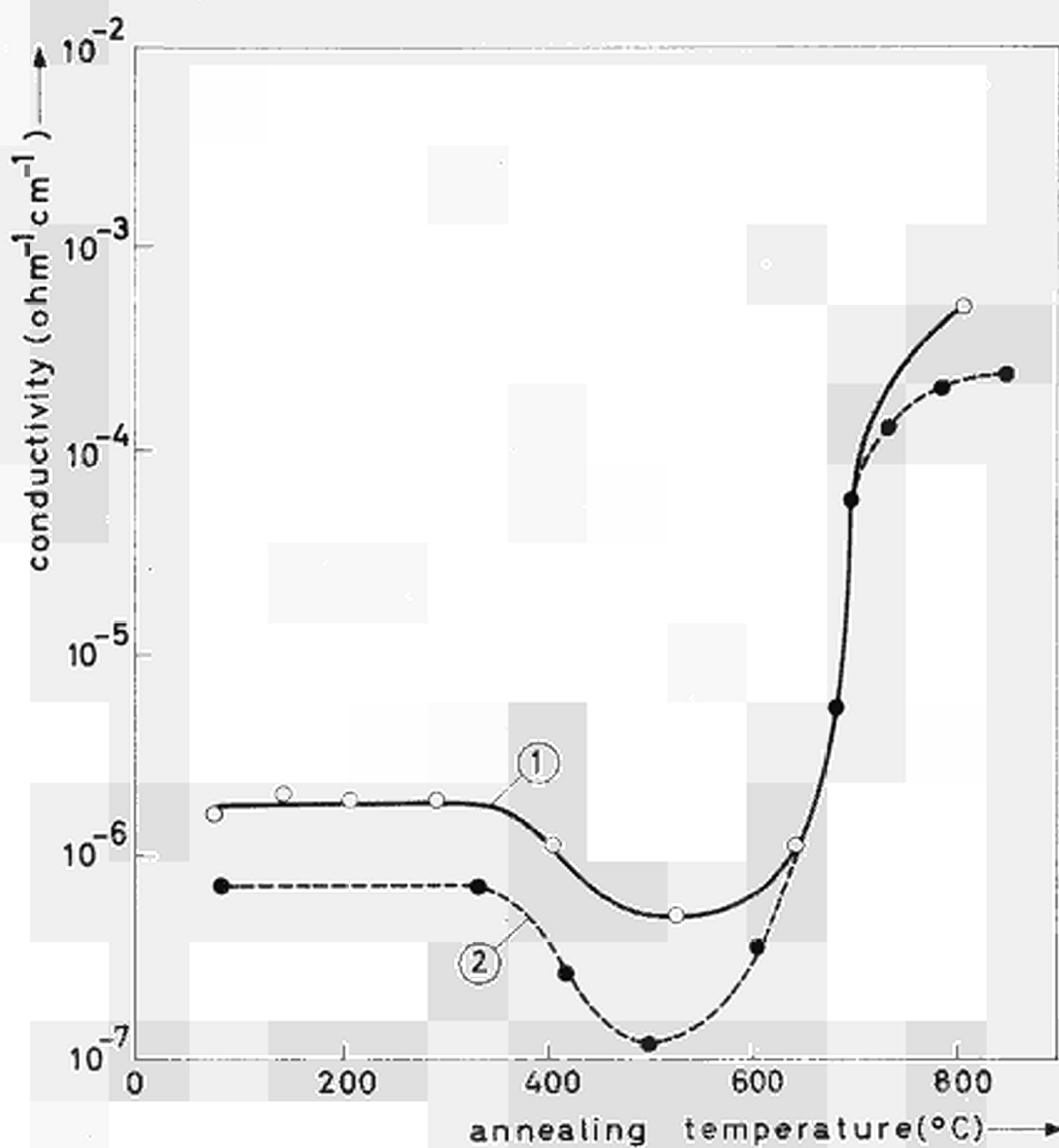


Fig. 49

Recovery of the electrical conductivity due to annealing of UO_2 previously irradiated with thermal neutrons; the conductivity values before irradiation are 1.4×10^{-3} (curve 1) and 1.2×10^{-3} $ohm^{-1}cm^{-1}$ respectively

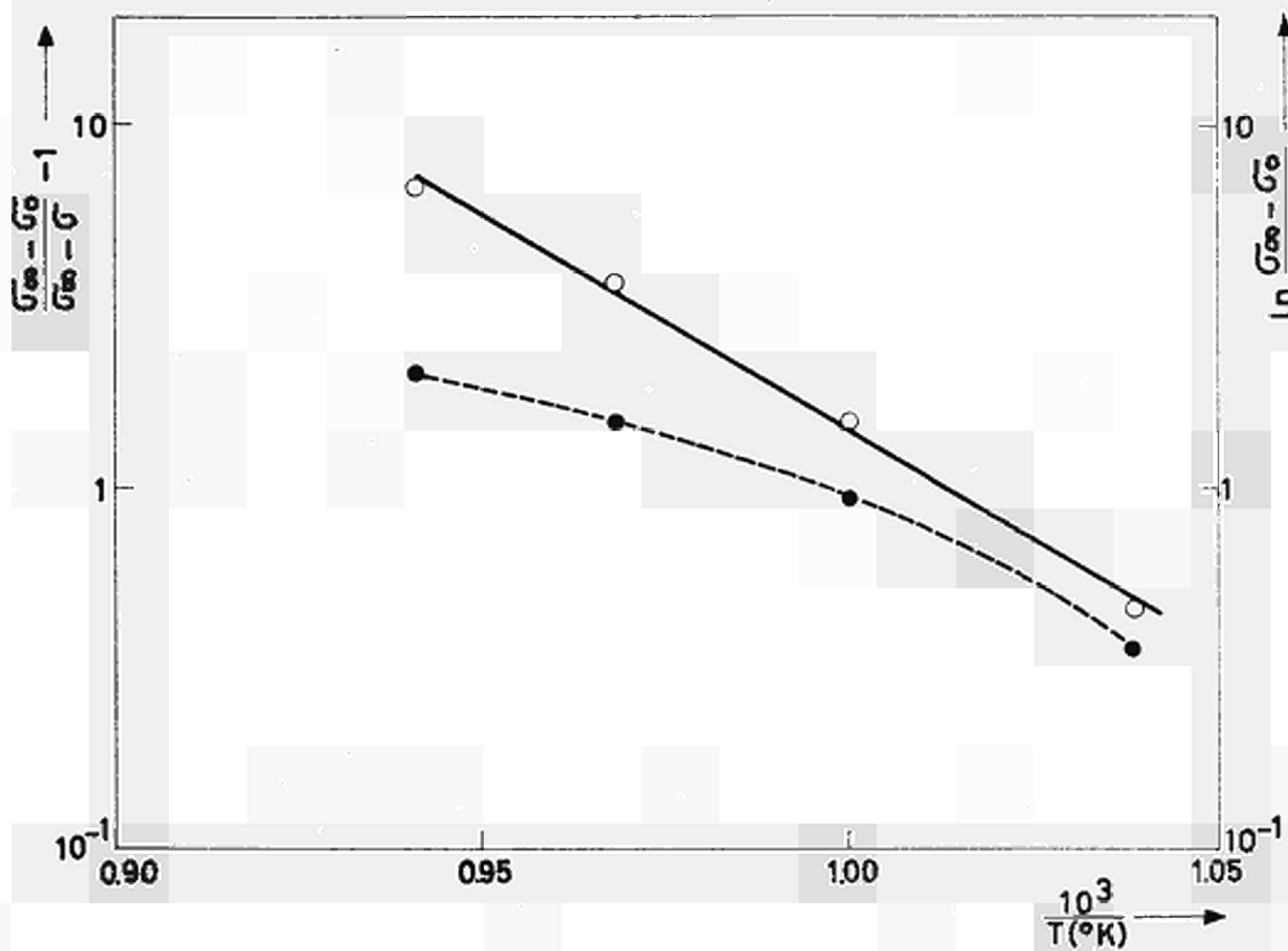


Fig. 50

Analysis following the method of Baiarin and Zetzsche of the pulse annealing data of UO_2 previously irradiated with thermal neutrons - The dotted and full lines correspond to first and second order kinetics respectively

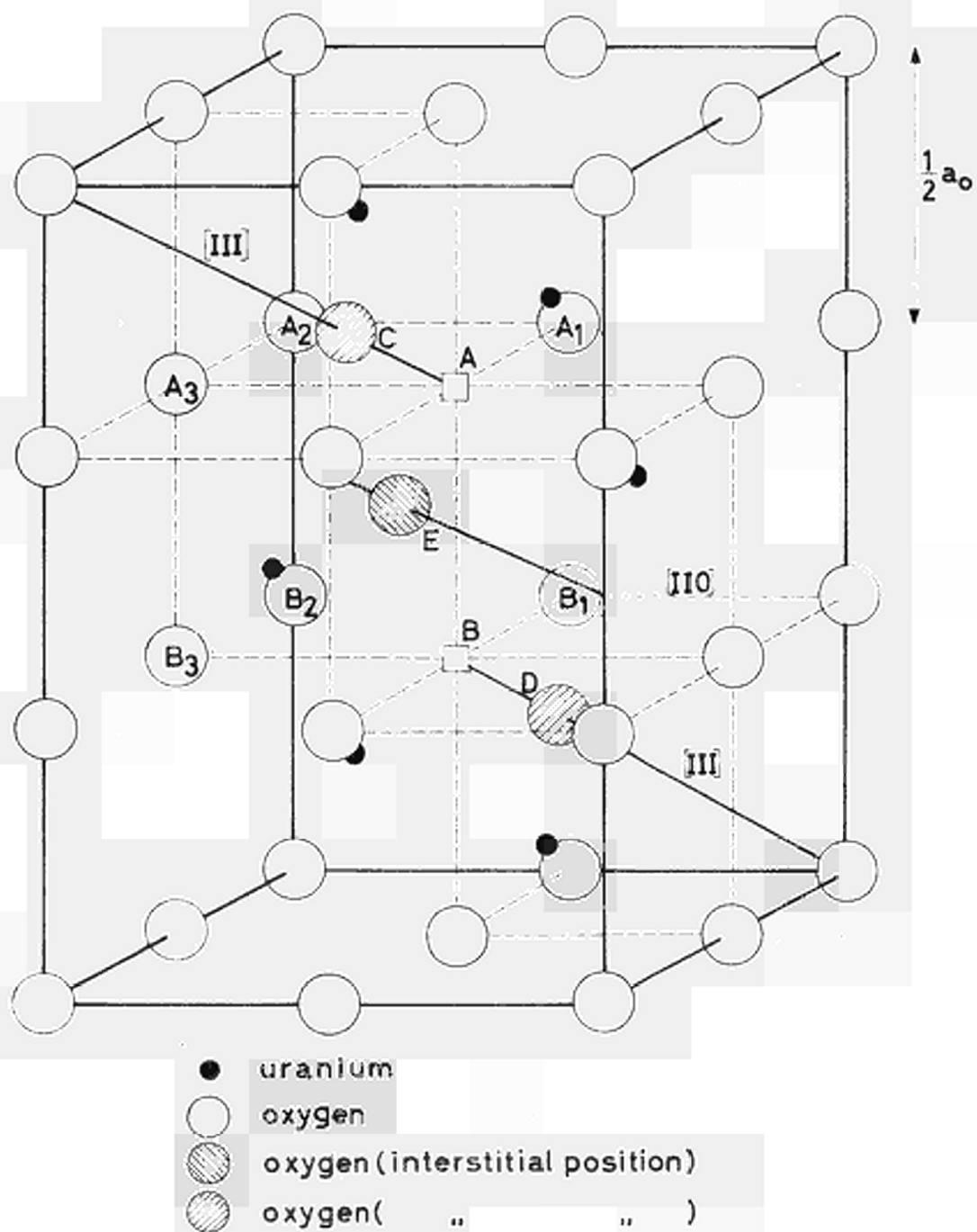


Fig. 51

Model for an oxygen interstitial in UO_{2+x} (according to Willis)



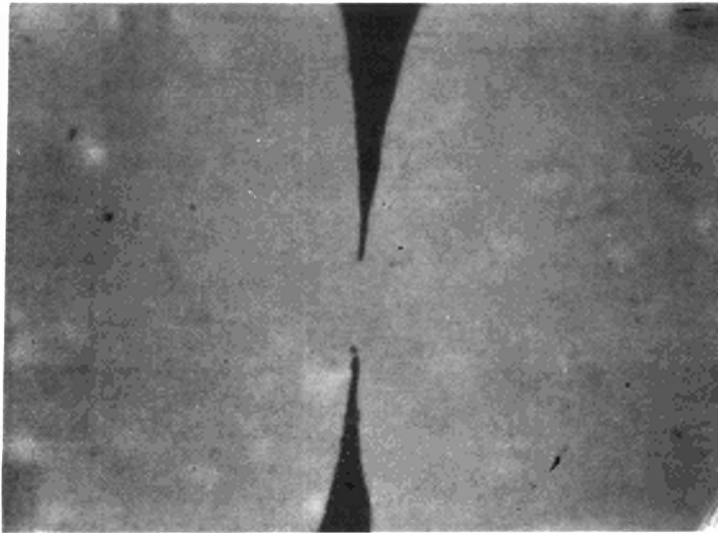


Fig. 53

Neck between two spheres sintered at 1700°C for 3 h
($\times 1500$)

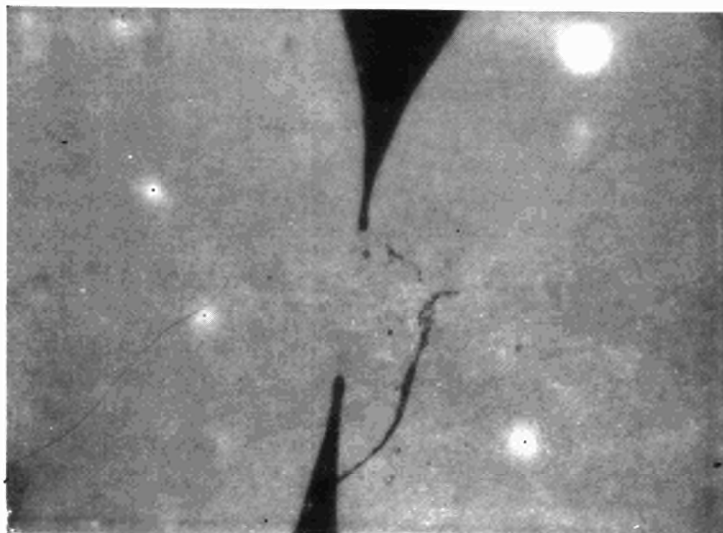


Fig. 54

Neck between two spheres sintered at 1700°C for 7 h
($\times 1500$)

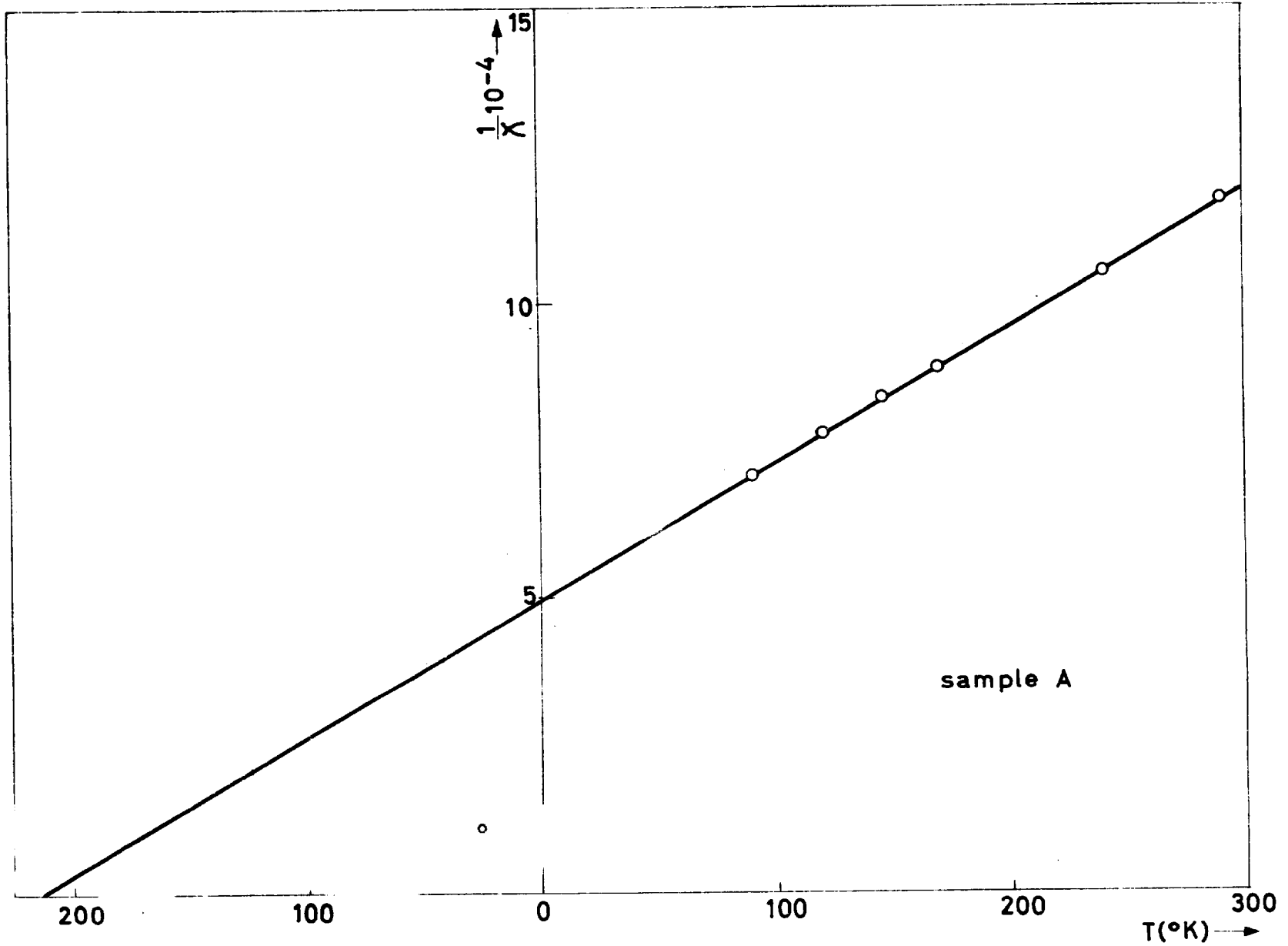


Fig. 55

Reciprocal of the magnetic susceptibility as a function of the absolute temperature

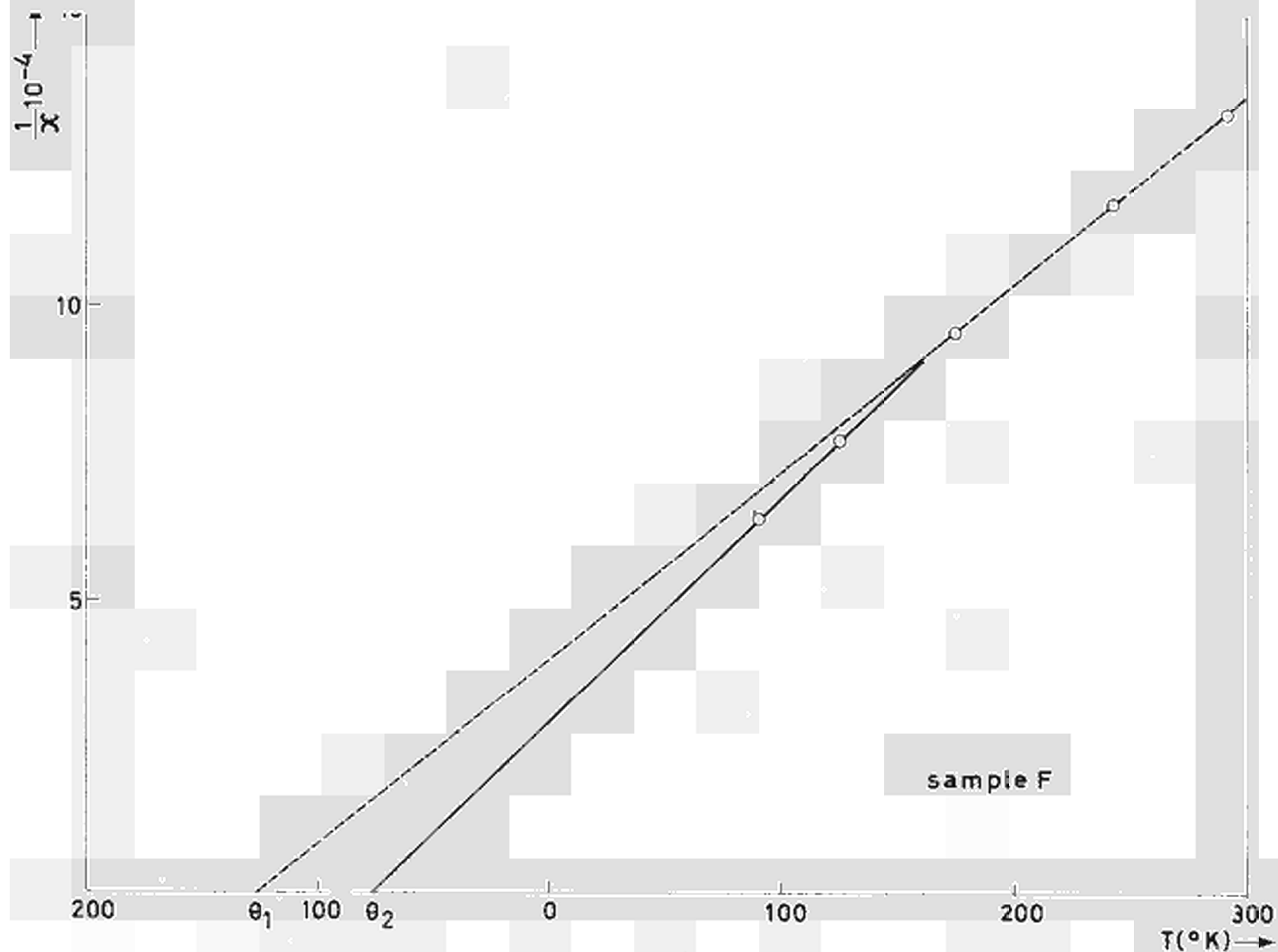
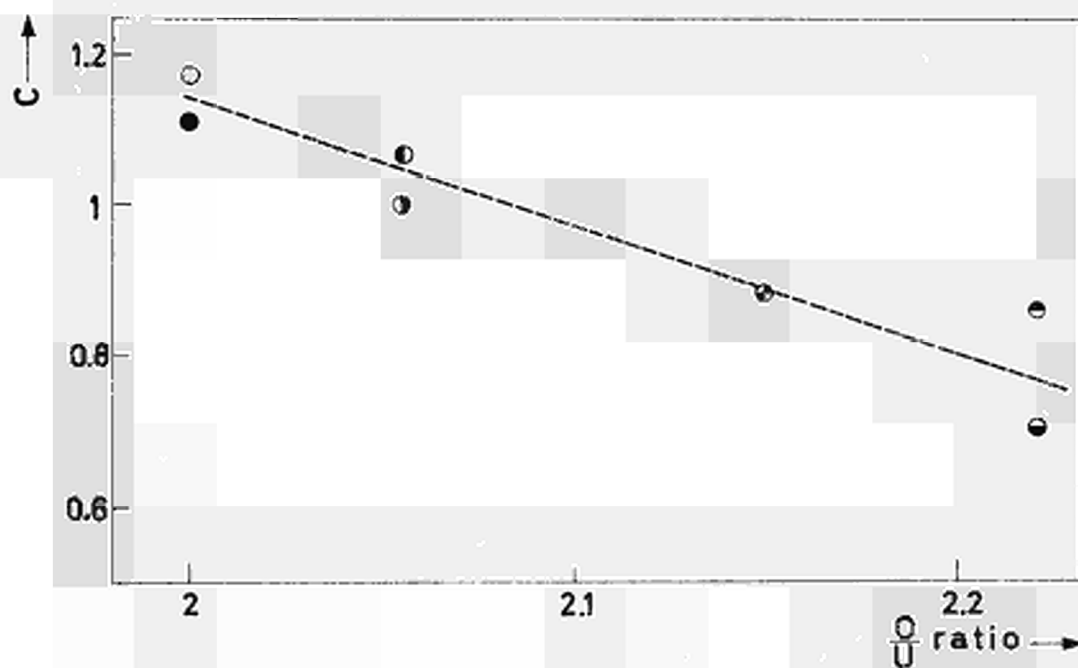
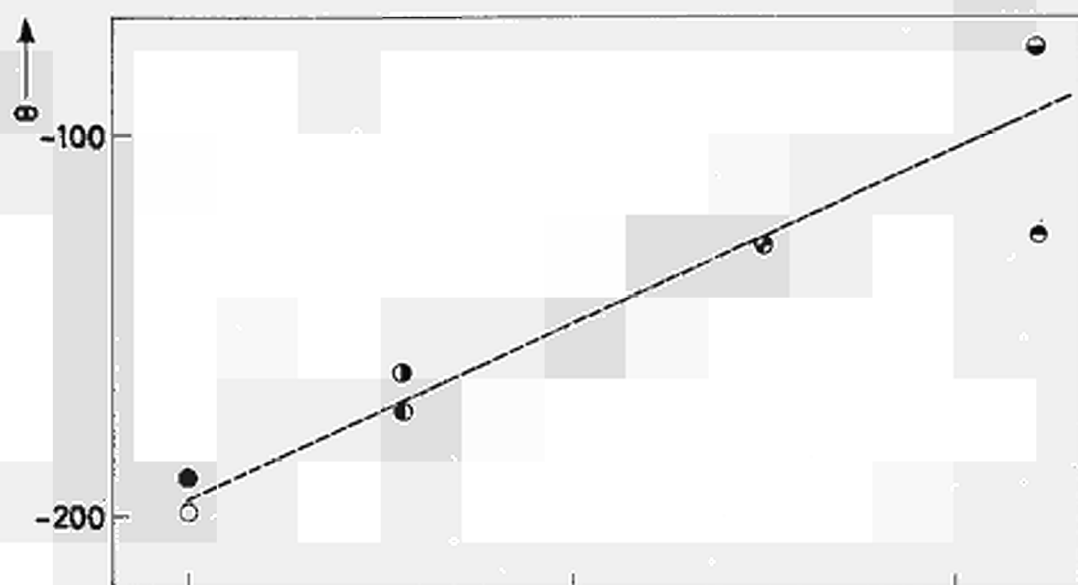


Fig. 56

Reciprocal of the magnetic susceptibility of a UO_2 crystal (χ) as a function of the absolute temperature

Fig. 57

Weiss constant θ of different UO_2 crystals as a function of the O/U ratio

○ A	● C	● E	● 160° < T
● B	● D	● F	● 90° < T < 160° K

Fig. 58

Curie constant C of different UO_2 crystals as a function of the O/U ratio



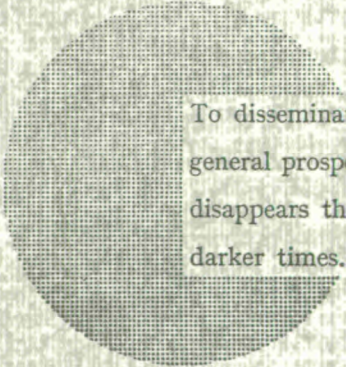
NOTICE TO THE READER

All Euratom reports are announced, as and when they are issued, in the monthly periodical **EURATOM INFORMATION**, edited by the Centre for Information and Documentation (CID). For subscription (1 year : US\$ 15, £ 5.7) or free specimen copies please write to :

**Handelsblatt GmbH
"Euratom Information"
Postfach 1102
D-4 Düsseldorf (Germany)**

or

**Office de vente des publications
des Communautés européennes
2, Place de Metz
Luxembourg**



To disseminate knowledge is to disseminate prosperity — I mean general prosperity and not individual riches — and with prosperity disappears the greater part of the evil which is our heritage from darker times.

Alfred Nobel

SALES OFFICES

All Euratom reports are on sale at the offices listed below, at the prices given on the back of the front cover (when ordering, specify clearly the EUR number and the title of the report, which are shown on the front cover).

OFFICE CENTRAL DE VENTE DES PUBLICATIONS DES COMMUNAUTES EUROPEENNES

2, place de Metz, Luxembourg (Compte chèque postal N° 191-90)

BELGIQUE — BELGIË

MONITEUR BELGE
40-42, rue de Louvain - Bruxelles
BELGISCH STAATSBAD
Leuvenseweg 40-42 - Brussel

LUXEMBOURG

OFFICE CENTRAL DE VENTE
DES PUBLICATIONS DES
COMMUNAUTES EUROPEENNES
9, rue Goethe - Luxembourg

DEUTSCHLAND

BUNDESANZEIGER
Postfach - Köln 1

NEDERLAND

STAATSDRUKKERIJ
Christoffel Plantijnstraat - Den Haag

FRANCE

SERVICE DE VENTE EN FRANCE
DES PUBLICATIONS DES
COMMUNAUTES EUROPEENNES
26, rue Desaix - Paris 15^e

ITALIA

LIBRERIA DELLO STATO
Piazza G. Verdi, 10 - Roma

UNITED KINGDOM

H. M. STATIONERY OFFICE
P. O. Box 569 - London S.E.1

EURATOM — C.I.D.
51-53, rue Belliard
Bruxelles (Belgique)

CDNA03323ENC